FREQUENCY-DEPENDENT SEISMIC REFLECTIVITY OF RANDOMLY FRACTURED FLUID-SATURATED MEDIA

A Dissertation Presented to

the Faculty of the Department of Earth and Atmospheric Sciences

University of Houston

In Partial Fulfillment

of the Requirements for the Degree

Doctor of Philosophy

By

Anna Krylova

May 2017

FREQUENCY-DEPENDENT SEISMIC REFLECTIVITY OF RANDOMLY FRACTURED FLUID-SATURATED MEDIA

____

Anna Krylova

APPROVED:

____

Dr. Evgeny M. Chesnokov, Chairman

____

Dr. Gennady M. Goloshubin

____

Dr. Robert R. Stewart

____

Dr. Haitao Ren

____

Dean, College of Natural Science and Mathematics

ACKNOWLEDGMENTS

This research would not be possible with anyone other than my advisor and mentor Dr. Gennady Goloshubin. I am grateful to him for the shared geophysical knowledge beyond the subject of this work, his reasonable criticism, support and dedication.

A special gratitude I give to the chairman of the committee and advisor, Dr. Evgeny Chesnokov, also to Dr. Robert R. Stewart for comments, time and efforts, and Dr. Haitao Ren for practical industrial insights and remark. I want to give a special thanks to Nikolay Dyaur for the help with measurements. I would like to thank all other professors of the University of Houston for guiding through the geoscience theoretical foundations.

I would like to thank The West-Siberian Research Institute of Geology and Geophysics through Contract with the University of Houston, as well as by the University of Stavanger through the Low Frequency Consortium Project for the support of this research.

I am deeply thankful to my family: my mother Marina Krylova, grandmother Valentina Korchagina, who despite the distance always love, believe in and support me; my newly gained family in U.S: my beloved fiance Alex Khadeev, Yulia and Anna Khadeeva for understanding, encouragement and help during my graduate school.

I dedicate this work in memory of two outstanding personalities: Valeri Korneev, who stands behind an idea of this research and contributed a lot to the development of the Krauklis wave, and to granddad, Valeriy Korchagin, who raised me to be a dedicated person, unconditionally loved and supported me.

FREQUENCY-DEPENDENT SEISMIC REFLECTIVITY OF RANDOMLY FRACTURED FLUID-SATURATED MEDIA

An Abstract of a Dissertation

Presented to

the Faculty of the Department of Earth and Atmospheric Sciences

University of Houston

In Partial Fulfillment

of the Requirements for the Degree

Doctor of Philosophy

By

Anna Krylova

May 2017

ABSTRACT

Fractures exist on a wide range of scales from microns to hundreds of meters. Throughout this scale range, fractures have a significant influence on fluid flow and physical properties of rocks. The average elastic properties of a randomly fractured fluid-filled rock were discussed for different fracture distribution laws in association with the extremely slow and dispersive guided wave propagation within individual fractures. Krauklis wave was used as an asymptotic solution of the fluid interface wave (FIW) equations.

Different fracture distribution laws (exponential, power, fractal and gamma laws) within the rock in the seismic range of frequencies ($10 - 100Hz$) initiated high-velocity dispersion and attenuation of the P-wave. Calculations showed that increase of one order of fracture density enhances velocity dispersion and attenuation by 20%, in particular, at low seismic frequencies.

Different cases of acoustic impedance distributions versus depth for assessing reflection properties from fractured and non-fractured layers have been considered. Results demonstrated the remarkable difference between the P-wave reflection coefficient from the fractured layer and the P-wave reflection coefficient from the non-fractured layer: about 30-40% decrease in amplitude for the fractured high-impedance layer, about 30-50% increase of amplitude for the fractured low-impedance layer and about 20% decrease for the intermediate case. The biggest difference in the behavior of reflection coefficient versus incident angle is observed at seismic low-frequencies ($<$ 15Hz). The thickness related tuning effect has the different impact on the seismic signal in the fractured and homogeneous layers for all acoustic impedance cases.

The approach and results of calculations allow an interpretation of abnormal velocity dispersion, high attenuation, and special behavior of reflection coefficients vs. frequency and angle of incidence as the indicators of fractures. The analysis of the seismic monitoring

data from the Royal Center Field, Indiana, indicates the frequency-dependent difference of attenuation and velocity of the P-wave in water saturated and gas saturated formation. It is in agreement with numerical modeling results involving Krauklis wave theory. The difference is bigger at low frequencies. The numerical modeling explains a low-frequency seismic anomaly, detected in fractured zones within source rock in the East-Surgut Basin, Western Siberia. The study of the laboratory measurements on the fractured 3-D printed samples indicates the possibility of a P-wave velocity prediction in the fluid-filled fractured sample based on the velocity of non-fractured porous saturated background.

Contents

List of Figures

Frequently used symbols

Symbol	Meaning	Units
V_P	P-wave Velocity	m/s
V_S	S-wave Velocity	m/s
ρ_{fl}	Fluid Density	kg/m^3
η_{fl}	Viscosity of a Fluid	Pa s
ρ_m	Density of a Background Matrix	kg/m^3
G	Shear Modulus	Pa
f	Frequency	Hz
ω	Angular Frequency	rad/s
ϕ	Porosity	-
h	Fracture Thickness	m
$N_e(l)$	Exponential Law	-
$N_y(l)$	Gamma Law	-
$N_p(l)$	Power Law	-
$N_f(l)$	Fractal Law	-
C_y	Empirical Constant	-
C_p	Empirical Constant	-
C_f	Empirical Constant	-
N_0	Fracture density	-
l_0	Length	m
$u_z^{(m)}$	Displacement in matrix	m
$u_z^{(f)}$	Displacement in a fracture	m
$\tau_{zz}^{(m)}$	Normal Component of stress in matrix	Pa
$\tau_{zz}^{(f)}$	Normal Component of stress in a fracture	Pa
$\tau_{xy}^{(f)}$	Horizontal Component of stress in a fracture	Pa
$\rho^{(B)}$	Density	kg/m^3
α^*	Biot-Willis Effective Stress Coefficient	-
M	Storage Modulus	Pa

Symbol	Meaning	Units
$\mathbf{R}(\xi^2)$	Rayleigh Equation	-
ξ_P	P-wave Slowness	s/m
ξ_S	S-wave Slowness	s/m
ξ_{P_3}	3-direction P-wave Slowness	s/m
ξ_{S_3}	3-direction S-wave Slowness	s/m
η_M	Storage Fracture Compliance	m/Pa
η_D	Drained Normal Fracture Compliance	m/Pa
η_T	Shear Fracture Compliance	m/Pa
η_N^*	Effective Normal Fracture Compliance	m/Pa
$V_K(\omega)$	Krauklis wave velocity	m/s
$\widehat{V}_K(\omega)$	Viscous Krauklis wave velocity	m/s
$E(\omega)$	Resonance Energy	-
Vol	P-wave Volume	m^3
v_f	Volume of a Single Fracture	m^3
Vol_f	Total Volume of Fluid	m^3
$v_{fr}(\omega)$	Wave Volume of a Single Fracture	m^3
Vol_{fr}	Cumulative Fracture Volume	m^3
Vol_m	Matrix Volume	m^3
f_{max}	Maximum Observed Seismic Frequency	Hz
f_{min}	Minimum Observed Seismic Frequency	Hz
L_{max}	Maximum Fracture Length	m
L_{min}	Minimum Fracture Length	m
$\overline{\rho}$	Average Density of the Media	kg/m^3
ρ_{fr}	Density of Fluid and Adjacent Matrix	kg/m^3
$\Im$	Imaginary Part	-
$\Re$	Real Part	-
$\overline{V}_P$	Effective P-wave velocity	m/s
$\overline{V}_S$	Effective S-wave velocity	m/s

Symbol	Meaning	Units
Q_m	Quality Factor of the Matrix	-
$\overline{Q}$	Quality Factor of the Fractured Medium	-
R_P	Reflected P	-
R_S	Reflected S	-
T_P	Transmitted P	-
T_S	Transmitted S	-
θ_1	Angle of Incidence	degree
θ_2	Angle of Transmitted P-wave	degree
ϕ_1	Angle of the Reflected S-wave	degree
ϕ_2	Angle of the Transmitted S-wave	degree
$R(\omega,\alpha)$	Amplitude of reflection coefficient from a layer	-
$\Theta(\omega,\alpha)$	Phase of reflection coefficient from a layer	-
α	Angle of Incidence	degree
$\overline{\rho}_m$	Density of the Fractured Matrix	m/s
$\tilde{V}_{P_1}$	Velocity of the Half-space Above	m/s
$\tilde{V}_{P_3}$	Velocity of the Half-space Below	m/s
ρ_g	Liquified Gas Density	kg/m^3
η_g	Liquified Gas Viscosity	Pa s

1 Introduction

1.1 Motivation and objectives

Fractures are common features of a rock, they serve as natural storage and transport paths for fluids, including hydrocarbons (Figure 1). The fracture modeling itself is a challenging problem: there are numerous studies ranging from the explicit description of particular fracture shapes to globally scaled fracture systems. Among of the most used is a model of a fracture as an ellipsoid or “penny-shape” (Hudson, 1981, 2000; Bakulin et al., 2000a, and others); other widely-used models include fractures as alternating soft and hard layers (Molotkov, 1979, 1984; Schoenberg, 1983, and others), and fractures with rough walls and inclusions (Greenwood and Williamson, 1966; Walsh and Grosenbaugh, 1979; Nagy et al., 1993; Pecorari, 1997; Kozlov, 2004 and others). All of above represent effective models substituting real discrete media by equivalent continuous media.

Figure 1. The fracture distribution in nature (*Snapshot from (Hargitaia et al., 2014)*).

Anisotropy of a medium is created by organized oriented fractures and is a popular topic in geophysical literature (Chesnokov et al., 1984; Schoenberg and Douma, 1988; Liu et al., 1993; Chesnokov et al., 1995; Bayuk and Chesnokov, 1998; Bakulin et al., 2000b; Shapiro, 2017, and others). There are number of works that involve frequency-dependent anisotropy including Schoenberg and Sayers (1995), Liu et al. (2002), Chapman (2003) and more recent Tsvankin et al. (2010), Liner (2012, 2016).

Random fracture distribution also commonly occurs in nature. There is no anisotropy associated with a randomly oriented fractured medium, and it is considered isotropic.

Fractures exist on a wide range of scales from microns to hundreds of meters. Throughout this range, they have a significant influence on the fluid flow and physical properties of rocks (Bonnet et al., 2001). Seismic waves spreading in the solid subsurface and encountering fluid-saturated fractures of various sizes may initiate the wave phenomena (Frehner, 2013).

In this work, the mechanism of the averaging elastic module for P-wave velocity computations of the fractured fluid-saturated rock is suggested with respect to the following assumptions:

- There is a random fracture distribution in the medium, hence fractured medium is presumed isotropic.
- Single fluid-saturated fracture is considered as a thin liquid layer with unsealed tips.
- Unsealed tips are connected with the permeable matrix.
- A fluid guided wave is propagating within the fracture.
- Interactions between fractures are not considered.

The mechanism of averaging was analyzed and discussed with respect to the effect of strong and dispersive fluid guided interface wave (FIW) (Korneev and Goloshubin, 2015). At the low frequencies, the asymptotic solution of FIW is known as the Krauklis wave, which was named after its first discoverer (Krauklis, 1962).

Compared to other related waves, the K-wave carries most of the wave energy and is an intense wave phenomenon in a fluid-saturated fracture. Krauklis wave (K-wave) is a product of an interaction between the fluid and the elastic walls of a fracture during their oscillation. K-wave has been investigated in detail analytically, numerically and experimentally (Krauklis, 1962; Ferrazzini and Aki, 1987; Krauklis et al., 1994; Goloshubin et al., 1994; Krauklis et al., 1997; Groenenboom and Falk, 2000; Ionov, 2007; Korneev, 2008; Frehner and Schmalholz, 2010; Maksimov et al., 2011; Frehner, 2013; Korneev et al., 2012; Nakagawa and Korneev, 2014; Nakagawa et al., 2016).

Assuming the existence of the frequency-dependent K-wave within the fractures, computations demonstrate remarkable dispersion and attenuation of P-wave velocity in fractured media and abnormal reflection coefficients from the fractured layer (Krylova and Goloshubin, 2016a,b, 2017).

Posterior calculations of the reflection coefficient from the isotropic-fractured layer with the consideration of the slow and dispersive K-wave propagation within individual fractures were expanded into three cases of the acoustic impedance distribution. The presence of the tuning effect and its dispersive character for the fractured layers of different width were taken into an account. Three case studies are aimed to explain and verify the averaging and reflectivity analysis technique on seismic time-lapse monitoring of the gas storage in the Royal Center Field, Indiana, seismic field data from East-Surgut Basin, Western Siberia, and measured data from Allied Geophysics Laboratory (AGL).

2 Fractures in nature

2.1 Fracture distributions

The nature of fractures is mainly the result of tectonic processes in the Earth, heterogeneity of rocks, and overburden pressure. Fractures in a rock are present in a variety of distributions. The most common distributions are by orientation (Fisher, 1953; Kuster and Toksoz, 1974; Long et al., 1982; Park et al., 2001), by location (Baecher and Lanney, 1978; Long et al., 1982; Priest, 2012), and by length (Baecher et al., 1977; Long et al., 1982; Dershowitz and Einstein, 1988; Bour and Davy, 1997; Bonnet et al., 2001; Park et al., 2001; De Dreuzy et al., 2001).

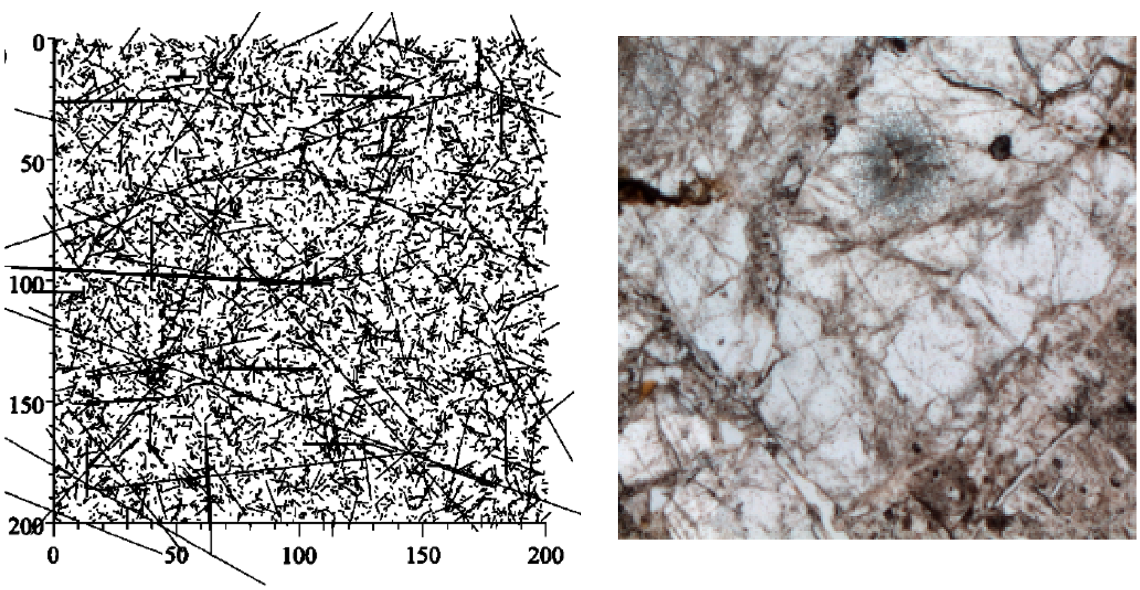

(a) The fracture distribution network (*Snapshot from (Bour and Davy, 1997)*).

(b) The fracture distribution in nature (*Snapshot from (Rempe et al., 2013)*).

Figure 2. Illustration of two fractured systems: modeled and natural.

Organized oriented fractures of any size may create anisotropy of the matter (Chesnokov et al., 1984; Schoenberg and Douma, 1988; Chesnokov et al., 1995; Bayuk and Chesnokov, 1998; Shapiro, 2017, and others). The random distribution of fractures is also very common and natural; however, in this case, there is no anisotropy connected with a fluid-saturated fractured medium. In a fracture modeling (Figure 2a), the length-dependent number of chaotically oriented fractures can be described by exponential law, gamma law, power law, and fractal law, a special case of the power law, that are based on real practical data (De Dreuzy et al., 2001; Bonnet et al., 2001). These laws allow considering the same distribution and behavior of the fractured system on the extended scale, both smaller volumes and larger, than the original. This work, after comparison of the above-mentioned laws, focuses on fractures with individual properties that are governed by the fractal distribution in the isotropic-fractured media.

The number of fractures N in each law declines with increase of length l. The laws are described by equations below:

- exponential law:

$$N_e(l) = N_0 \exp\left[-\frac{l}{l_0}\right], \tag{1}$$

- gamma law:

$$N_\gamma(l) = N_0 \left[\frac{l}{l_0}\right]^{-C_\gamma} \exp\left[-\frac{l}{l_0}\right], \tag{2}$$

- power law:

$$N_p(l) = N_0 \left[\frac{l}{l_0}\right]^{-C_p}. \tag{3}$$

Special case of power law (3), when $C_p = C_f$ and $1 \leq C_f \leq 3$, is called fractal law (Bour and Davy, 1997):

$$N_f(l) = N_0 \left[\frac{l}{l_0}\right]^{-C_f}. \tag{4}$$

Here N_0 is a calibration constant, that defines the density of the fracture distribution (Davy et al., 1990), l_0 is the characteristic length, C_γ, C_p, and C_f are empirical constants. The Figure 3 illustrates fracture distribution for laws with $C_\gamma = C_p = 2$, and $C_f = 2.5$. The specific goals, parameters, and conditions of investigated formations have influence on the choice of appropriate constants and law of the fracture distribution in each study.

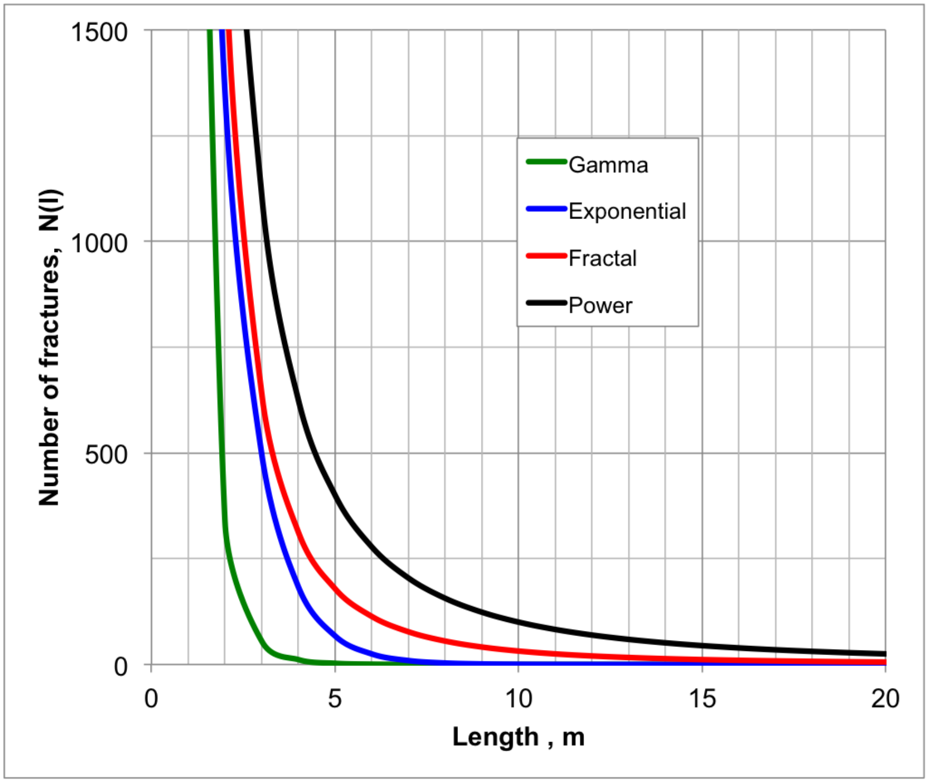

Figure 3. Number of fractures depending on the fracture length in a given volume for different laws $N_p(l)$ black, $N_f(l)$ red, $N_e(l)$ blue, $N_\gamma(l)$ green. $C_\gamma = 2$, $C_p = 2$, $C_f = 2.5$

3 Waves in fracture

3.1 Fluid interface waves

As it is suggested by Pyrak-Nolte and Cook (1987) and Gu et al. (1996), each single open fluid-saturated thin fracture at any scale provides interaction of Rayleigh surface waves coupled across a fracture. These fracture interface waves (FIW) satisfy the boundary conditions: $u_z^{(m)} = u_z^{(f)}$ the continuity of the displacement perpendicular to the fracture, $\tau_{zz}^{(m)} = \tau_{zz}^{(f)}$ the continuity of normal stress, and $\tau_{xy}^{(f)} = 0$ free-surface conditions for the horizontal stress component (Korneev et al., 2014). FIW's can be either symmetric or anti-symmetric particle motions across the fracture in elastic model, referred to as classical linear-slip-interface model (LSIM) (Schoenberg, 1980). The LSIM was extended to poroelastic media, taking into account fluid pressure and displacement within the fracture volume (Nakagawa and Schoenberg, 2007; Korneev, 2010; Frehner, 2013). Nakagawa and Korneev (2014) derived the extended LSIM for the permeable fractures, connecting wave-induced stress and displacement on the two parallel surfaces bounding a compliant layer representing a fracture, under the constrain that the thickness of the layer is reduced to zero. The derivation resulted in the frequency equations of the waves guided by a fluid-saturated fracture:

$$\mathbf{R}(\xi^2) + i\left(\frac{2\xi_S}{\omega\rho^{(B)}\eta_T}\right)\xi_{S3}\xi_S^2 = 0, \tag{5}$$

$$\mathbf{R}(\xi^2) + i\left(\frac{2\xi_S}{\omega\rho^{(B)}\eta_N^*}\right)\xi_{P3}\xi_S^2 = 0, \tag{6}$$

where $\mathbf{R}(\xi^2) \equiv \left(2\xi^2 - \xi_S^2\right)^2 + 4\xi^2\xi_{P3}\xi_{S3}$ is Rayleigh equation, $\rho^{(B)}$, ξ_P, and ξ_S are the density and P- and S-wave slowness of the background media, respectively; $\xi_{P3} = \sqrt{\xi_P^2 - \xi^2}$

and $\xi_{S3} = \sqrt{\xi_S^2 - \xi^2}$ are the third (z-) direction P- and S- wave slowness, ω is the angular frequency; η_T and η_N^* are the shear fracture compliance and effective normal fracture compliance, respectively.

The dispersion equation (5) describes anti-symmetric FIW's. Anti-symmetric FIW's equation is not controlled by the fluid properties of the saturation material in the fracture for low frequencies (Nakagawa and Korneev, 2014). It has weak dependence on the frequency, and the solution is asymptotically close to Rayleigh and Scholte-wave velocities.

The symmetric FIW case is governed by the equation (6). It depends on the fracture compliance, wave frequency and slowness, likewise fluid viscosity and fracture permeability (Nakagawa and Korneev, 2014). Assuming $|\xi_P^2|$ and $|\xi_S^2| \ll |\xi^2|$, equation (6) can be re-written as:

$$\omega \frac{\rho^{(B)}}{\xi_S^2}\left(1 - \frac{\xi_P^2}{\xi_S^2}\right)\xi + \frac{1}{\eta_N^*} = 0 \tag{7}$$

and can be represented as third order polynomial in ξ:

$$\chi\beta\xi^3 + \frac{\beta}{\eta_D}\xi^2 + \chi\eta_M\xi + \frac{\eta_M}{\eta_D} + \alpha^* = 0 \tag{8}$$

where α^* is the Biot-Willis coefficient, η_M is storage compliance, η_D is drain module compliance, and

$$\chi \equiv \omega \frac{\rho^{(B)}}{\xi_S^2}\left(1 - \frac{\xi_P^2}{\xi_S^2}\right),$$
$$\beta \equiv \frac{i\omega h^3}{12\eta_{fl}}.$$

For the open fracture, $\eta_D \to \infty$, $\alpha \to 1$, and storage coefficient $M \to \frac{\xi_A^2}{\rho_{fl}}$, where ξ_A is the acoustic wave slowness, and ρ_{fl} is the fluid density. For stiff fluids $|\xi_A| \ll |\xi^2|$ and equation

(7) and can be reduced to:

$$\chi\beta\xi^3 + 1 = 0 \tag{9}$$

resulting in the expression for the phase velocity:

$$\frac{1}{\xi} = h\left[-i\frac{\omega^2 G^{(B)}}{12\eta_{fl}}\left(1-\frac{\xi_P^2}{\xi_S^2}\right)\right]^{\frac{1}{3}} \tag{10}$$

that is identical to the asymptote expression for the thin fracture by Korneev (2008). For a rigid background with $\xi_S \to 0$ and $\chi \to \infty$, equation (7) becomes

$$\beta\xi^2 + \eta_M = 0 \tag{11}$$

yielding an asymptote

$$\frac{1}{\xi} = \sqrt{\frac{\omega k(\omega) M}{i\eta_{fl}}} \tag{12}$$

where $k(\omega)$ is a frequency-dependent permeability. This equation is the low-frequency phase of the Biot's slow P-wave (Pride et al., 2002) for a porous media with the rigid frame. In summary, the solution of symmetric equation (6) has Biot' slow wave (infinitely high shear modulus, diffusive character) and Krauklis wave (open fracture with parallel interfaces, dispersive) velocities as asymptotes (Korneev and Goloshubin, 2015).

This work is focused on the Krauklis wave (K-wave) velocity as the solution of the dispersion equation within the fracture. The K-wave carries most of the wave energy relative to other waves of the similar nature, and is an intense wave phenomenon in a fluid-saturated fracture (Frehner, 2013; Shih and Frehner, 2016).

3.2 Krauklis wave

Acoustic waves propagation through the fracture medium causes the movement of the elastic walls in each fracture. Contractions of fracture's walls result in a strong and dispersive fluid-guided wave, running in it. Through the history, such fluid wave was called differently: slow wave (Krauklis, 1962; Ferrazzini and Aki, 1987), crack wave (Chouet, 1986), Stoneley wave (Tang and Cheng, 1988), Stoneley guided wave (Korneev, 2008; Frehner and Schmalholz, 2010). Due to ingrown interest to this type of wave, it was agreed to give the wave a name "Krauklis wave", after Pavel Krauklis who gave the first theoretical description of it (Korneev et al., 2012). Both body waves P- and S- can initiate Krauklis wave propagation at any tip of a fracture (Frehner, 2013), moreover, the K-wave can be originated in the fracture intersection, similar to tube waves (Ionov, 2007; Maksimov et al., 2011).

Classical modeling of the Krauklis wave (K-wave) consists of two straight parallel elastic walls and a viscous fluid layer in between, which is the idealized model of the complex fracture structures in the real rocks. In latest publications Nakagawa and Korneev (2014) and Nakagawa et al. (2016) considered more realistic fracture model, assumed roughness and irregularity of the walls with a granular filling of the fracture space (proppant-like filling) and has permeability and fracture connectivity as parameters. Asymptotic solutions of this more generalized model lead to earlier classical approach.

Consider the fracture with parallel walls and a fluid layer inside: the classical model. The plain wave originates Krauklis wave propagation in a volume occupied by the fracture. The velocity of propagation of the K-wave in each single fracture is described by original formula from Krauklis (1962):

$$V_K(\omega) = \left(\frac{\omega h G}{\rho_{fl}} \left[1 - \left(\frac{V_S}{V_P} \right)^2 \right] \right)^{\frac{1}{3}}, \tag{13}$$

where ρ_{fl} is a fluid density, G is a shear modulus of the solid, h is an opening of the fracture, $\omega = 2\pi f$ is an angular frequency, and f is frequency in Hz. The elastic medium matrix has P-wave velocity V_P and S-wave velocity V_S. The K-wave velocity profile is illustrated in Figure 4. This is slow and dispersive wave that has specific amplitude distribution inside and outside a fracture (Figure 5). The vertical component achieves maximum strength on the fracture walls (Figure 5a) and the horizontal component prevails inside the fracture (Figure 5b). The wave attenuates slowly within fracture and exponentially in the media outside.

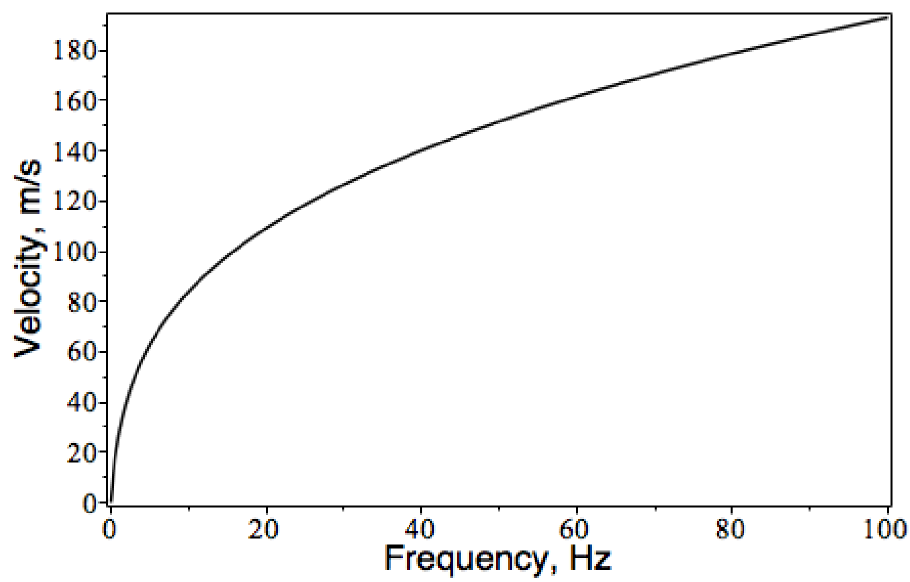

Figure 4. K-wave velocity profile for $h = 10^{-3}$ m, $\rho_{fl} = 800$ kg/m^3, $\eta_{fl} = 1$ cP, $G = 15 \cdot 10^9$ Pa, $V_P = 4000$ m/s, $V_S = 2361$ m/s.

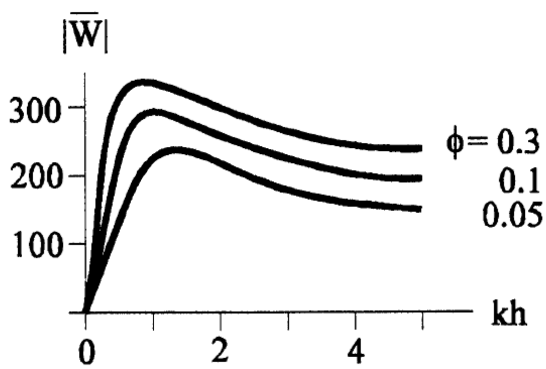

(a) Vertical component.

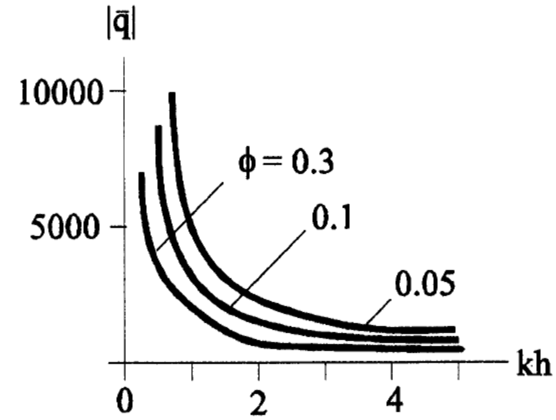

(b) Horizontal component.

Figure 5. (a) The vertical and (b) horizontal components of slow wave amplitude vs. porosity(ϕ), wavenumber (k) and thickness of fracture (h) (Goloshubin et al., 1994)

Later Korneev introduced the slow wave (K-wave) for fractures filled with viscous fluids (Korneev, 2008):

$$\widehat{V}_K(\omega) = V_K(\omega)\left(\frac{\beta}{1+\sqrt{\beta/3}+\beta}\right)^{1/3}, \tag{14}$$

$$\beta = -\frac{i}{12}\frac{h^2\omega\rho_{fl}}{\eta_{fl}}. \tag{15}$$

where $V_K(\omega)$ is a K-wave velocity (13) and η_{fl} is the viscosity of a fluid in the fracture (Figure 6). This modification allows to consider not only velocity of the Krauklis wave for the single fracture, but also the attenuation for the different ranges of frequency (Figure 7).

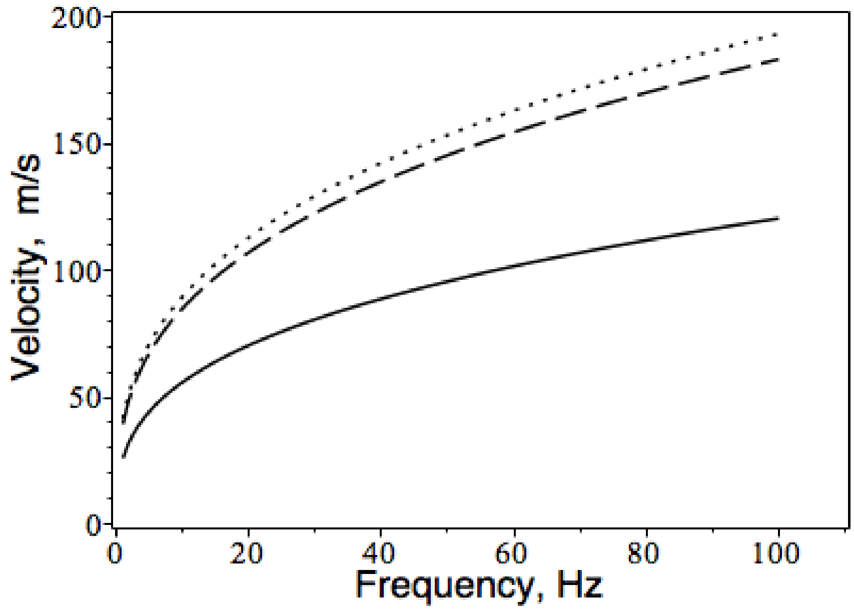

Figure 6. K-wave velocity profile for $\eta_f = 5$ cP (solid), $\eta_f = 1$ cP (dash), $\eta_f = 0.5$ cP (dots) with $h = 10^{-3}$ m, $\rho_{fl} = 800$ kg/m^3, $\eta_{fl} = 1$ cP, $G = 15 \cdot 10^9$ Pa, $V_P = 4000$ m/s, $V_S = 2361$ m/s. The V_K is proportional to $\sqrt[3]{\omega}$.

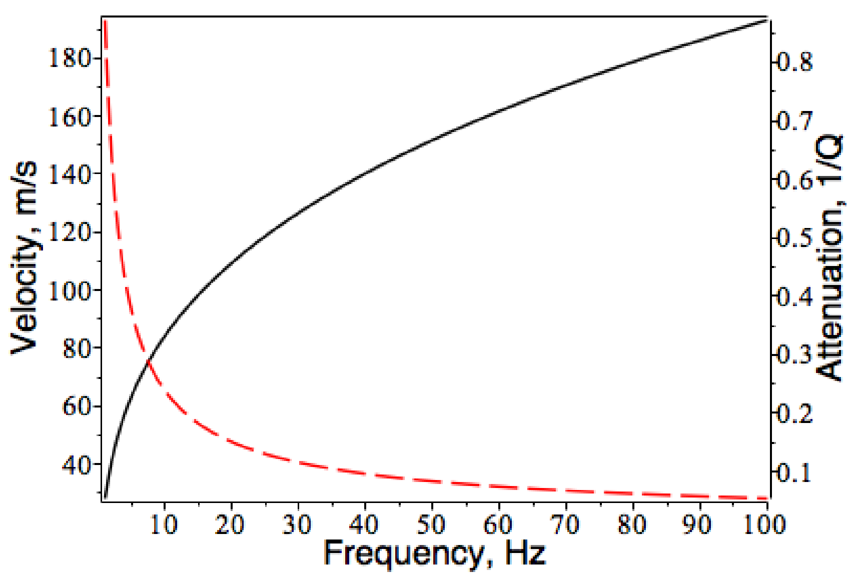

Figure 7. K-wave velocity (black) and attenuation (red-dash) for the water-saturated fracture with $h = 10^{-3}$ m from frequency. K-wave attenuation increases with the frequency.

In accordance with laws (1-4) of fracture distribution (Figure 3), there is some number of fractures with a size comparable to the K-wave wavelength at certain seismic frequencies. This creates resonance conditions for wave propagation within finite fractures.

Korneev (2008) demonstrated that in the case of a fracture with length l, the zero displacement condition $u(0) = 0$ at $x = 0$, and driving displacement $u(l) = u_0 \exp(-i\omega t)$ at $x = l$, the solution for the resonance phenomenon is

$$u(\omega,x) = u_0 A(\omega,x) \exp\left(-i\omega x/\widehat{V}_K\right), \tag{16}$$

$$A(\omega,x) = \frac{\exp\left(i\omega x/\widehat{V}_K(\omega)\right) - \exp\left(-i\omega x/\widehat{V}_K(\omega)\right)}{\exp\left(i\omega l/\widehat{V}_K(\omega)\right) - \exp\left(-i\omega l/\widehat{V}_K(\omega)\right)}. \tag{17}$$

The resonance energy might be presented as the amplitude-square average:

$$E(\omega) = \frac{1}{l}\int_0^l |A(\omega,x)|^2 dx. \tag{18}$$

Krauklis wave, once originated, propagates back and forward along a fracture, whereas each time on the tips or intersections its energy gets partially converted to the body wave and scattered into the surrounding rock (Frehner, 2013). From Figure 8a one can see that the K-wave holds most of its energy in the first mode, which moves depending on the fracture length. The resonance energy (Figure 8a) was calculated for three different lengths $l = 2$ m, $l = 3$ m, $l = 4$ m with $h = 10^{-3}$ m, $\rho_{fl} = 800$ kg/m^3, $\eta_{fl} = 1$ cP, $G = 15 \cdot 10^9$ Pa, $V_P = 4000$ m/s, $V_S = 2361$ m/s. Furthermore, the resonance energy for the fixed length depends on the viscosity of the fluid (Figure 8b) and is larger for less viscous fluids.

In nature, resonance is observed when a fracture length is comparable to the wavelength of a wave. Generally, considering fracture distributions (1)-(4), seismic frequency, the length of the fracture is significantly greater than the K-wave wavelength.

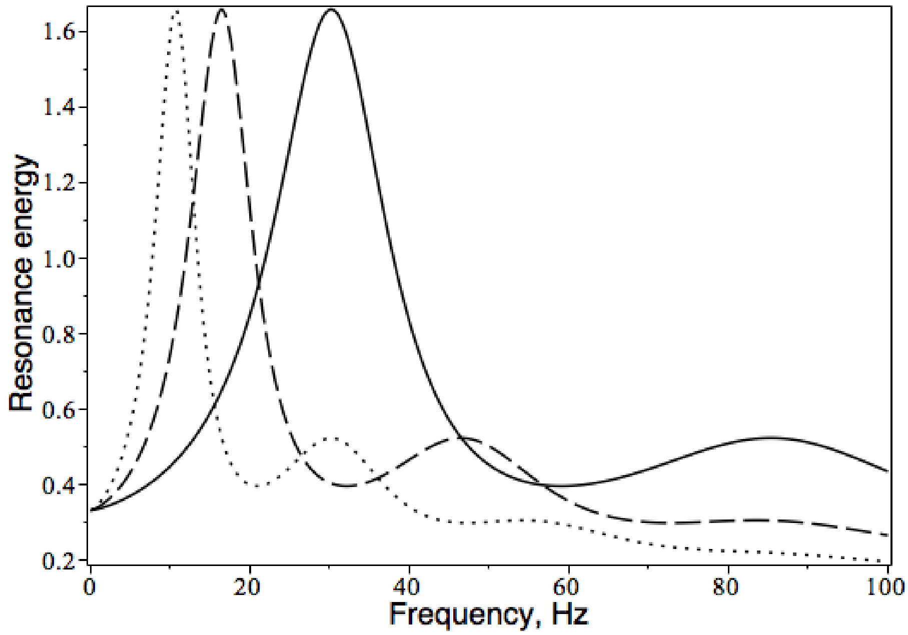

(a) Fractures of various length $l = 2$ m (solid), $l = 3$ m (dash), $l = 4$ m (dots) for $\eta_{fl} = 1$ cP. The K-wave holds most of its energy in the first mode.

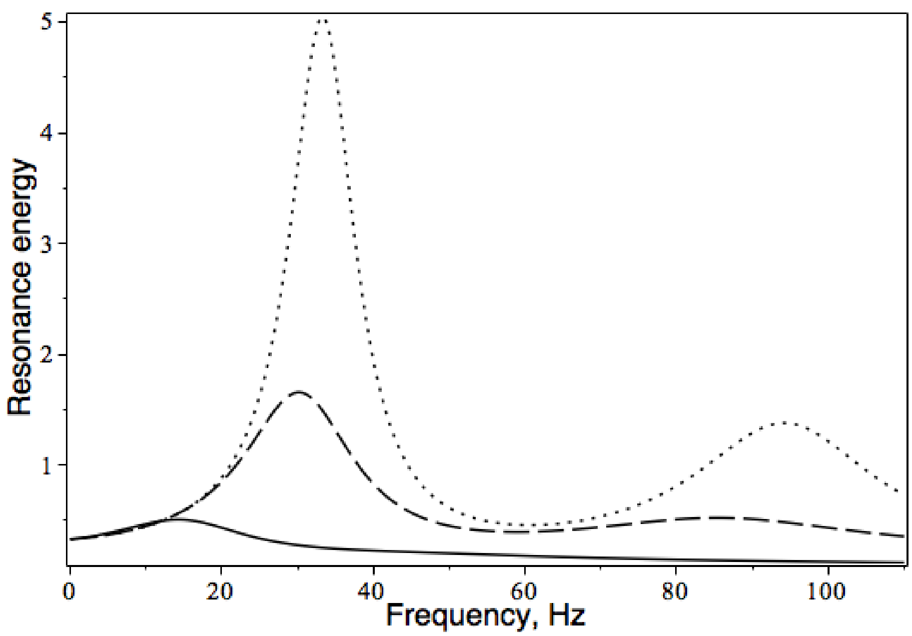

(b) The fracture of length $l = 2$ m for viscosities $\eta_f = 5$ cP (solid), $\eta_f = 1$ cP (dash), $\eta_f = 0.5$ cP (dots). The greater viscosity of fluid, the smaller resonance energy.

Figure 8. The amplitude-square average $E(\omega)$ of the K-wave.

4 Averaging of elastic parameters

Consider a randomly fractured media with the following properties: matrix background with P-wave velocity V_P, S-wave velocity V_S, density ρ_m; saturated fractures with the fluid density ρ_{fl}, viscosity η_{fl}, thickness h, and variable length l. The semi-empirical mechanism of the averaging for computation of P-wave velocity and attenuation of the fractured fluid-saturated rock is described in the framework of the certain wave volumes: volume of the P-wave in the fractured media, volume of a single fracture, cumulative volume of fractures, and volume of the matrix for a limited frequency band $[f_{min}, f_{max}]$.

4.1 Methodology

In the isotropic-fractured fluid-saturated medium, the total averaging volume Vol can be defined as the first Fresnel zone volume:

$$Vol = \frac{4\pi}{3}R^2(x) \cdot \frac{\lambda}{2} = \frac{\pi}{2}\lambda^3, \tag{19}$$

where $R(x)$ is radius of the Fresnel zone, and λ is a P-wave wavelength. For a detailed derivation of this and following wave volumes refer to the Appendix 8.1.

The volume of the fracture with the length l and thickness h is defined by:

$$v_f = \frac{\pi}{3}l^2 h. \tag{20}$$

The guided wave volume can be described with the wavelength λ_K of the K-wave, and the fracture length as:

$$v_{fr}(l,\omega) = \frac{l^2}{6}\lambda_K. \tag{21}$$

The average density in the guided wave volume is

$$\rho_{fr}(\omega) = \frac{\omega h \rho_{fl} + 2V_K(\omega)\rho_m}{\omega h + 2V_K(\omega)}, \tag{22}$$

more detailed derivation is in the Appendix 8.2.

For the given volume (19), the minimum and maximum fracture lengths are defined by V_P,$V_K(\omega)$ and minimum frequency $f_m in$:

$$L_{min} = \frac{V_K(\omega)}{f_{min}}, \tag{23}$$

$$L_{max} = \frac{V_P}{2f_{max}}. \tag{24}$$

The total volume of the fluid in the fracture network can be estimated as:

$$Vol_f = \frac{1}{L_{max} - L_{min}} \int_{L_{min}}^{L_{max}} \nu_f(l) N_i(l) dl, \tag{25}$$

here $N_i(l)$ could be substituted by the desired law $N_e(l)$, $N_\gamma(l)$, $N_p(l)$ or $N_f(l)$ ((1)-(4)). A choice of the law should be based on the seismo-geological parameters of the media.

The cumulative volume Vol_{fr} of fracture system can be estimated by calculation of an integral over the whole domain of the fracture network taking into account the volume of each single fracture (21):

$$Vol_{fr} = \frac{1}{L_{max} - L_{min}} \int_{L_{min}}^{L_{max}} \nu_{fr}(l,\omega) N_i(l) dl \tag{26}$$

In this case, the matrix volume is

$$Vol_m = Vol - Vol_{fr} \tag{27}$$

The effective fracture density $\overline{\rho}$ can be calculated using following expression:

$$\overline{\rho} = \frac{Vol_f \rho_{fl} + Vol_m \rho_m}{Vol} \tag{28}$$

By taking the average of the inverse elastic coefficient with weights according to the fracture volume, we obtain the effective P-velocity:

$$\overline{V}_P^2(\omega) = \frac{1}{\overline{\rho}} \left(\frac{1}{Vol\,(L_{max} - L_{min})} \int\limits_{L_{min}}^{L_{max}} \nu_{fr}(l,\omega) N_i(l) \left(\rho_{fr} \widehat{V}_K^2\right)^{-1} dl + \frac{Vol_m}{Vol} \left(\rho_m \widehat{V}_P^2\right)^{-1} \right)^{-1}, \tag{29}$$

where $\overline{\rho}$ is the density of the fractured fluid-saturated media, ρ_{fr} is the density of the fluid-filled fracture with the neighboring matrix, ρ_m is the density of matrix, $\widehat{V}_K$ is a complex function given by (14) and the $\widehat{V}_P$ consisting of real part $\Re(\widehat{V}_P) = V_P$ and imaginary $\Im(\widehat{V}_P)$ of the matrix, where real and imaginary parts are connected over the P-wave velocity V_P of the matrix the quality factor: $Q_m = \left|\Re(\widehat{V}_P^2)\right| / \left|\Im(\widehat{V}_P^2)\right|$(Carcione et al., 2013).

The effective quality factor $\overline{Q}$ for the fractured fluid-saturated medium is defined as

$$\overline{Q} = \left| \frac{\Re\left(\overline{V}_P^2(\omega)\right)}{\Im\left(\overline{V}_P^2(\omega)\right)} \right|, \tag{30}$$

where $\Re$ and $\Im$ indicate the real and imaginary parts.

The similar averaging can be done for S-wave velocity (Korneev and Goloshubin, 2015). The average $\overline{V}_S$ has weak dependence on the K wave and, as a result, on frequency:

$$\overline{V}_S^2(\omega) = \frac{\Re(\overline{c}_{44}(\omega))}{\rho} \approx V_S^2. \tag{31}$$

4.2 Numerical examples of velocity and attenuation

The theoretical description above was utilized in seismic range of frequencies ($10-100$ Hz) to compare the effective velocity of the layer controlled by different fracture distribution laws (Figure 3). The slow dispersive Krauklis wave is considered to be present in each single fracture. The matrix parameters were $V_P = 2580$ m/s, $V_S = 1290$ m/s, shear modulus $G = 3.65 \cdot 10^9$ Pa, quality factor $Q_m = 80$, density $\rho = 2300$ kg/m^3, fluid density $\rho_{fl} = 1000$ kg/m^3, and fluid viscosity $\eta_{fl} = 1$ cPa. The Gamma law (2) detention is characterized by the exponent $C_\gamma = 2$, the power law (3) has an exponent $C_p = 2$,and the fractal dimension is $C = 2.5$ in the fractal law. For all laws, fracture density is $N_0 = 10^4$, length is $l_0 = 1$ m and the opening of the fractures is $h = 10^{-3}$ m. The calculated effective P-wave velocities (Figure 9) with parameters above demonstrate remarkable dispersion with decrease in frequency. All laws in Figure 9 can be adjusted to satisfy the properties of the medium by taking appropriate N_0 and exponents; hence, for simplicity in further analysis, only the fractal law is considered.

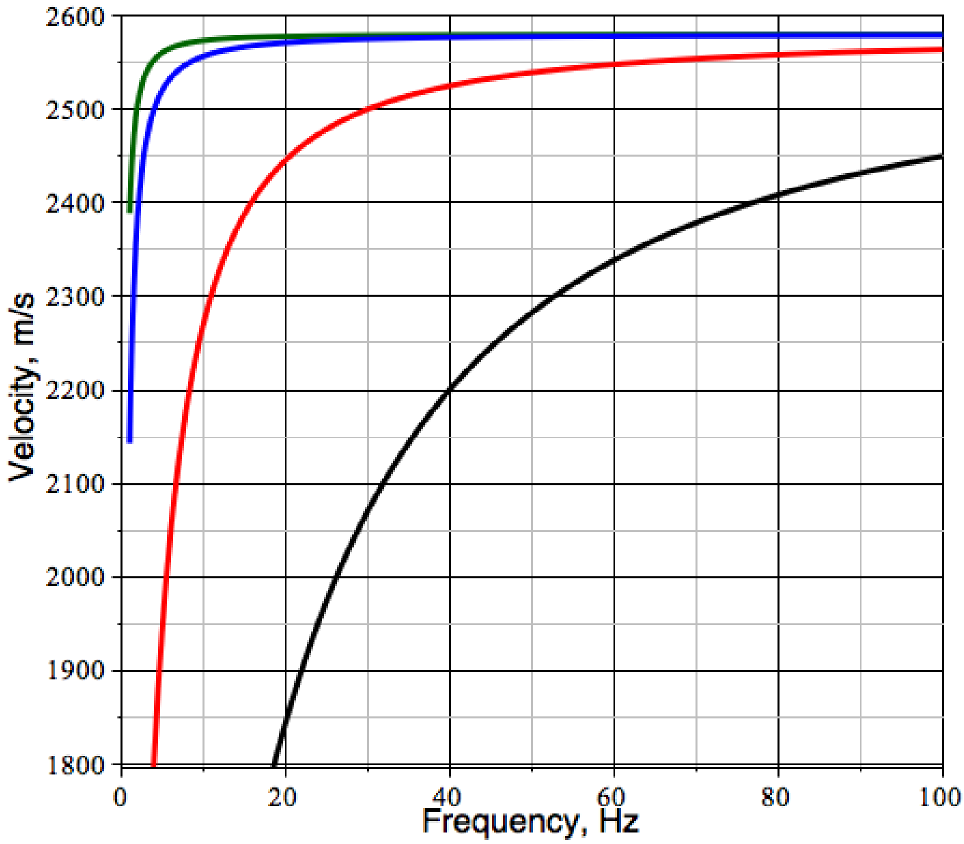

Figure 9. The effective P-wave velocity of the fractured saturated medium is frequency dependent for given laws of the fracture distribution. The color-scheme is same as on Figure 3: $N_p(l)$ black, $N_f(l)$ red, $N_e(l)$ blue, $N_\gamma(l)$ green

For the fracture distribution described by the fractal law (4), the P-wave velocity dispersion and attenuation were modeled for a different range of the calibration density constant N_0. Figure 10 represents velocities in solid lines (29) and attenuation (30) in dot-dashed for three cases of N_0 color-coded for $N_0 = 10^3$ in blue, 10^4 in red, and 10^5 in black. Greater values of N_0 lead to the more dense fracture concentration in the media; therefore, lower velocities in the layer and stronger attenuation were observed.

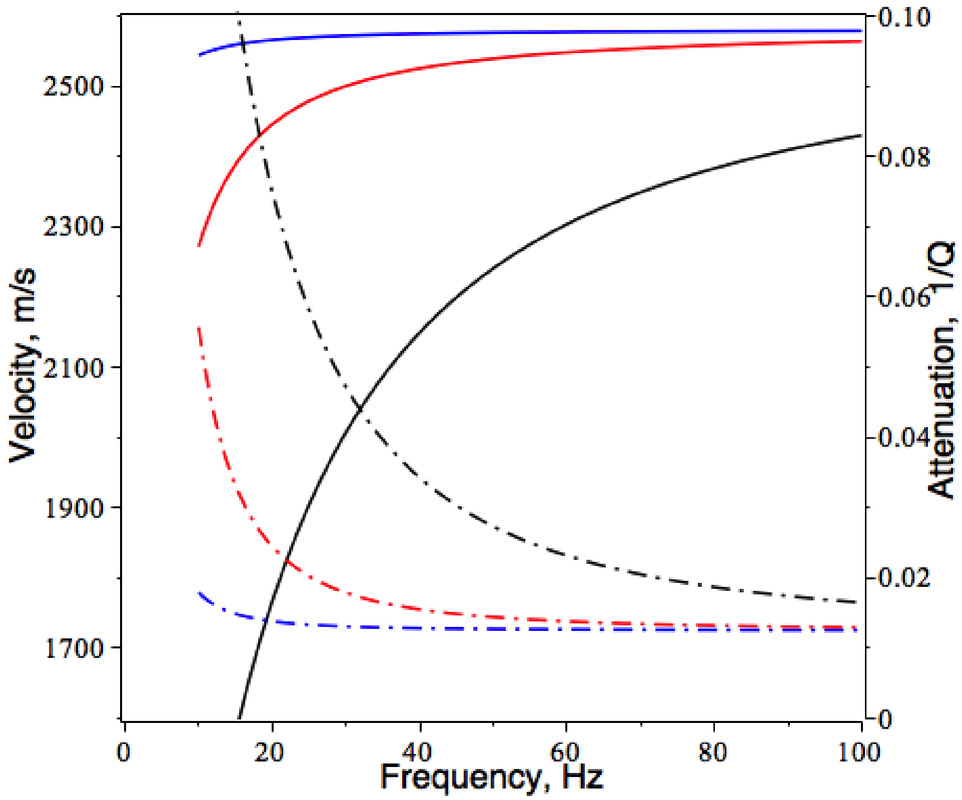

Figure 10. Velocity (solid lines) and attenuation (dot-dashed lines) vs. frequency for the fractal law with different density calibration constant N_0: 10^3 in blue, 10^4 in red, 10^5 in black. The increase of fracture density tends to increase the velocity dispersion and attenuation.

Consider the case with the same fractal distribution with fracture density $N_0 = 10^4$ and liquids with different properties to investigate the effect of viscosity onto effective velocity and attenuation. In Figure 11, the first liquid (solid line) has high viscosity $\eta_f = 5$ cP and $\rho_f = 800$ kg/m^3, second liquid with viscosity $\eta_f = 1$ cP and $\rho_f = 1000$ kg/m^3, and third liquid has lightest viscosity among the three $\eta_f = 0.5$ cP and $\rho_f = 792$ kg/m^3. With the growth of viscosity, greater becomes the attenuation; however, the velocity dispersion is less affected by change in viscosity.

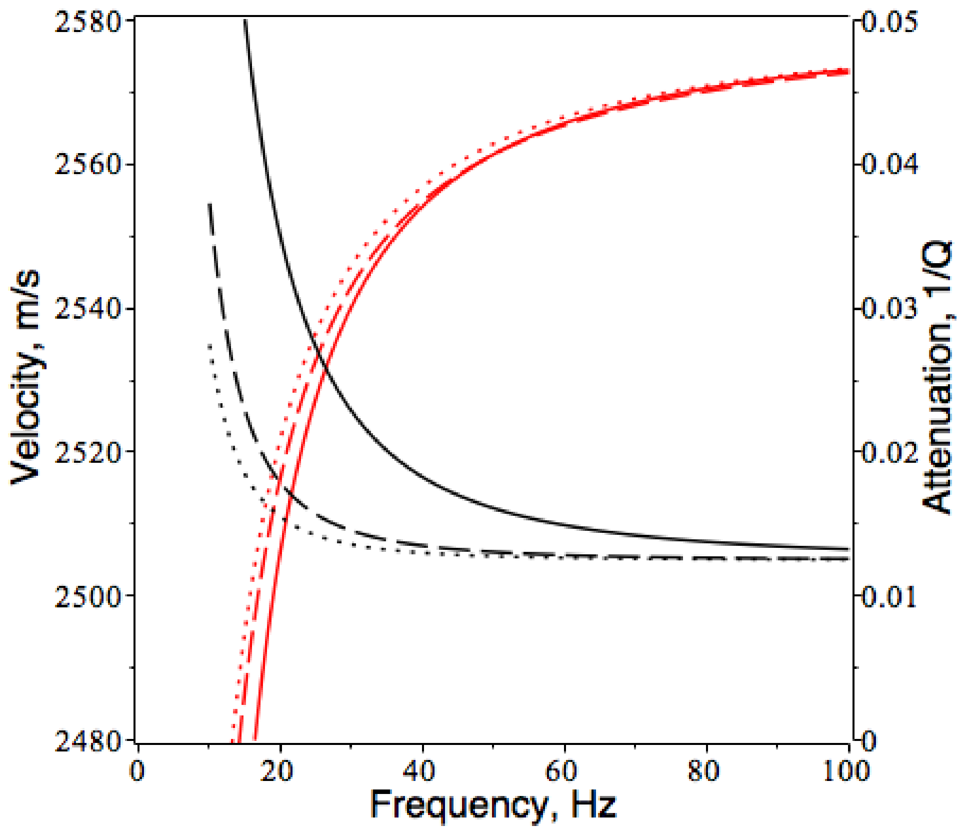

Figure 11. Velocity (red lines) and attenuation (black lines) vs. frequency for the fractal law with fracture density constant $N_0 = 10^4$ depending on viscosity: $\eta_f = 5$ cP (solid), $\eta_f = 1$ cP (dash), $\eta_f = 0.5$ cP (dots).

Additionally, the effect of different Q-factor of the matrix on the attenuation of the media was considered for the fractal law (4) of fracture distribution for $N_0 = 10^4$. In Figure 12, the velocity curve was left for the reference, and quality factors were varying: $Q_m = 20$ in orange, $Q_m = 40$ in magenta, and $Q_m = 80$ in purple. The attenuation rate increased with the increase in Q-factor.

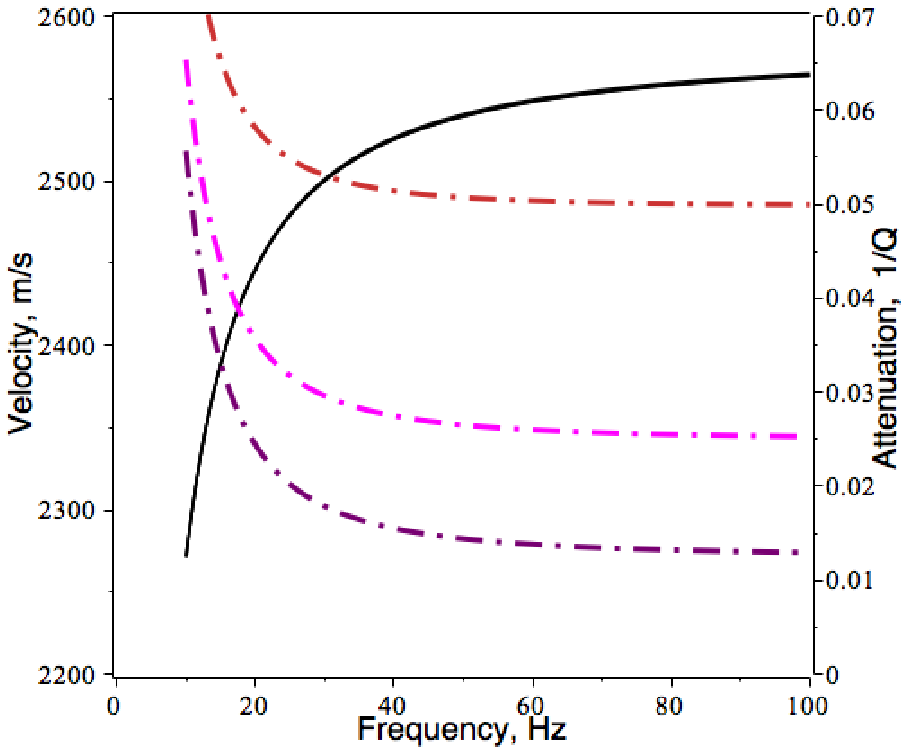

Figure 12. Velocity (solid lines) and attenuation (dot-dashed lines) vs. frequency for the fractal law for various Q-factor of the initial matrix: $Q_m = 20$ orange, $Q_m = 40$ magenta, and $Q_m = 80$ purple. Velocity has weak dependence on the matrix Q-factor, the attenuation of fractured media increase with increase of matrix Q-factor.

Effective velocity and attenuation of the fractured media are sensitive to the choice of fracture thickness. At low frequencies, thickness $h < 0.0015$ has a strong effect on the velocity and attenuation, and $h > 0.003$ has an insignificant influence on the reverse dispersion. At high frequencies, the effect of h on the same parameters is small to none. For the fractal law with fracture density $N_0 = 10^4$, the velocity dependence on frequency and fracture thickness is presented in Figure 13a and the attenuation is in the Figure 13b.

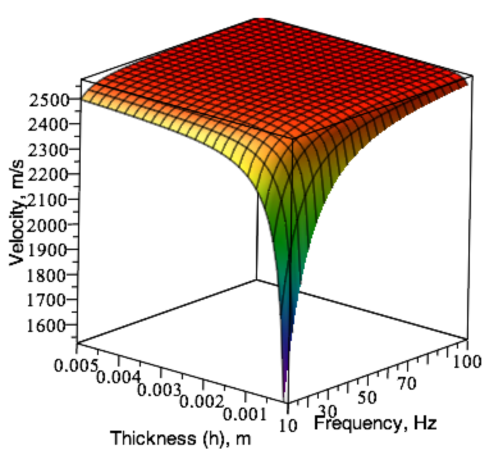

(a) Velocity from frequency and fracture thickness for the fractal law (4) and $N_0 = 10^4$. The velocity is sensetive to the fracture thickness.

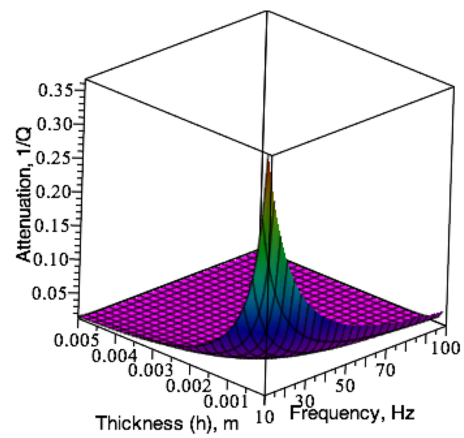

(b) Attenuation from frequency and fracture thickness for the fractal law (4) and $N_0 = 10^4$. The attenuation is sensetive to the fracture thickness.

Figure 13. Velocity (a) and Attenuation (b) from frequency and fracture thickness.

Based on the relation between the velocity and h/λ ratio, where $\lambda = V_w/2\pi f$ is the wavelength of P-wave in a liquid, the zones of a suitability of the technique can be identified for each fracture thickness h. For instance, for the $h = 10^{-3}$ in Figure 14, the effect of the guided wave presence in the green zone would be remarkable, the effects in the orange zone are small, and the effects in the gray zone are negligible. The effective average velocity is close to matrix velocity. The seismic range of frequencies ($10-100$ Hz) falls into the green zone, the lab measurements for hundreds kHz and first tens MHz fall into the orange zone, and ultrasonic data belongs to the gray zone.

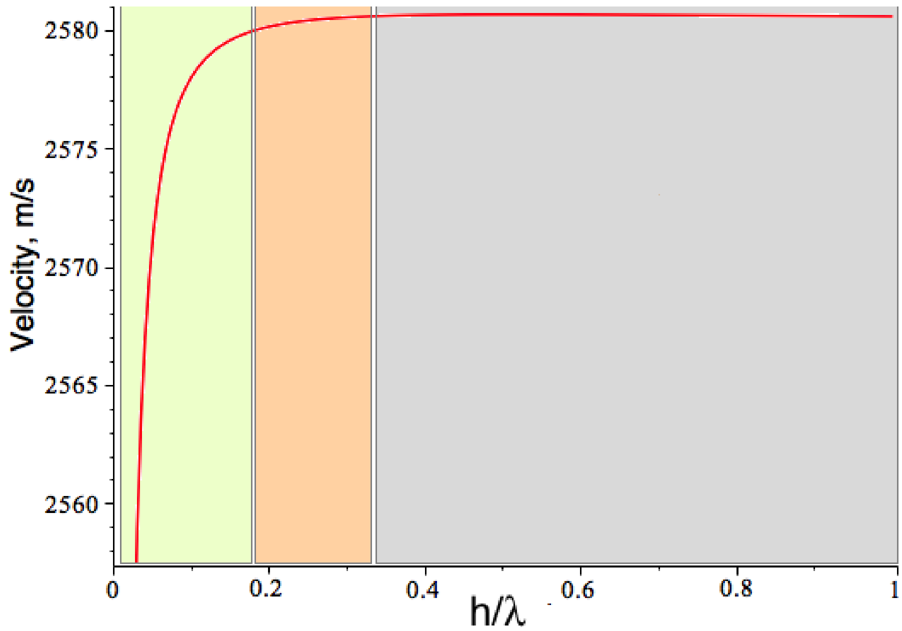

Figure 14. The velocity of the randomly fractured media from a thickness of a fracture to wavelength ratio. For the fracture thickness $h = 10^{-3}$ the low ratio (green zone) characterizes the zone of remarkable velocity dispersion due to the presence of fluid-guided wave, orange zone shows small effects from guided waves, and gray zone is where the effects can be neglected.

5 Reflectivity of fractured medium

5.1 Reflectivity of a boundary

5.1.1 Theoretical background

As a seismic wave comes across a planar interface between two half-spaces with different properties, part of it energy reflects back to the medium, some transmits to the other half-space, and some converts to another type of body waves. The amplitudes of reflected and transmitted waves for the flat boundary are described by four Zoeppritz equations depending on the angle of incidence (Zoeppritz, 1919):

$$
\begin{bmatrix} R_P \\ R_S \\ T_P \\ T_S \end{bmatrix} = \begin{bmatrix} -\sin\theta_1 & -\cos\phi_1 & \sin\theta_2 & \cos\phi_2 \\ \cos\theta_1 & -\sin\phi_1 & \cos\theta_2 & -\sin\phi_2 \\ \sin 2\theta_1 & \frac{V_{P1}}{V_{S1}}\cos 2\phi_1 & \frac{\rho_2 V_{S2}^2 V_{P1}}{\rho_1 V_{S!}^2 V_{P2}}\cos 2\phi_1 & \frac{\rho_2 V_{S2} V_{P1}}{\rho_1 V_{S1}^2}\cos 2\phi_2 \\ -\cos 2\phi_1 & \frac{V_{S1}}{V_{P1}}\sin 2\phi_1 & \frac{\rho_2 V_{P2}}{\rho_1 V_{P1}}\cos 2\phi_2 & \frac{\rho_2 V_{S2}}{\rho_1 V_{P1}}\sin 2\phi_2 \end{bmatrix}^{-1} \begin{bmatrix} \sin\theta_1 \\ \cos\theta_1 \\ \sin 2\theta_1 \\ \cos 2\phi_1 \end{bmatrix}, \quad (32)
$$

where R_P, R_S, T_P, and T_S are reflection coefficients of the reflected P, reflected S, transmitted P, and transmitted S- waves, respectively. θ_1 is the angle of incidence, θ_2 is the angle of the transmitted P-wave, ϕ_1 is the angle of the reflected S-wave, ϕ_2 is the angle of the transmitted S-wave.

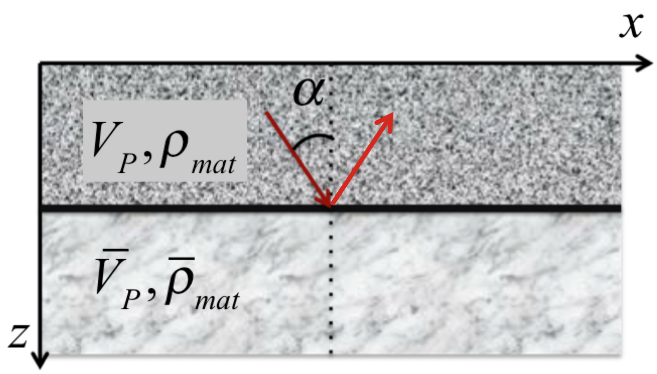

Figure 15. Schematic boundary between two half-spaces and reflection. For upper half-space: V_P is velocity and ρ_{mat} is density; For lower fractured half-space $\overline{V}_P$ is velocity and $\overline{\rho}_{mat}$ is density; α is an angle of P-wave incidence.

The exact analytic solutions by Červenỳ and Ravindra (1971) of the Zoeppritz equations (32) are used to calculate amplitude of the P-wave reflection and P-wave transmission coefficients of the plain primary wave encountering the flat interface (Figure 15):

$$R_{refl} = -1 + 2P_1 D^{-1} \left(\overline{V}_P \overline{V}_S P_2 X^2 + V_S \overline{V}_P \rho_m \overline{\rho}_m + q^2 \Theta^2 P_2 P_3 P_4 \right), \tag{33}$$

where

$$\begin{aligned}
D &= V_P \overline{V}_P V_S \overline{V}_S \Theta^2 Z^2 + \overline{V}_P \overline{V}_S P_1 P_2 X^2 + V_P V_S P_3 P_4 Y^2 \\
&\quad + \rho_m \overline{\rho}_m \left(\overline{V}_P V_S P_1 P_4 + V_P \overline{V}_S P_2 P_3 \right) + q^2 \Theta^2 P_1 P_2 P_3 P_4 \\
q &= 2 \left(\overline{\rho}_m \overline{V}_S^2 - \rho_m V_S^2 \right), \\
X &= \overline{\rho}_m - q\Theta^2, \qquad Y = \rho_m + q\Theta^2, \qquad Z = \overline{\rho}_m - \rho_m - q\Theta^2, \\
\Theta &= \sin\alpha / V_i, \qquad P_i = \left(1 - V_i^2 \Theta^2 \right)^{\frac{1}{2}}, \quad (i = 1, 2, 3, 4), \\
&V_1 = V_P, \quad V_2 = V_S, \quad V_3 = \overline{V}_P, \quad V_4 = \overline{V}_S.
\end{aligned}$$

The upper half-space is solid non-fractured matter. The lower half-space is fractured with the fractal fracture distribution (4) and the $\overline{V}_P$ and $\overline{V}_S$ are the results of averaging (29) and (31), respectively; density $\overline{\rho}_m$ is equal to the ρ of the fractured matrix. $\overline{V}_P$ is complex-valued and frequency dependent; hence, the reflection R_{refl} for fractured lower half-space is also complex-valued and frequency dependent. The use of the complex-valued velocity $\overline{V}_P$ to compute reflection coefficient R_{refl} was justified by the comparison to the complex reflection coefficient by Ren et al. (2009), where real-valued velocities are used based on theory from Trapeznikova (1985). The comparison shows that two reflection coefficient calculated with different approaches are identical.

5.1.2 Numerical illustration

Assuming the acoustic impedance distribution in the upper half-space is less than in half-space below, consider two types of the lower half-spaces. Type one is fractured half-space with the fractal fracture distribution (4), fracture density $N_0 = 10^4$, and the $\overline{V}_P$ and $\overline{V}_S$ are the results of averaging (29) and (31), respectively; density $\overline{\rho}_m$ is equal to the ρ of the fractured matrix. Type two is the homogeneous half-space with the properties of the matrix without fractures: $V_P = 2580$ m/s, $V_S = 1290$ m/s, density $\rho = 2300$ kg/m^3. Figure 16 is an illustration of the normal incident angle reflection coefficient. For the homogeneous type (black dashed line): the boundary is between two homogeneous half-spaces with different properties, and amplitude of the reflection coefficient is frequency independent. For the fractured case (red solid line) the reflection coefficient from the boundary depends on frequency.

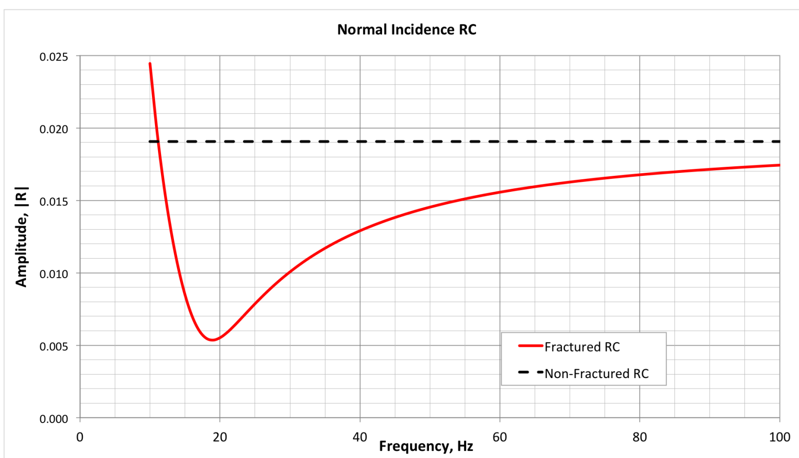

Figure 16. Amplitudes of normal incidence reflection coefficients from fractured (red solid) and homogeneous (black dash) cases.

The comparison of the traces in Figure 17 provides a possible explanation to the frequency shadows beneath fluid-saturated zones. The detailed analysis and the development of this methodology regarding frequency shadow phenomena might be a possible direction of the future work.

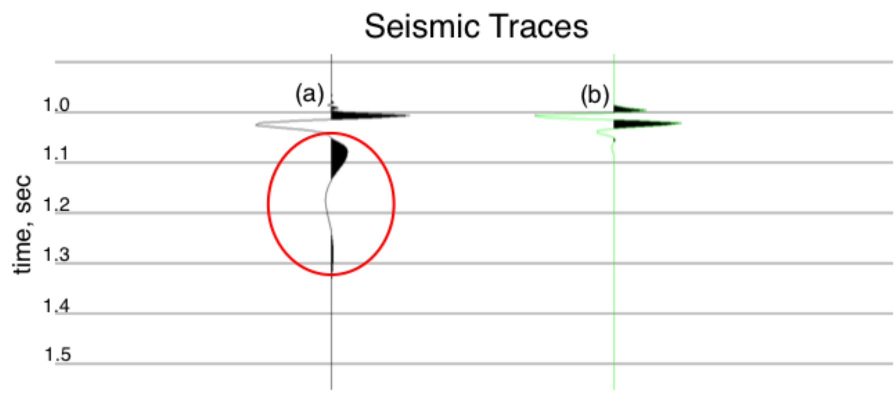

Figure 17. Normal incidence reflection in the time domain from (a) fractured and (b) elastic non-fractured half-spaces.

In Figure 18 there are three curves for fractured case, for frequencies $f = 10$ Hz (red), $f = 20$ Hz (blue), and $f = 30$ Hz (black), and one curve (magenta) for the homogeneous, due to independent from frequency reflective behavior. The 10Hz fractured curve differs the most in behavior from the frequency independent non-fractured curve.

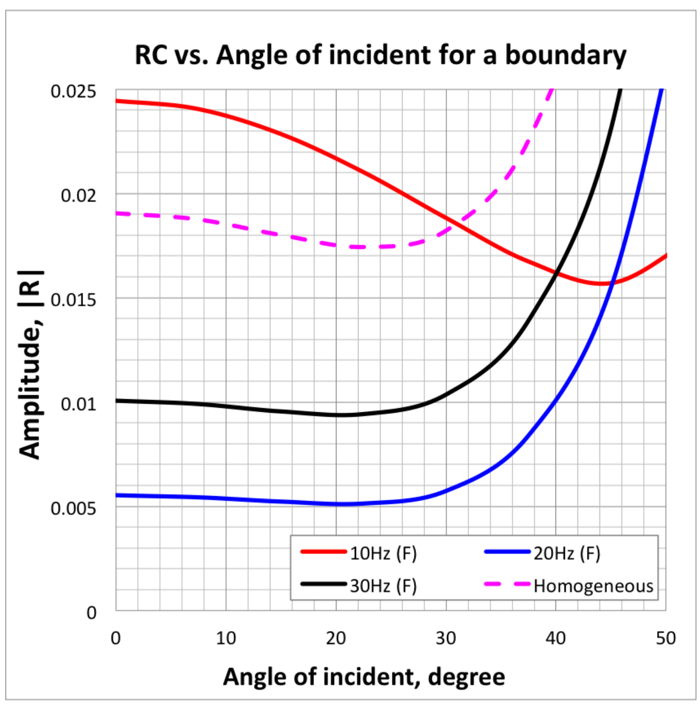

Figure 18. Amplitudes of angular dependent reflection coefficients for fractured case $f =$ 10 Hz (red), $f = 20$ Hz (blue), $f = 30$ Hz (black) and frequency-independent homogeneous (dashed magenta).

5.2 Reflectivity of a layer

5.2.1 Theoretical background

Two combined planar interfaces create a layer between two parallel boundaries. The seismic wave also can be reflected, transmitted from the layer, and change properties within it. Consider a P-wave confronting a layer with the thickness d between two isotropic half-spaces (Figure 19). The velocity $\overline{V}_{P_2}$ differs from velocities $\tilde{V}_{P_1}$ and $\tilde{V}_{P_3}$ of half-spaces above and below. The complex valued reflection coefficient of the plain wave from the horizontal layer at the frequency ω and incident angle α can be written as modified formula of (Brekhovskikh, 1960), taking into an account the complex acoustic impedance ($\overline{V}_{P_2} \in \mathbb{C}$):

$$R(\omega,\alpha) = \frac{R_1(\omega,\alpha) + R_2(\omega,\alpha)\exp\left(-i\omega\Delta t\cos\alpha_2\right)}{1 + R_1(\omega,\alpha)R_2(\omega,\alpha)\exp\left(-i\omega\Delta t\cos\alpha_2\right)}, \tag{34}$$

where $\Delta t = 2d/\overline{V}_{P_2}(\omega)$ is the time thickness of the layer and $\overline{V}_{P_2}(\omega)$ is the effective velocity of the fractured or homogeneous layer; α_2 is the reflection angle from the lower inter-phase; $R_1(\omega,\alpha)$ and $R_2(\omega,\alpha)$ are the reflection coefficients from the upper and lower boundary, respectively, computed with analytic solutions (33) by Červenỳ and Ravindra (1971).

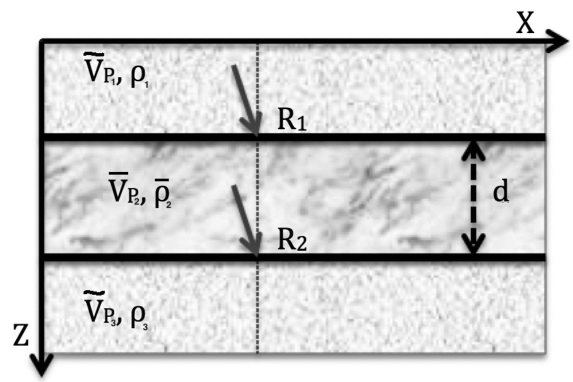

Figure 19. Scheme of the layers. Upper and lower half-spaces are non-fractured with velocities $\tilde{V}_{P_1}$ and $\tilde{V}_{P_3}$ and densities ρ_1 and ρ_3, respectively. Middle layer with thickness d is fractured with velocity $\overline{V}_{P_2}$ and density $\overline{\rho}_2$. R_1 and R_2 are angular and frequency dependent reflection coefficients from the upper and lower boundary, respectively.

The amplitude and phase of the reflection coefficient (34) from the layer is defined by:

$$\left|R(\omega,\alpha)\right| = \sqrt{(\Re(R(\omega,\alpha)))^2 + (\Im(R(\omega,\alpha)))^2}, \tag{35}$$

$$\Theta(\omega,\alpha) = \arctan\left(\frac{\Im(R(\omega,\alpha))}{\Re(R(\omega,\alpha))}\right), \tag{36}$$

where $\Re$ and $\Im$ are real and imaginary parts of the reflection coefficient (34).

5.2.2 Numerical examples

As it was discussed in the Section 4.2, numerical simulations demonstrate remarkable velocity dispersion and attenuation of the P-wave in fractured media (Figure 10) for any given law of random fracture distribution (1-4); hence, the computational results would indicate abnormal reflection coefficients of fractured layers. Beneath the surface, layers can have complex nature and geometry. In Geophysical industry, simplified models are used, where their acoustic impedance describes subsurface layers.

In seismic range of frequencies ($10-100$ Hz), the theory above was applied to three synthetic scenarios of the acoustic impedance distribution in layers (Figure 20); however, the parameters for the target (middle) layer remained the same in all cases: $\tilde{V}_{P_2} = 2580$ m/s, $\tilde{V}_{S_2} = 1290$ m/s and $\rho_1 = 2400$ kg/m^3. For each case, calculations were made for two widths of fractured layer ($d = 20$ m and $d = 50$ m). As any of random fracture distribution laws can be applicable, for simplicity, all calculations were made for the fractal distribution law with the fracture density 10^4. The expressions (23), the limitations on the fracture length, for the seismic range of frequencies, P-wave and Krauklis wave velocities indicate $L_{min} = 2$ m and $L_{max} = 257$ m for constant fracture thickness of $h = 10^{-3}$, which is consistent with aspect ratios $\alpha_{min} = 5\cdot 10^{-4}$ and $\alpha_{max} = 4\cdot 10^{-6}$, respectively. Results of calculations for fractured layers were compared to the homogeneous layers with $V_{P_2} = 2580$ m/s, $V_{S_2} = 1260$ m/s and $\rho_2 = 2400$ kg/m^3 for the same range of frequencies and same width.

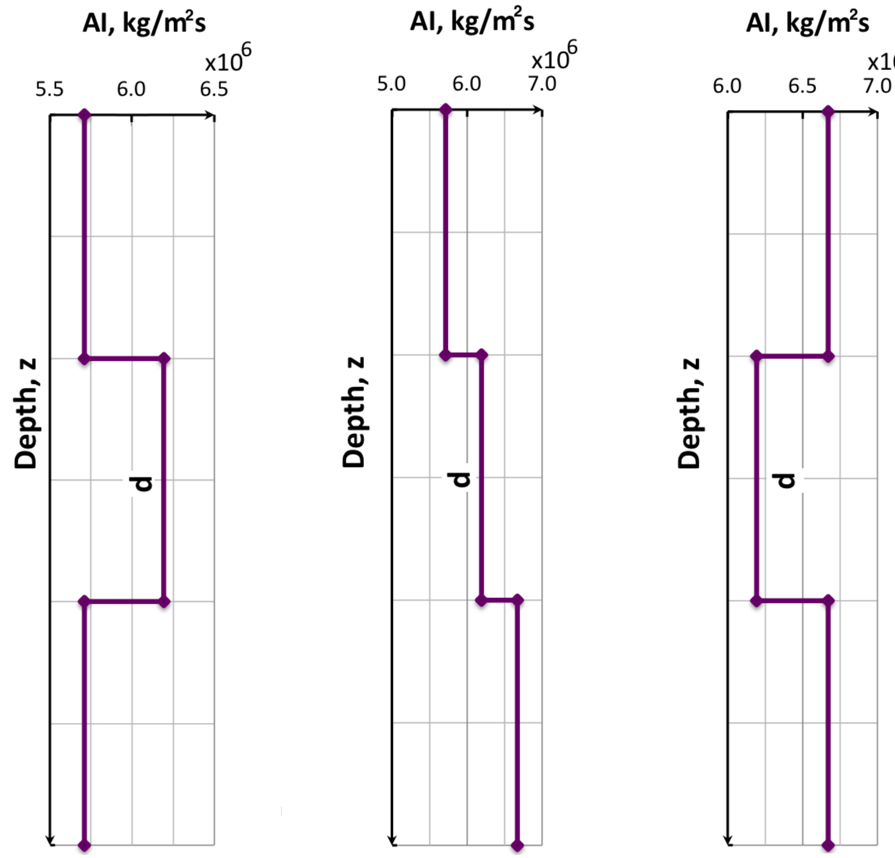

(a) $AI_1 = AI_3 < AI_2$. **(b)** $AI_1 < AI_2 < AI_3$. **(c)** $AI_1 = AI_3 > AI_2$.

Figure 20. Schemes of acoustic impedance distribution for the layers with the thickness d. (a) High acoustic impedance layer ($AI_1 = AI_3 < AI_2$); (b) Intermediate acoustic impedance ($AI_1 < AI_2 < AI_3$); (c) Low acoustic impedance layer ($AI_1 = AI_3 > AI_2$). The acoustic impedance of the layer AI_2 remains the same in all cases and equal to $6.2 \cdot 10^6$ kg/m^{2}s.

Case 1

For the first case (Figure 20a), the half-space above and below the layer have P-wave velocity $\tilde{V}_{P_1} = \tilde{V}_{P_3} = 2380$ m/s, S-wave velocity $\tilde{V}_{S_1} = \tilde{V}_{S_3} = 1190$ m/s and density $\rho_1 = \rho_3 = 2400$ kg/m^3. This case is an illustration of the “dim spot” in terms of the AVO analysis (Castagna and Backus, 1993; Hilterman, 2001). The reduction of the amplitudes for the fractured layers at the low frequency characterizes frequency dependent tuning effect for such acoustic impedance distribution.

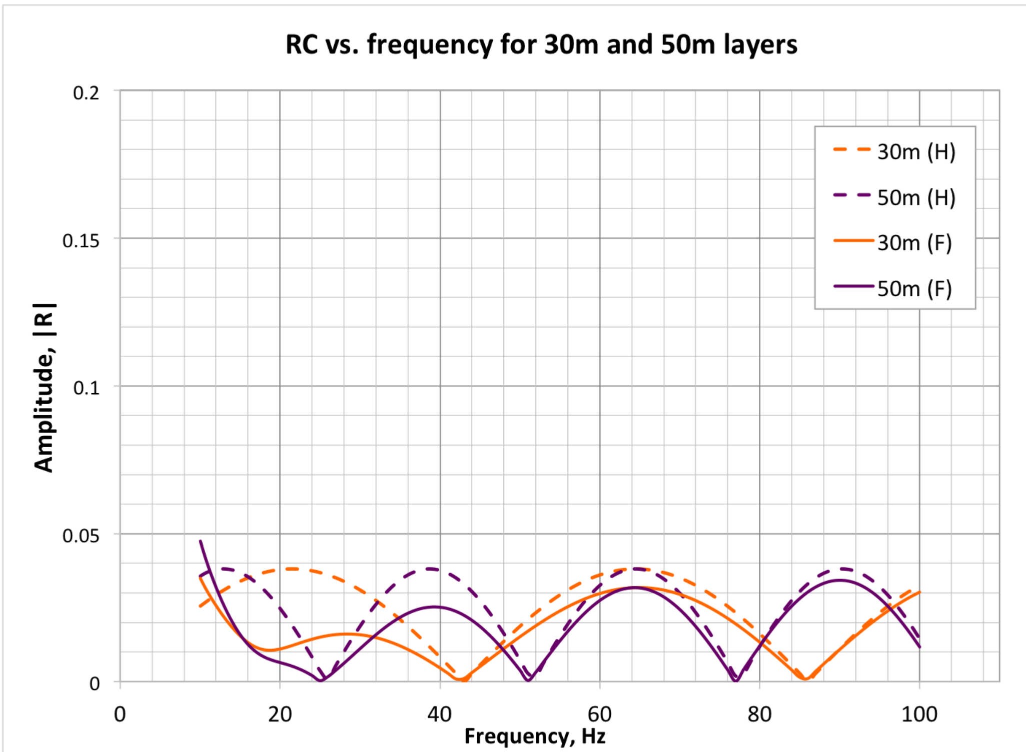

Figure 21. Amplitudes of the normal incident reflection coefficients vs. frequency for AI distribution (Figure 20a). Dashed lines represent homogeneous cases, solid lines referred to fractured cases. Orange is the 30 m thick layer, purple is the 50 m thick layer.

To estimate the difference of the fractured reflection coefficients versus non-fractured reflection coefficients for both thicknesses (Figure 22), the relative ratio was used:

$$Relative\ Ratio = \frac{2|RC_F - RC_H|}{RC_F + RC_H} \cdot 100\%, \tag{37}$$

where RC_F and RC_H are normal reflection coefficients from fractured and non-fractured layer, respectively. Vertical parts of the curve correspond to minimums on Figure 21, between of them, the flatter and closer to 0 relative ratios, smaller the difference of fractured and non-fractures RC's.

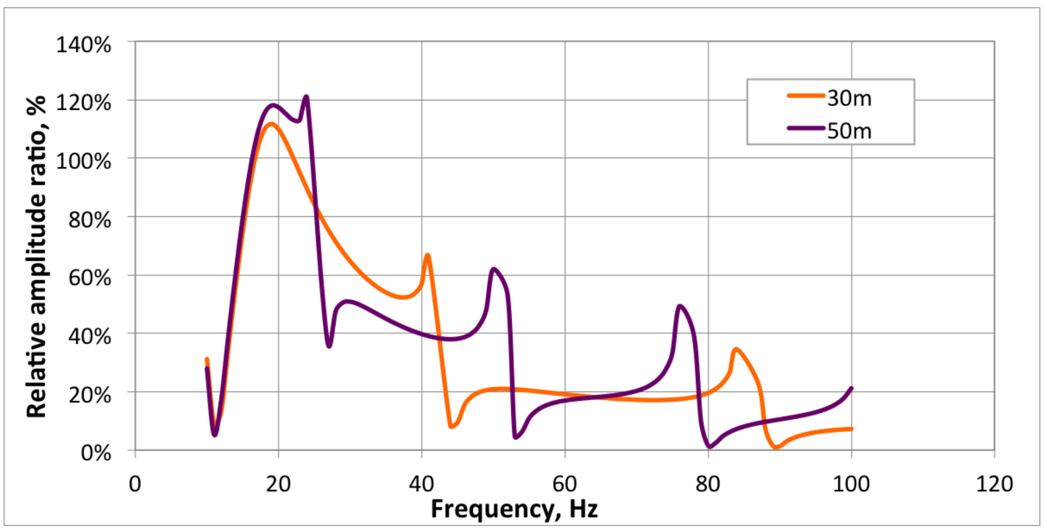

Figure 22. Relative amplitude ratio between fractured and non-fractured layers. Orange is the 30 m thick layer, purple is the 50 m thick layer. The relative ratio is closer to 0 for the smaller difference of fractured and non-fractured RC's. Vertical parts of the curve correspond to minimums on Figure 21.

The angular reflection coefficients for the 30 m layer (Figure 23a) and for the 50 m layer (Figure 23b) show the greatest difference between RC is achieved for the lowest frequency 10 Hz.

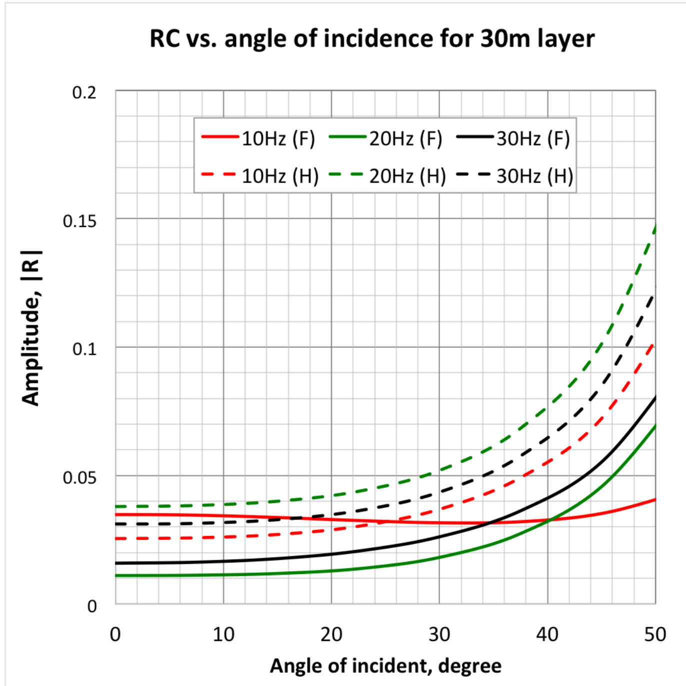

(a) For the $d = 30$ m layer.

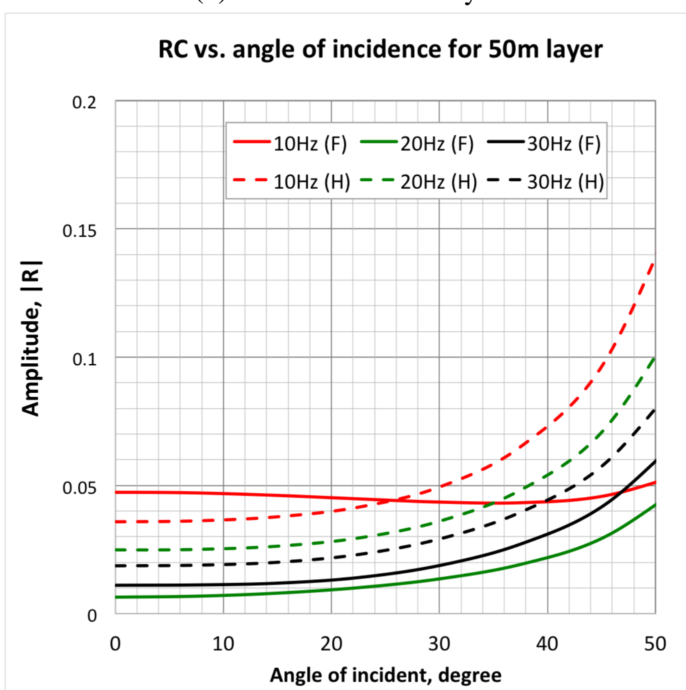

(b) For the $d = 50$ m layer.

Figure 23. Amplitudes of the normal incident reflection coefficients vs. frequency for AI distribution (Figure20a). Legend: reds for $f = 10$ Hz, greens for $f = 20$ Hz, and blacks for $f = 30$ Hz; solid lines are the fractured layers, dashed lines are homogeneous isotropic layers.

Case 2

The second case (Figure 20b) represents an increase in acoustic impedance from the upper half-space down. The half-space above the layer has P-wave velocity $\tilde{V}_{P_1} = 2380$ m/s, S-wave velocity $\tilde{V}_{S_1} = 1190$ m/s and density $\rho_1 = 2400$ kg/m^3; the half-space below have P-wave velocity $\tilde{V}_{P_3} = 2780$ m/s, S-wave velocity $\tilde{V}_{S_3} = 1390$ m/s and density $\rho_3 = 2400$ kg/m^3, the middle layers remains with the same properties.

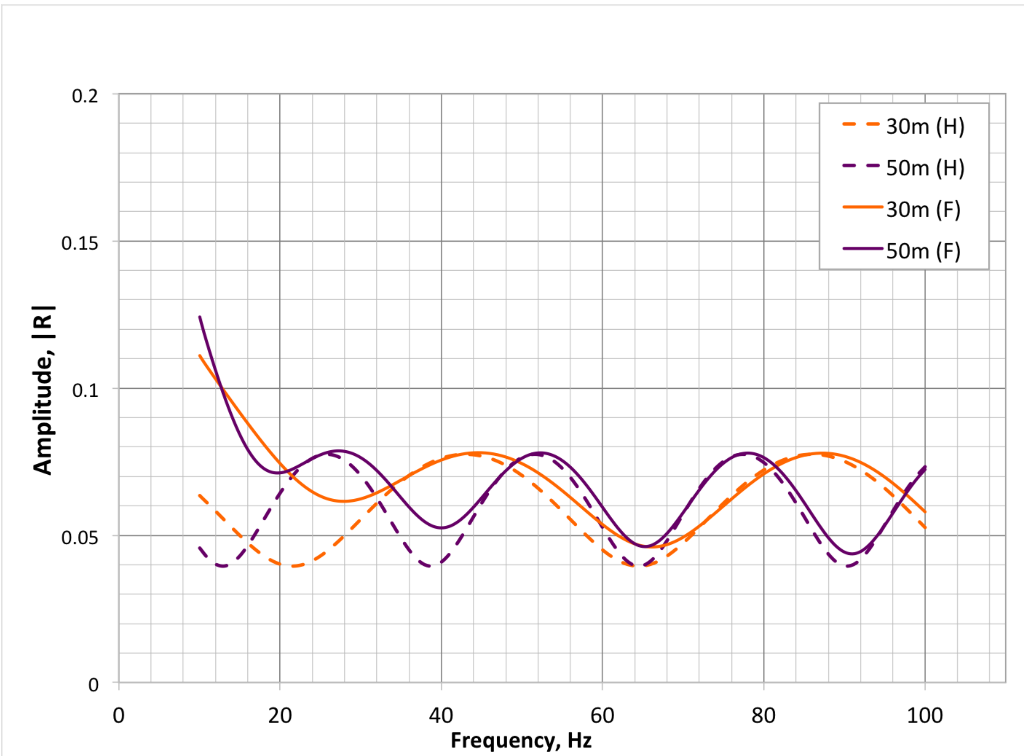

Figure 24. Amplitudes of the normal incident reflection coefficients vs. frequency for AI distribution (Figure 20b). Dashed lines represent homogeneous cases, solid lines referred to fractured cases. Orange is the 30 m thick layer, purple is the 50 m thick layer.

The amplitudes of the tuning effect associated with the layer width for fractured layer differs from the homogeneous layer amplitudes: the amplitudes of the fractured layers are decreasing at lower frequencies, and the local maxima (minima) of the amplitudes are shifted right from the location of homogeneous critical points.

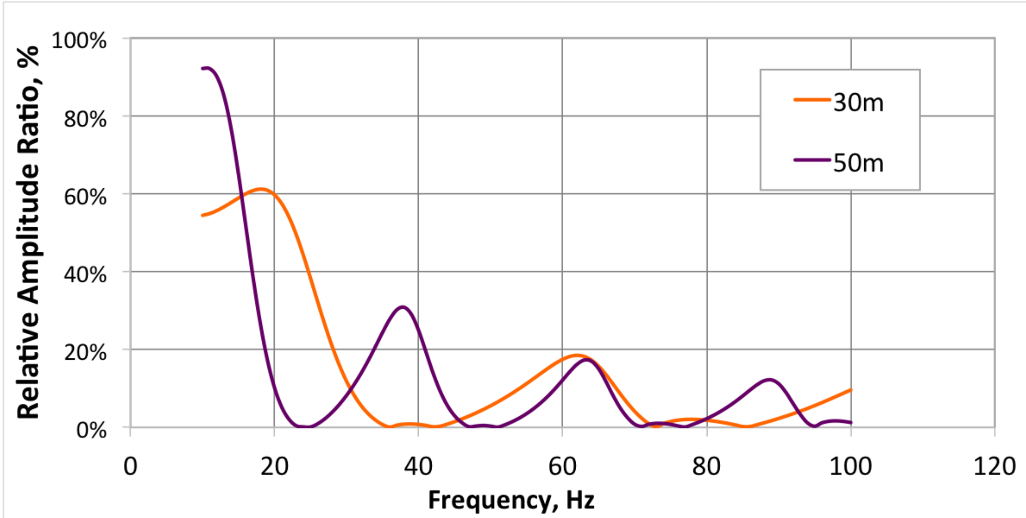

Figure 25. Relative amplitude ratio between fractured and non-fractured layers. Orange is the 30 m thick layer, purple is the 50 m thick layer. Zero values correspond to tuning maxima, and the picks on curves indicate the highest difference in reflection coefficient amplitudes on Figure 24.

To estimate the difference of the fractured reflection coefficients versus non-fractured reflection coefficients for both thicknesses (Figure 25), the relative ratio (37) was used. In Figure 25, zero values correspond to tuning maxima, and the picks on curves indicate the highest difference in reflection coefficient amplitudes.

For angular dependent RC (Figure 26) with the increase of the layer width, from 30 m to 50 m, greater become the amplitude difference for the low-frequency curve of 10 Hz.

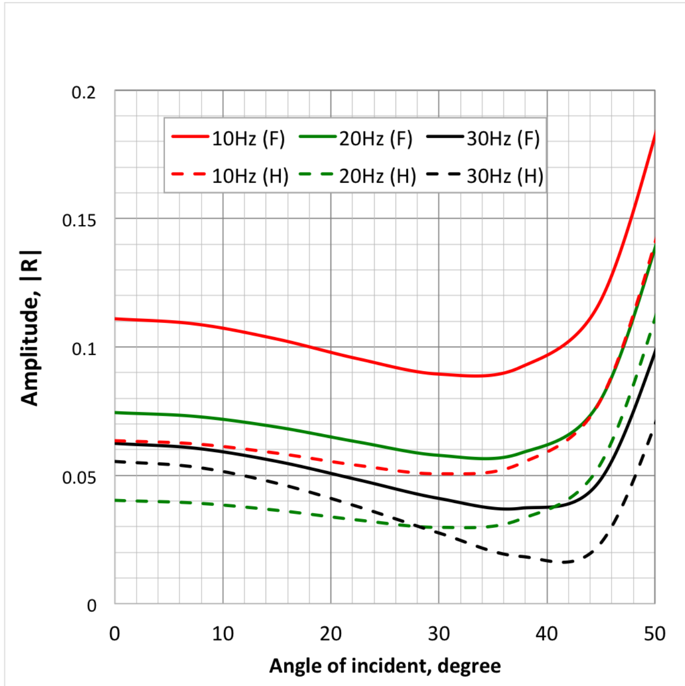

(a) For the $d = 30$ m layer.

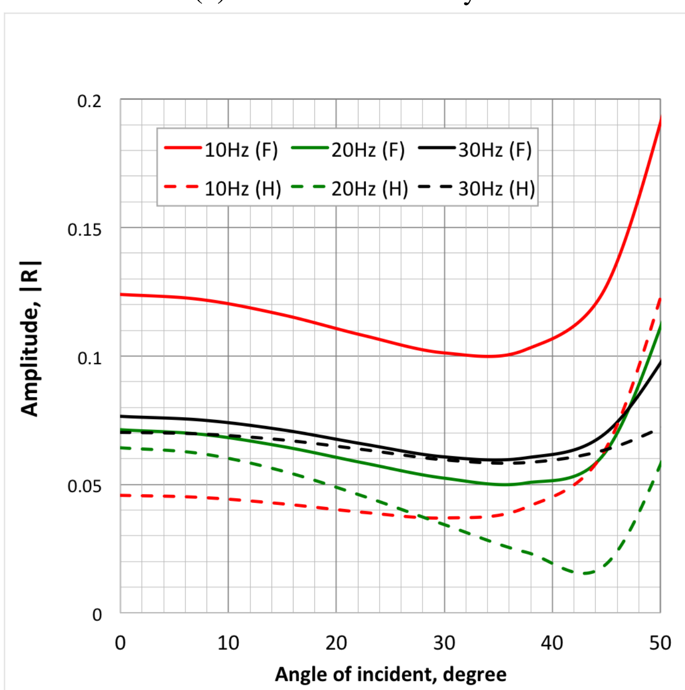

(b) For the $d = 50$ m layer.

Figure 26. Amplitudes of the normal incident reflection coefficients vs. frequency for AI distribution (Figure 20b). Legend: reds for $f = 10$ Hz, greens for $f = 20$ Hz, and blacks for $f = 30$ Hz; solid lines are the fractured layers, dashed lines are homogeneous isotropic layers.

Case 3

In the third case (Figure 20c), the layer has the lowest impedance compared to the half-spaces and represents the "bright spot" in the AVO theory (Castagna and Backus, 1993; Hilterman, 2001). The half-spaces have P-wave velocity $\tilde{V}_{P_1} = \tilde{V}_{P_3} = 2780$ m/s, S-wave velocity $\tilde{V}_{S_1} = \tilde{V}_{S_3} = 1390$ m/s and density $\rho_1 = \rho_3 = 2400$ kg/m^3. In fractured layers tuning amplitudes decay with the increase of frequency, and local extrema of the amplitudes are shifted left from of homogeneous curve extrema.

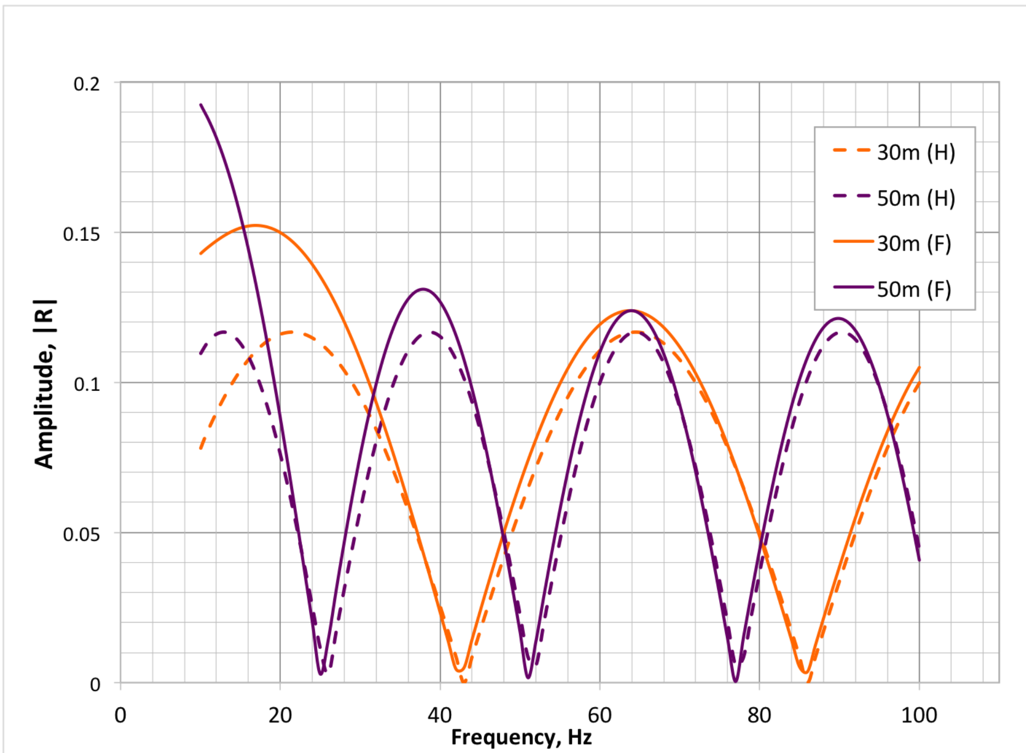

Figure 27. Amplitudes of the normal incident reflection coefficients vs. frequency for AI distribution (Figure 20c). Dashed lines represent homogeneous cases, solid lines referred to fractured cases. Orange is the 30 m thick layer, purple is the 50 m thick layer.

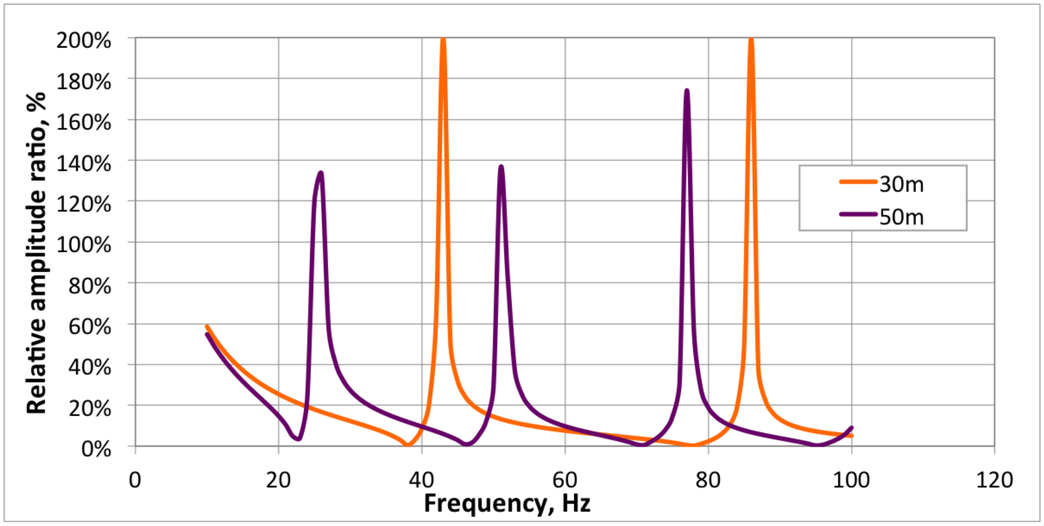

Figure 28. Relative amplitude ratio between fractured and non-fractured layers. Orange is the 30 m thick layer, purple is the 50 m thick layer. The relative ratio is closer to 0 for the smaller difference of fractured and non-fractured RC's. Picks correspond to the tuning minima.

The difference of the fractured reflection coefficients versus non-fractured reflection coefficients was estimated for both thicknesses (Figure 25), using the relative ratio (37). On Figure 28, 0 relative ratios are consistent with frequencies, where RC's of fractured equals to non-fractured. Picks correspond to the tuning minima, and, similar to the case one, the flatter curves between picks, smaller relative ratios, smaller the difference of fractured and non-fractures RC's.

The same observations as for Case 1 and Case 2 are held for the angular dependent reflection coefficients (Figure 29): the greatest variation in amplitudes of the reflection coefficients present for the lowest frequency 10 Hz.

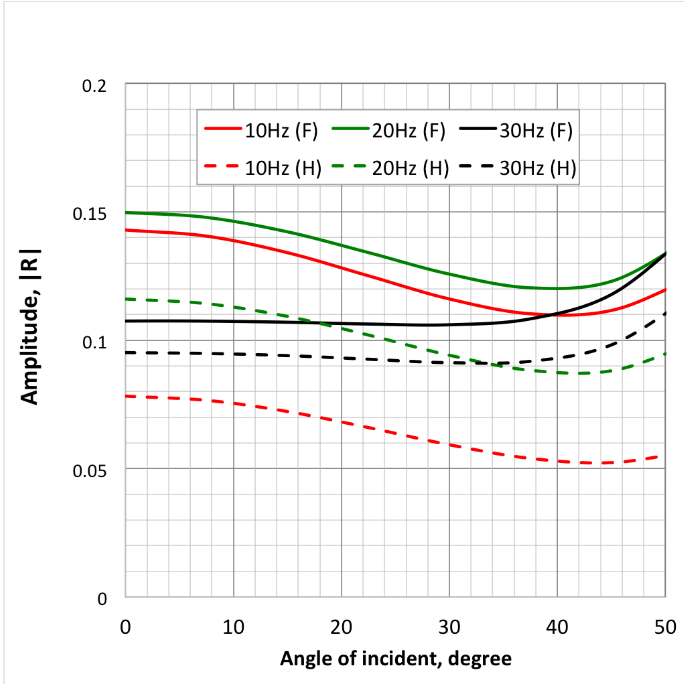

(a) For the $d = 30$ m layer.

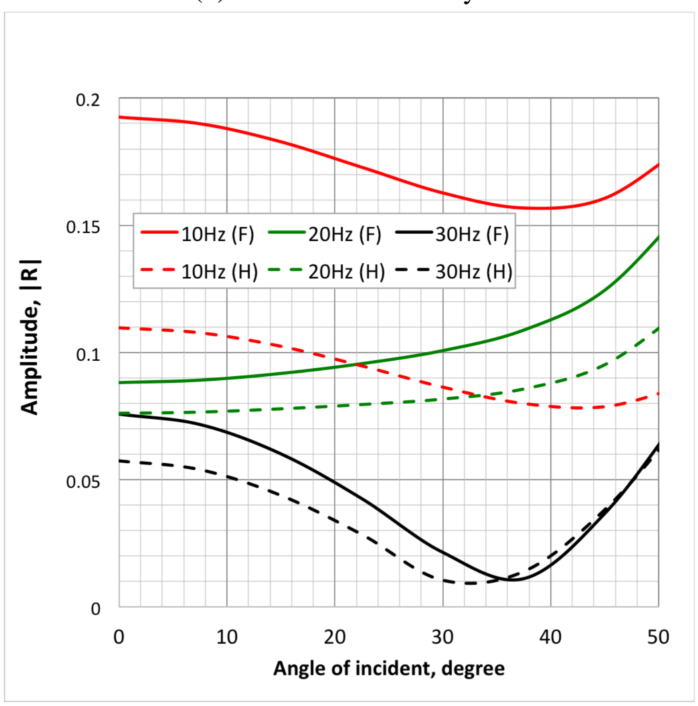

(b) For the $d = 50$ m layer.

Figure 29. Amplitudes of the normal incident reflection coefficients vs. frequency for AI distribution (Figure 20c). Legend: reds for $f = 10$ Hz, greens for $f = 20$ Hz, and blacks for $f = 30$ Hz; solid lines are the fractured layers, dashed lines are homogeneous isotropic layers.

In cases of fractured layer, the amplitude variations vs. angle of incident are different relatively to the homogeneous layer. At low frequencies, in particular at 10 Hz, the amplitude of the reflection coefficient from the fractured layer dominates for normal angle of incidence (Figure 21, 24, 27) and differs for any angle of incidence (Figure 23, 26, 29) for all cases of the acoustic impedance distribution.

The constructive or destructive interference of the P-wave from the layer's boundaries plays significant role in seismic analysis. The tuning effect is evident for fractured and homogeneous layers. Tuning effects in homogeneous cases are characterized by equal amplitude for each variation of AI distribution and by an equidistant spread of maxima (minima) for each of two layers ($d = 30$ m and $d = 50$ m). However, for the fractured cases, tuning effects are frequency dependent and do not coincide with homogeneous curves. The drastic change of tuning amplitudes and shift of reflection coefficient curves for fractured medium appear to be at low frequencies.

6 Analysis of experimental data

In the following Chapter, the applicability of the proposed theoretical approach is examined on the real experimental data taking into account the assumptions of this work (recall Introduction). The first example, the gas storage monitoring, is the mostly agree with assumptions: the randomly fractured dolomite alternately saturated with liquid gas and water, fracture thickness to wavelength (h/λ) relation was small, and crack porosity is high (Daley et al., 2000). The second example partially fit the assumptions, because of the data from the shale reservoir of Bazhenovskaya formation that has anisotropic properties. Despite the presence of the anisotropy, the aim was to justify interpretation by the proposed technique only in one direction of the wave propagation, normal to the layer. The third example mostly did not fit to the assumptions, it covers laboratory measurements with high thickness to wavelength (h/λ) ratio of highly porous anisotropic material. Due to the sample nature, different mechanisms might govern the wave propagation (e.g. Biot-Gassmann, etc..), as well as different attenuation phenomenon (i.e. scattering). The consideration of such example is fueled by the interest of comparison how distant is the prognoses of the one-directional velocity from the same-direction values, measured in the experiment.

6.1 Monitoring of gas storage

For the field-scale example is used the VSP data gathered at a natural gas storage field in Indiana by Lawrence Berkeley National Laboratory (LBNL). The reservoir conditions are changing seasonally from predominantly gas saturated in summer to being predominantly water saturated in winter (Korneev et al., 2004), thus the VSP survey performed in 1996-1997 as a time-lapse study. Before the analysis of the data using the proposed methodology (See Section 4), the background of the experiment by Daley et al. (2000), would be recalled.

Background

The Northern Indiana Public Service Company (NIPSCO) operates naturally fractured reservoirs in Royal Center field, Indiana (Figure 30) for seasonal storage of natural gas. The injection of the gas starts in summer. By the winter of 1996, when the first acquisition was made, the pressure in the reservoir increased to the near maximum values of about 400 psi. The extraction takes place during winter when gas is naturally substituted by the Trenton formation water, which has pressure about 310 psi. By the May 1997 the reservoir gas pressure was reduced to 250 psi, and reservoir could be considered mostly water flooded.

The Paleozoic Ordovician Trenton formation dolomite is the part of the Royal Center field stratigraphy, which is dominated by shale and carbonates (Figures 31). The Trenton Formation is overlain by a section of the Ordovician Eden Group shale, Ordovician-age limestone, Silurian-age limestone and shale, and Pleistocene gravel (Dawson and Carpenter, 1963; Goloshubin et al., 2001). The field operators believe that the top and bottom section of the Trenton Dolomite is unfractured and forms a cap for the reservoir. The thickness of the fractured reservoir is 9 m (Korneev et al., 2004).

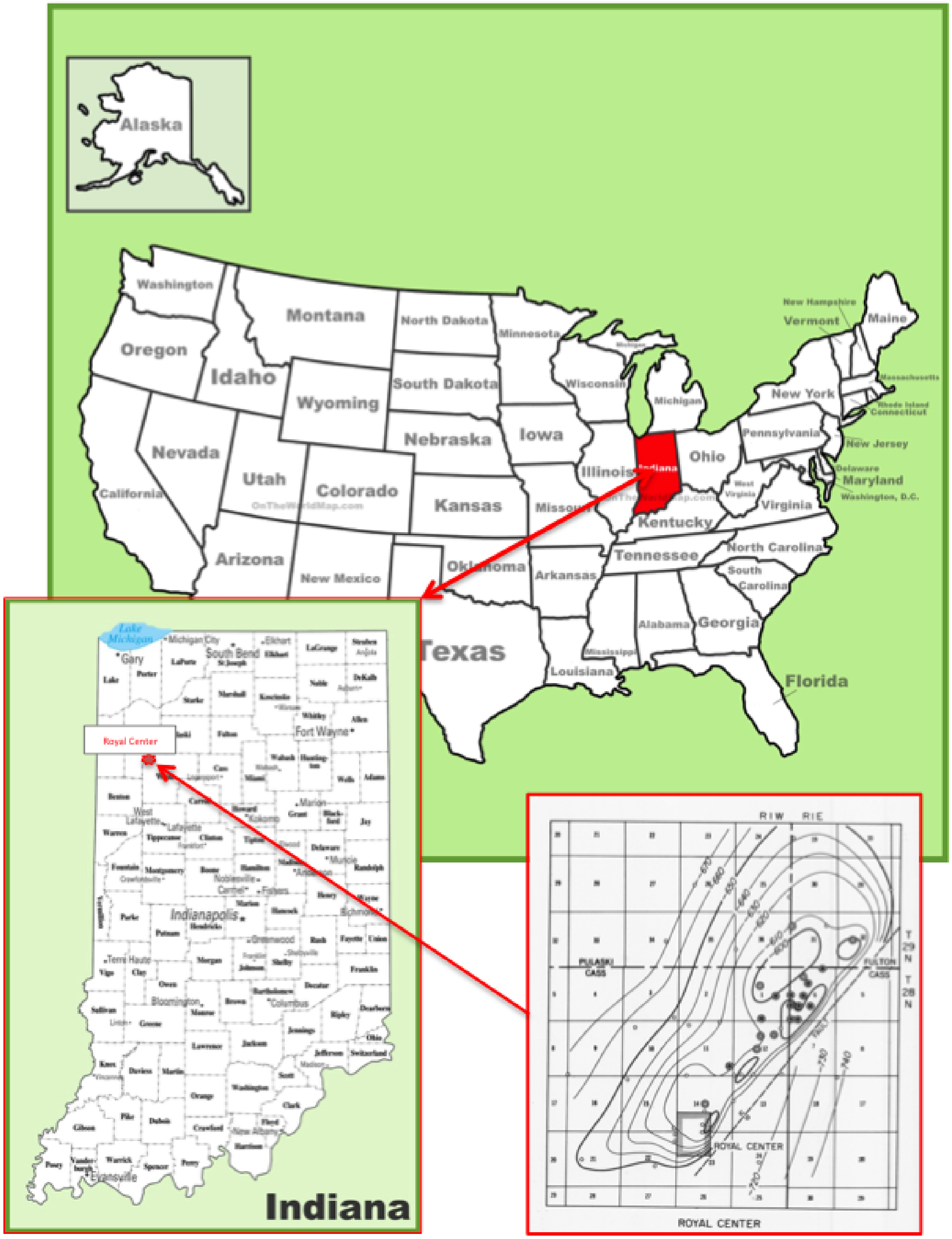

Figure 30. Location of the Royal Center field, Indiana. *Source www.ontheworldmap.com and Dawson and Carpenter (1963).*

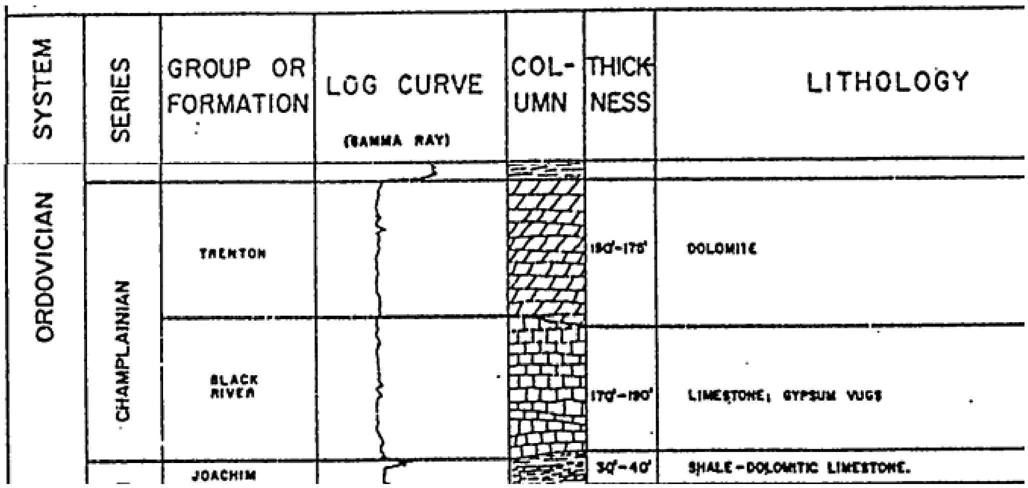

Figure 31. The Ordovivian part of geologic column for the Royal Center field. The approximate depths of Silurian limestone and shale are 150-675 ft (46-205 m), Eden shale is 675-930 ft (205-283 m), Trenton dolomite is 930-1100 ft (283-335 m). *Modified after Daley et al. (2000).*

The time-lapse VSP consisted of two phases at the field site (in December 1996 and May 1997), with essentially identical acquisition geometry (i.e. source and receiver locations) under distinctly different reservoir conditions. According to Korneev et al. (2004), there were four, nine-component VSP data sets acquired, plus a walkaway VSP. The sensors were three-component, wall clamping geophones (with a 14 Hz corner frequency) in a five level string with 2.4 m spacing between sensor depths. The vibroseis sources (both P- and S- wave) used a 12 to 99 Hz sweep, 12 s long and with a 3 s listen time recorded at a 1 μs sample rate. The May 1997 survey conditions duplicated the first one in December 1996.

Frequency-dependent analysis of field VSP data

In Figure 32 the downgoing wavefield illustrates good data resemblance of data from both surveys. Korneev et al. (2004) noted no differences between the 1996 and 1997 downgoing wavefields (as indicated by the conventional analysis); however, observed some differences between 1996 and 1997 upgoing wavefields (Figure 33). More precisely, the reservoir zone reflection wave traces has change (Figure 33b).

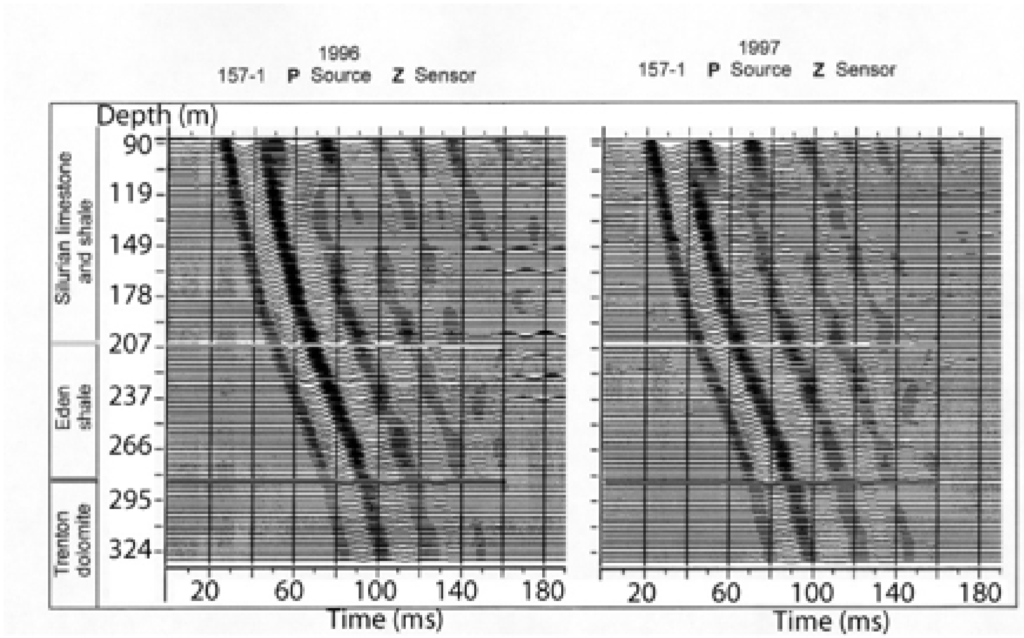

(a) Downgoing wavefields.

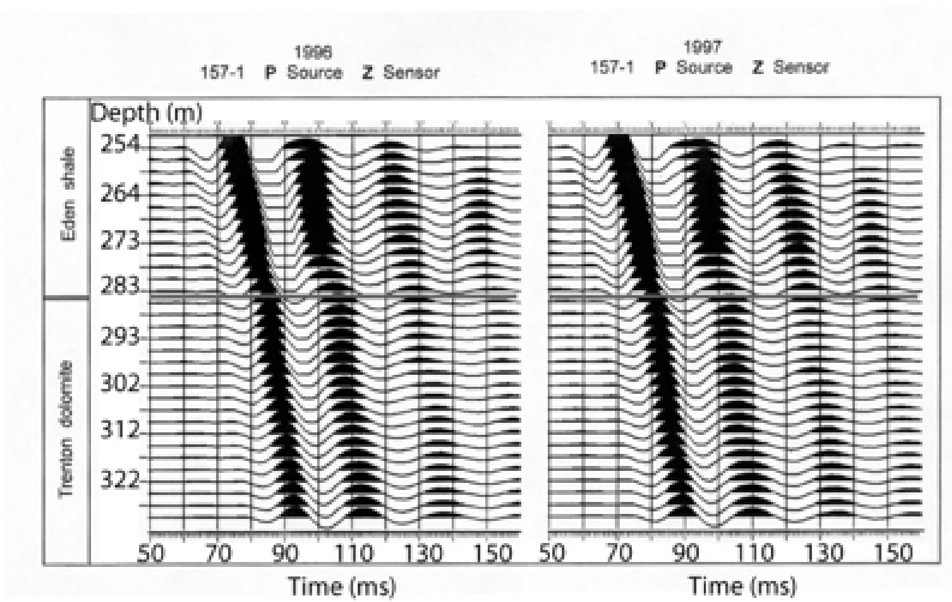

(b) Zoom of the traces on the 254 to 332 m depth interval.

Figure 32. Downgoing wavefields for 1996 (left) and 1997 (right) show no visible changes, except a constant time shift associated with near-surface effects.

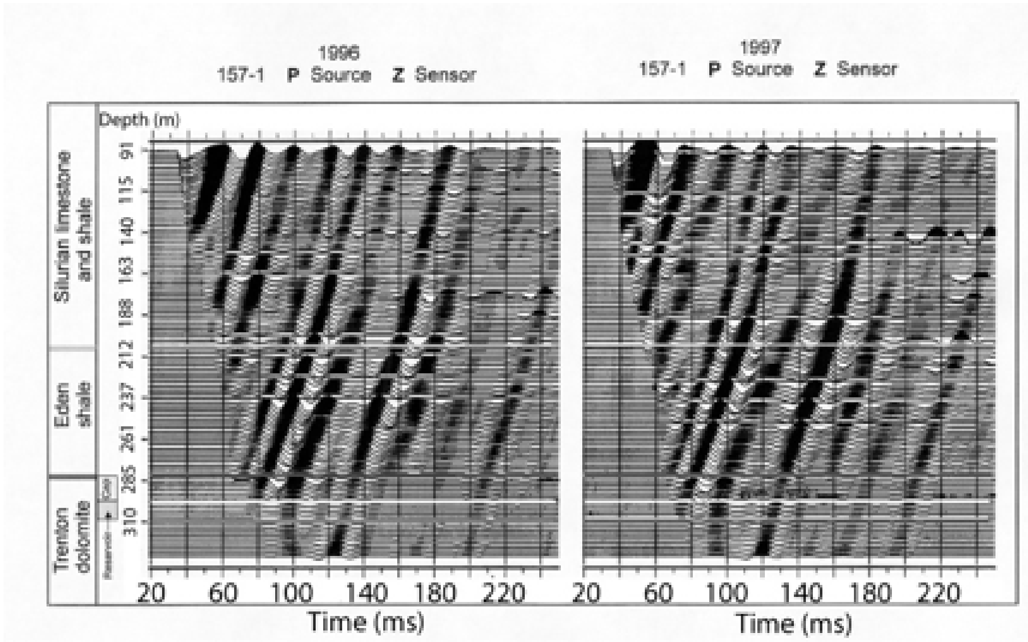

(a) Upgoing wave fields.

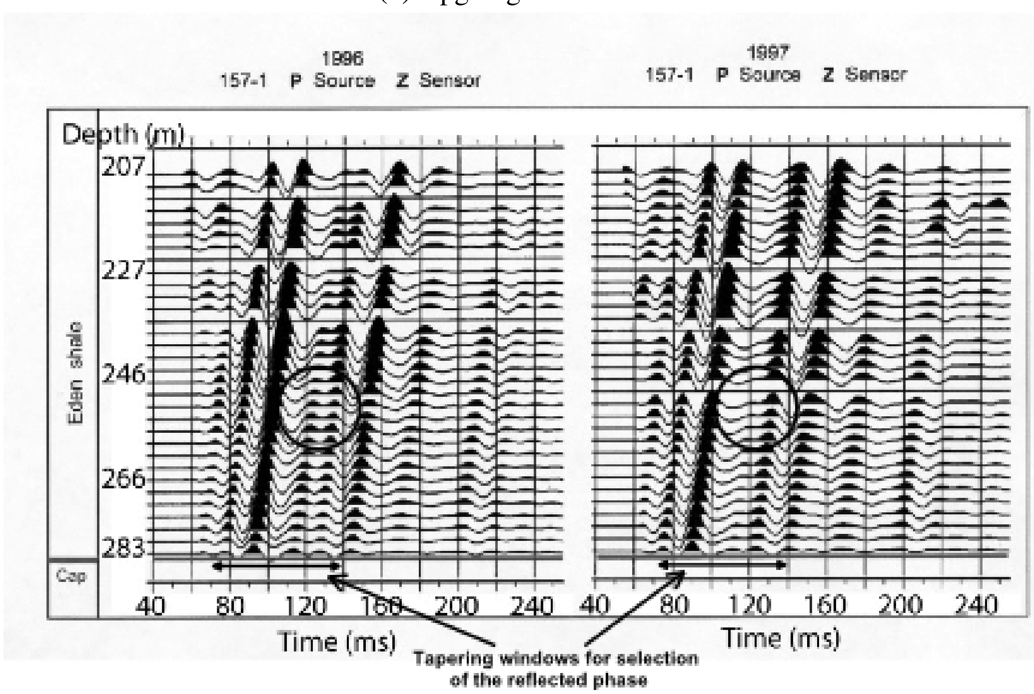

(b) Zoom of the traces on the 207 to 283 m depth interval.

Figure 33. Upgoing wavefields for 1996 (left) and 1997 (right) reveal low-frequency changes for reflections from the Trenton Dolomite.

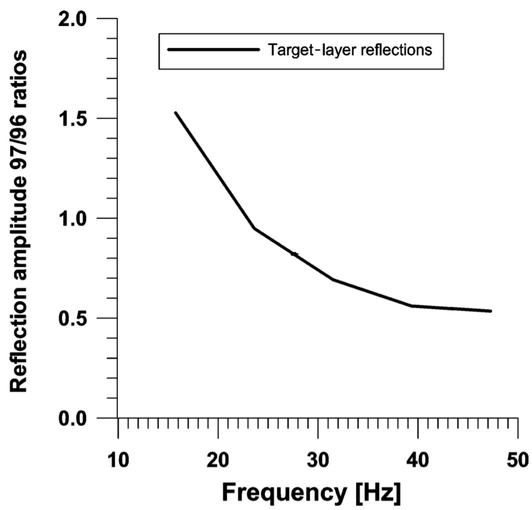

(a) Spectral amplitude ratios of water-saturated (1997) to gas-saturated (1996) data. The curves were computed using amplitude spectra of reflected phases. Reflections from the reservoir (solid line).

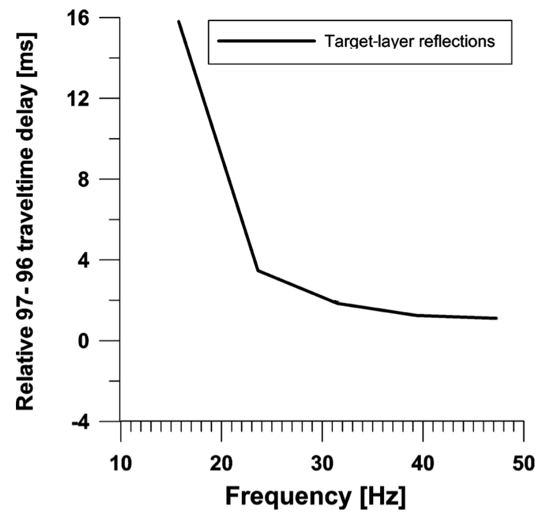

(b) Traveltime delays of water-saturated case (1997) data compared with the gas-saturated (1996) case data. The curves are computed from the argument of the complex spectral ratios. Delays for reservoir reflection (solid line).

Figure 34. Experimental data (Korneev et al., 2004)

The reflectivity analysis from Chapter 5 was applied to 9 m fractured reservoir in the Trenton formation, characterized by dolomites with relatively high velocities $V_p = 5500$ m/s, $V_S = 2895$ m/s, dolomite density $\rho = 2850$ kg/m^3, and formation factor $Qm = 100$ (Daley et al., 2000). The fracture distribution of the reservoir assumed to be governed by the fractal law (4) with fracture density constant $N_0 = 10^4$ due to abnormally high estimation of the crack density (0.27%) in the initial report. For the 1997 data, which consistent with water almost fully water saturated reservoir, the presence of Krauklis wave in fractures was considered. For gas saturated 1996 data the effect of the Krauklis wave on the reflectivity is poor, due to liquefied gas properties ($\rho_g = 300$ kg/m^3, $\eta_g = 34.2 \cdot 10^{-6}$ cP). Amplitude ratios and travel time delays were computed from spectral amplitude and phase and compared with the experimental data. Spectral-amplitude ratios and travel time delays for the reservoir reflection are shown using solid lines in Figures 35a and 35b, respectively.

The travel time delay was calculated by subtracting the two phase angles (97th-96th) and dividing by frequency, at each frequency sampled. All featured characteristics of the reflections (amplitude ratios and travel time delay) are frequency dependent and indicate attenuative properties of thin porous layers. Layers with high attenuation rate and reverse velocity dispersion produce travel time delays increasing as frequency approaches zero.

The computed relative $1997/1996$ amplitude ratio and time delay of reflection coefficients from NIPSCO gas storage resembles experimental date (Figure 34). The reflection amplitude ratio 97/96 increases with a decay in frequency, it almost doubles at low frequencies ($10-15$ Hz). Relative time delay for the computed results and experimental data (Figure 34b) follow the same pattern in behavior. The numerical modeling results involving Kraulis wave phenomenon is in agreement with seismic monitoring data (Goloshubin et al., 2001) from the Royal Center Field, Indiana.

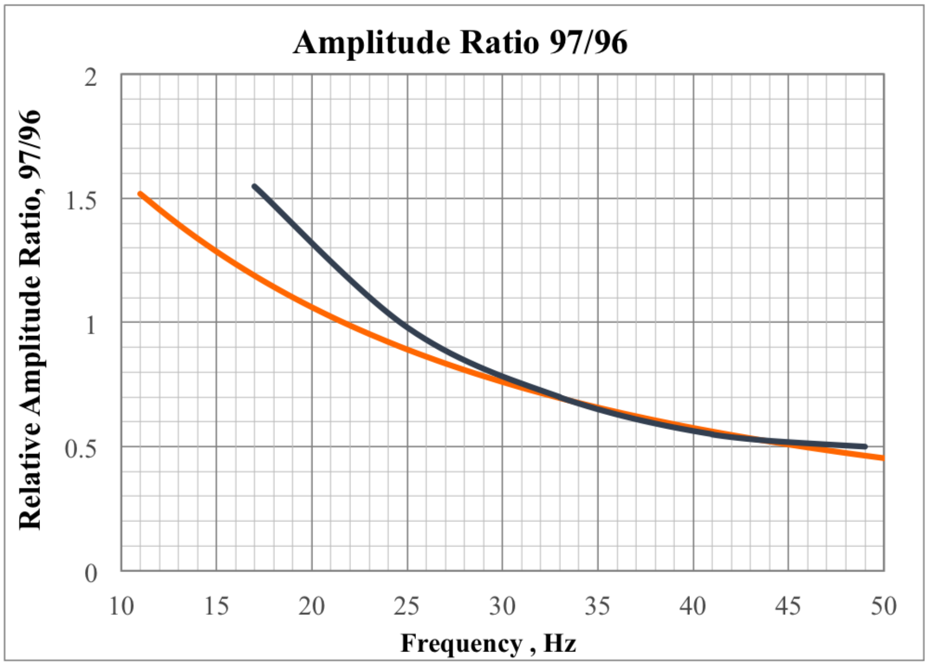

(a) Relative amplitude ratio of reflection coefficients 97/96. Experimental data - dark-blue curve; numerical prediction - orange curve.

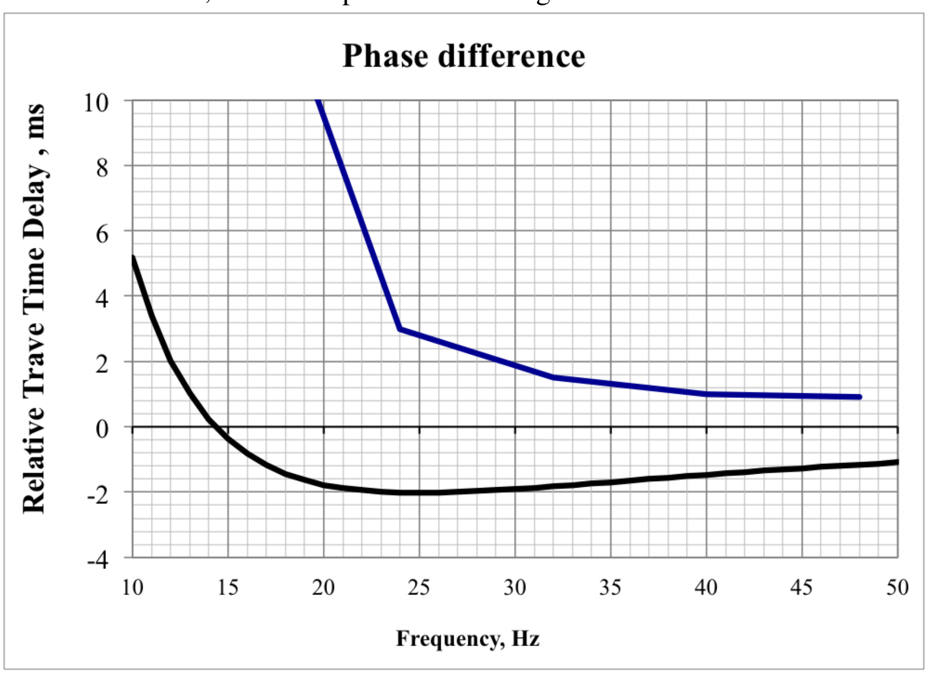

(b) Relative (1997/1996) travel time delay. Experimental data - blue curve; numerical prediction - black curve

Figure 35. Relative 1997/1996 amplitude ratio and phase difference of reflection coefficients from NIPSCO gas storage in Trenton formation reservoir.

6.2 Seismic image of fractured shale

The East-Surgut Basin is a part of the Western Siberian plain of Russia where the Jurassic sediments are the most prospective targets for oil and gas production (Figure 36). The Jurassic formations are characterized by high heterogeneity. The oil and gas potential of Jurassic reservoirs is still high; the estimation is about 45% of the total oil and gas reserves of Western Siberia (Ulmishek, 2003). The prediction of the hydrocarbon reservoir locations based on available data is the key aspect of the basin exploration.

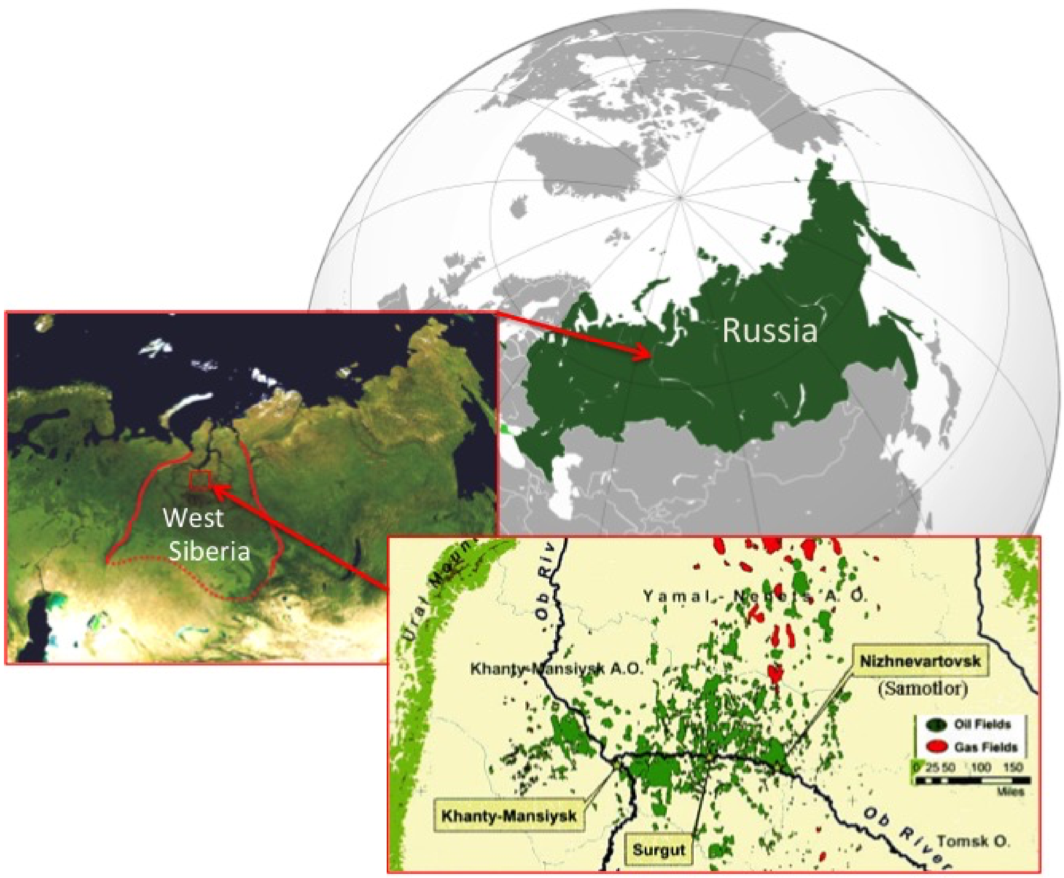

Figure 36. The geo-position of the East-Surgut basin. *Modified from Wikipedia.com, Maps.Google.com and Grace - Russian Oil Supply.*

The example is based on the data from Ai Pim Western Siberia oil field. Excessive resistivity, high gamma-ray, low-density well log data (Figure 37) indicate the presence of the fractured source rock in the Upper Jurassic (Goloshubin et al., 2006).

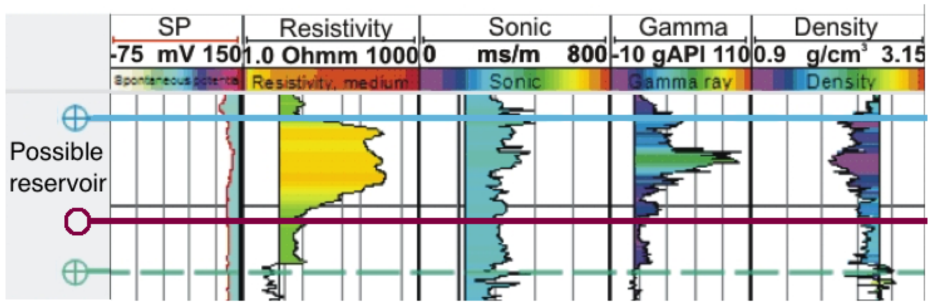

Figure 37. The well log from one of the wells that penetrates the target layer. Excessive resistivity, high gamma ray, low-density well log data indicate the presence of source rock.

Figure 38 depicts the standardized processing of the seismic time cross-section. The high-resolution seismic section identifies local small-amplitude structures and stratigraphic non-conformities; however, the test results from the wells show no correlation between seismic predictions and the actual fluid content in wells. Along the chosen seismic horizon neither the amplitude nor the shape of the signal changes; nevertheless not all wells are producing oil. This could be due to zones of fractured and non-fractured structure within the same formation. Goloshubin et al. (2006) reprocessed the seismic data with a wavelet transform of 12 Hz (Figure 39). The low-frequency processed image has a more precise correlation between fractured "sweet spots" and fluid-producing wells. In general, such anomalies can be associated with a tuning effects related to the variation of the formation thickness; however, the shale in the Upper Jurassic is the result of deep oceanic depositional environment, extended over large area and maintain a uniform thickness.

Below, the hypothesis is justified that the separation of the fractured and non-fractured zones can be done frequency-dependent analysis. Even in the anisotropic conditions, Krauklis wave may give a contribution to the P-wave velocity dispersion and attenuation, if only one direction of the P-wave prorogation is considered.

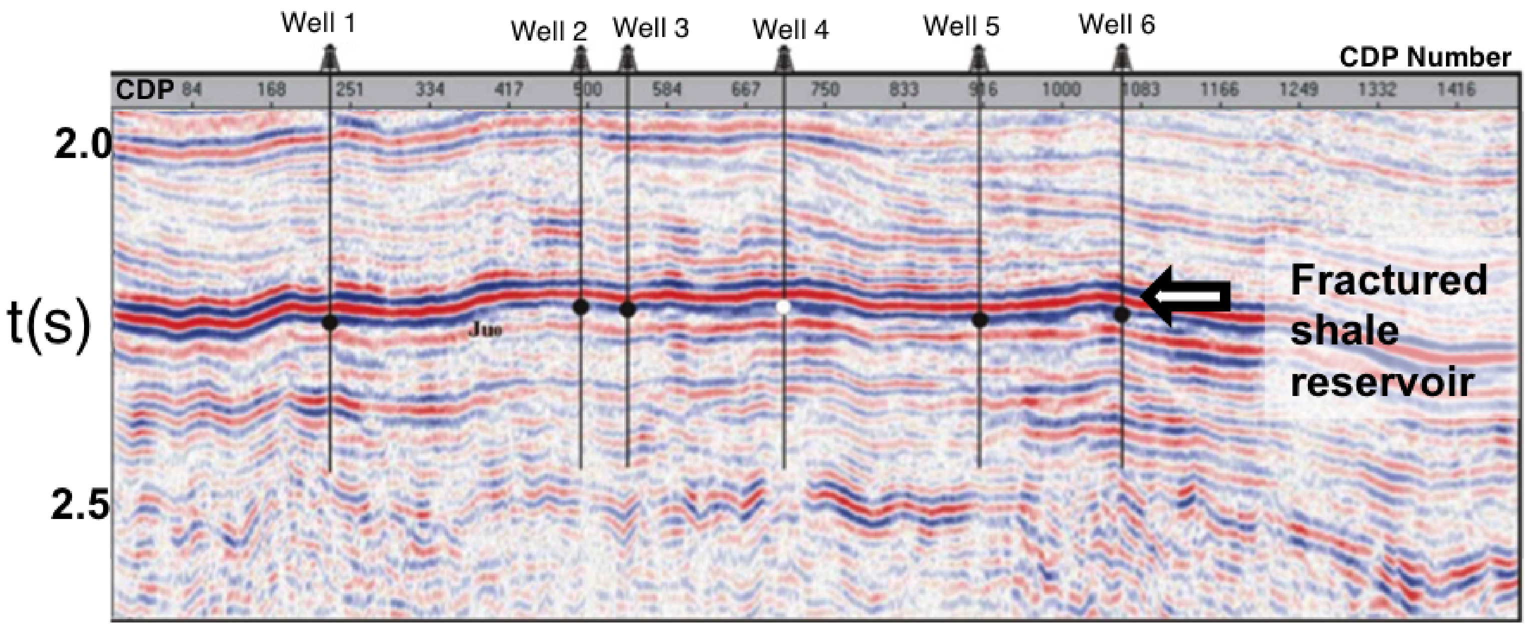

Figure 38. A seismic line from Ai Pim Western Siberia oil field was used to image oil-saturated reservoir (Goloshubin et al., 2006). Black dots show oil-producing wells; white dots are dry wells. The reservoir is represented by 15 – 20 m thick fractured shale. There is no evident correlation between well content and high frequency standard seismic imaging.

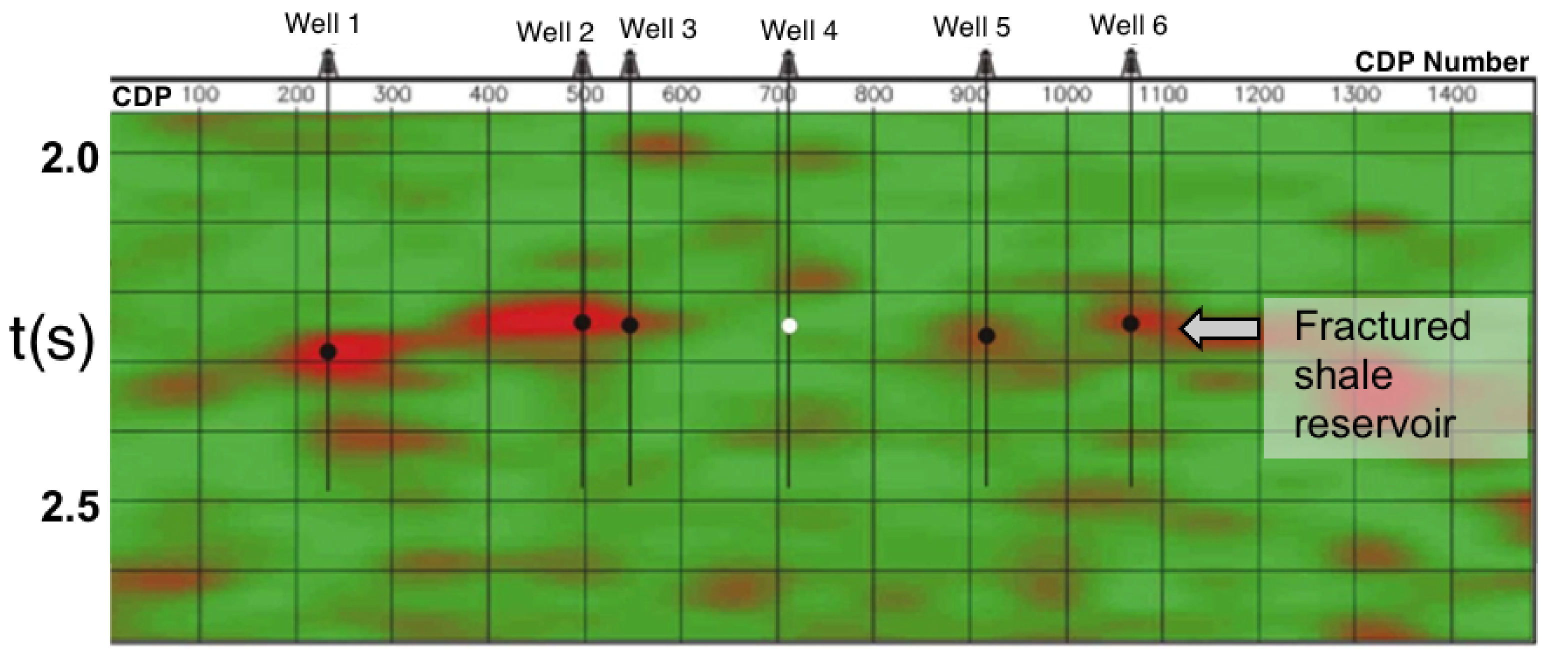

Figure 39. Image of the same reservoir at low-frequency (< 15 Hz) (Goloshubin et al., 2006) gives a good correlation for the reservoir and oil producing wells.

Based on the well log data (Figure 37) and reservoir size, the reflectivity of the horizon was calculated using above-described theory (See Section 5.2). The AI of the formation is relatively low compared to formations above and below (Figure 40). The upper formation is characterized by P-wave velocity $V_P = 3600$ m/s, S-wave velocity $V_S = 1800$ m/s, and density $\rho = 2440$ kg/m^3. The target layer has $V_P = 2580$ m/s, $V_S = 1260$ m/s, and $\rho = 2300$ kg/m^3. The formation below is consistent with $V_P = 3800$ m/s, S-wave velocity $V_S = 1900$ m/s, density $\rho = 2480$ kg/m^3, and quality factor $Q_m = 80$ (Goloshubin et al., 2014). In Figure 41, normal incidence of reflection coefficients from fractured compared against a non-fractured 20 m layer with the same properties.

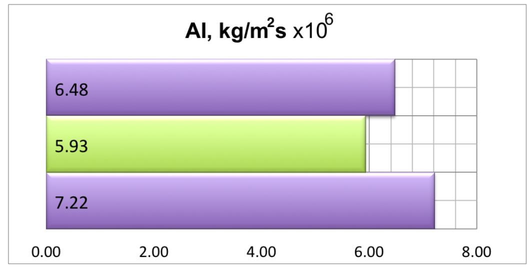

Figure 40. Acoustic impedance

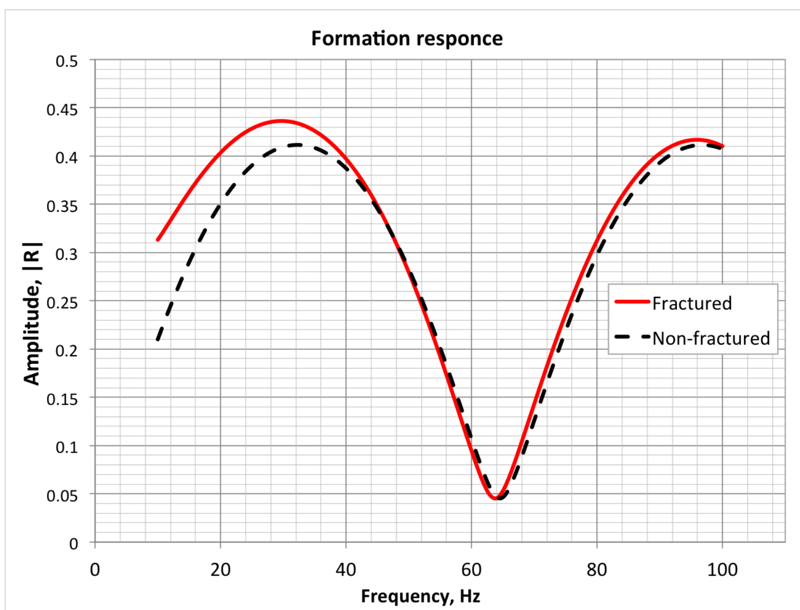

Figure 41. Amplitudes of the normal incident reflection coefficients vs. frequency for the target formation

The modeling of reflection coefficient was made in Fortran 95 (Section 9.1) using above-mentioned parameters. The fluid within fractures was assumed to be oil with $\rho_{fl} =$ 800 kg/m^3 with viscosity $\eta_{fl} =$ 5cP. Figure 41 illustrates: the reflection coefficients are different at the frequencies below 40 Hz, and about the same in the range 40 – 100 Hz. The relative difference of amplitudes of normal incidence reflection coefficient between fractured and non-fractured cases was examined at frequencies 10 – 50 Hz. A the low-frequencies (Figure 42) the ratio achieves about 40-50%, for the fractured media the fracture density constant was taken $N_0 = 10^4$. Hence, the application of 10 – 15 Hz wavelet transform would produce maps with distinguishable fractured and non-fractured zones, similar to what Goloshubin et al. (2006) have on their section. Thus, the proposed theoretical approach can be helpful in interpretation of a seismic data for the prognoses of fractured reservoir zones. It is possible even in case of an anisotropic shale, analyzing one (normal) direction of the P-wave propagation.

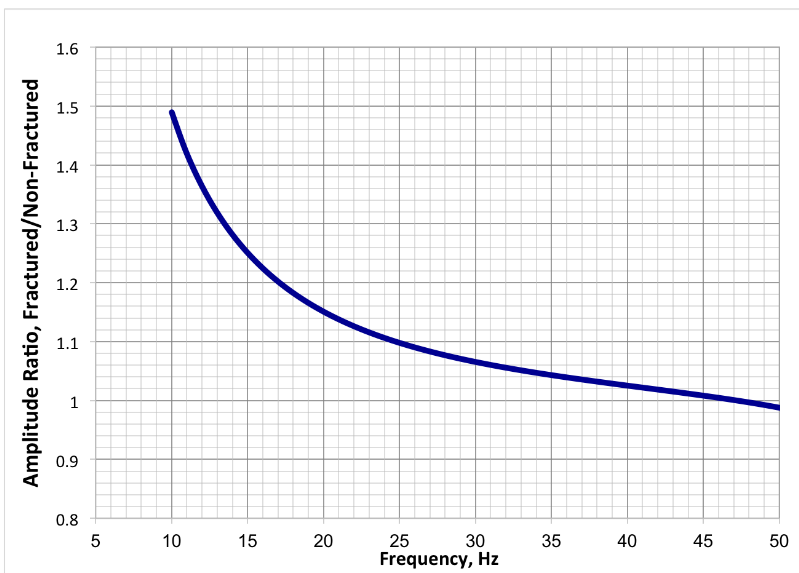

Figure 42. Ratio of amplitudes of the normal incident reflection coefficients of fractured to amplitudes of the normal incident reflection coefficients of non-fractured formation vs. frequency.

6.3 Physical modeling

The physical modeling was conducted at the Allied Geophysics Laboratory (AGL) at the University of Houston with the synthetic sample created on the 3-D printer. By the nature of the 3-D printing mechanism, samples are porous, thus they can be used for experiments to compare saturated versus non-saturated cubes. In addition, there is a possibility to create connected fracture-like structures while printing a sample (Figure 43a). The printing material was a thermoplastic type, called ABSplus[1] it is mechanically strong and stable over time. The material is approximately isotropic with an average P-wave velocity of approximately 2159 ± 6 m/s, S-wave velocity of 888 ± 3 m/s, and density 1040 kg/m^3 (Huang et al., 2016).

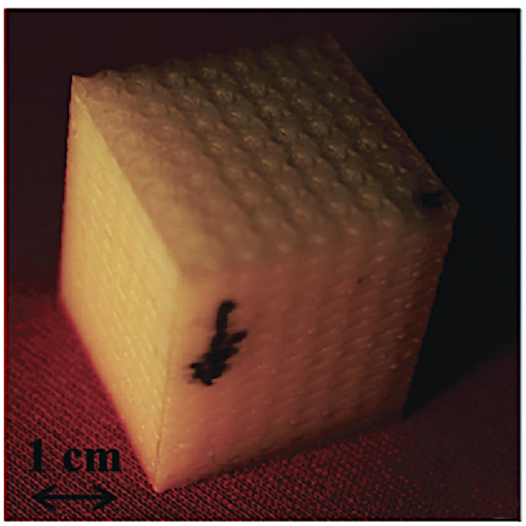

(a) Synthetic porous cube with fractures printed with 3D printer.

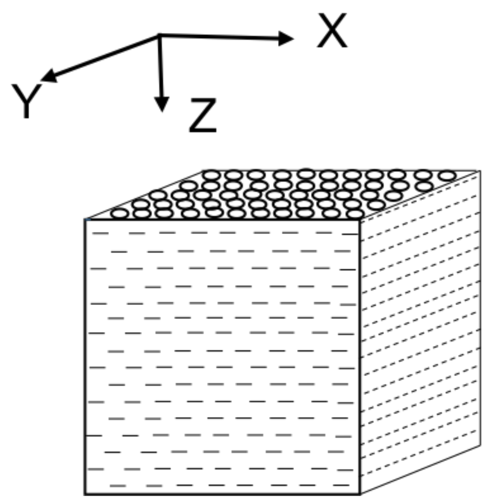

(b) Orientation of fractures in a cube in a space.

Figure 43. 3D printed cube (a side size 25 mm) with fracture inclusions parallel to layers. *Picture courtesy of N. Dyaur and AGL (UH).*

Under a constant weight (1170.9 g), the ultrasonic transducers with a central frequency 500 kHz (Figure 44) have been used to record the transmitting signal through non-fractured

[1] http://www.stratasys.com/materials/fdm/absplus

and fractured samples. To prevent leakage of the fluids the clear tape with thickness 0.089 mm was used. The same tape was left on the dry cube for ensuring the same coupling in all cases. Both cubes have same geometrical shape and size of 0.025 m.

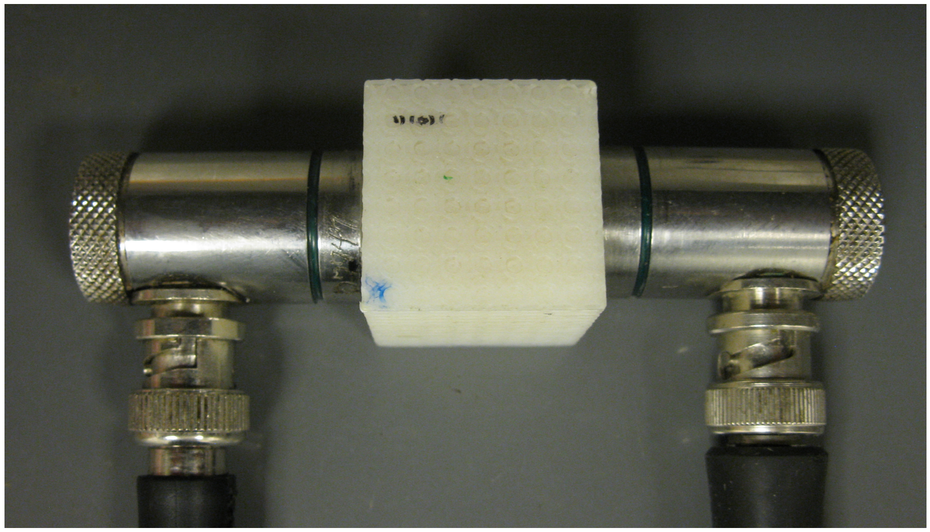

Figure 44. The cube with 500 kHz Transducers. *Pictures courtesy of N. Dyaur.*

The porous cube density was measured and resulted in 980 kg/m^3, with the porosity about 6%. The velocities in the direction of layering were $V_P = 1914$ m/s and $V_S = 879$ m/s for the dry sample, and $V_P = 2145$ m/s, $V_S = 879$ m/s for the saturated cube. The fractured sample has 27 layers with "penny-shape" fractures parallel to the printing layering. All fractures have the same size: $l = 0.00175$ m and $h = 5 \cdot 10^{-4}$ m. The porosity of the fractured cube was 24%, meaning that fractures contribute 18% to the porous model (Huang et al., 2016). As the model is anisotropic, here was considered, only velocities in the direction of fractures are observed: for dry cube $V_P = 1706$ m/s, $V_S = 812$ m/s, and for the saturated cube $V_P = 2052$ m/s, $V_S = 742$ m/s.

Below the following hypothesis is tested: is the calculation of the velocity of the water-saturated fractured cube can be made based on the parameters of the dry non-fractured sample? In this test, the Gassmann fluid substitution theory Gassmann (1951). was used for prognoses of non-fractured matrix parameters. The velocity of the fractured water-saturated sample was estimated by the proposed theoretical approach.

The estimations were made according to the Smith et al. (2003) fluid substitution tutorial, using equation:

$$K_{sat} = K^* + \frac{\left(1 - \frac{K^*}{K_0}\right)^2}{\frac{\phi}{K_{fl}} + \frac{1-\phi}{K_0} - \frac{K^*}{K_0^2}}, \tag{38}$$

where K_{sat} = the saturated bulk modulus, K_0 = bulk modulus of the material (in case of cubes, original material used in 3D-printer), K_{fl} = bulk modulus of the fluid (water), K^* = dry modulus of the porous frame, ϕ is porosity.

Using, in the equation (38), the dry P- and S- wave velocities of the dry porous cube and porosity $\phi = 6\%$, the saturated P-wave velocity of the porous cube is $V_{P_{sat}}^{(p)} = 2123$ m/s, which is less than measured (recall $V_P = 2145$ m/s).

Further, consider fractures have been added to the saturated porous cube. Hence, the above-mentioned P- and S-wave velocities were used as the matrix parameters for the averaging (29), and 600 identical fractures. Figure 45 illustrates the result of the averaging of the P-wave velocity for the $400-600$ kHz. The effective velocity at the transducer frequency is $V_{P_{sat}}^{(f)} = 1975$ m/s, which is 4% less then measured $V_P = 2052$ m/s. This results suggested a possible application of the isotropic averaging technique in combination with other theories for the rough predictions of velocities in fractured saturated samples, based on parameters of the dry porous background; however, the general concept requires further development for the anisotropic materials.

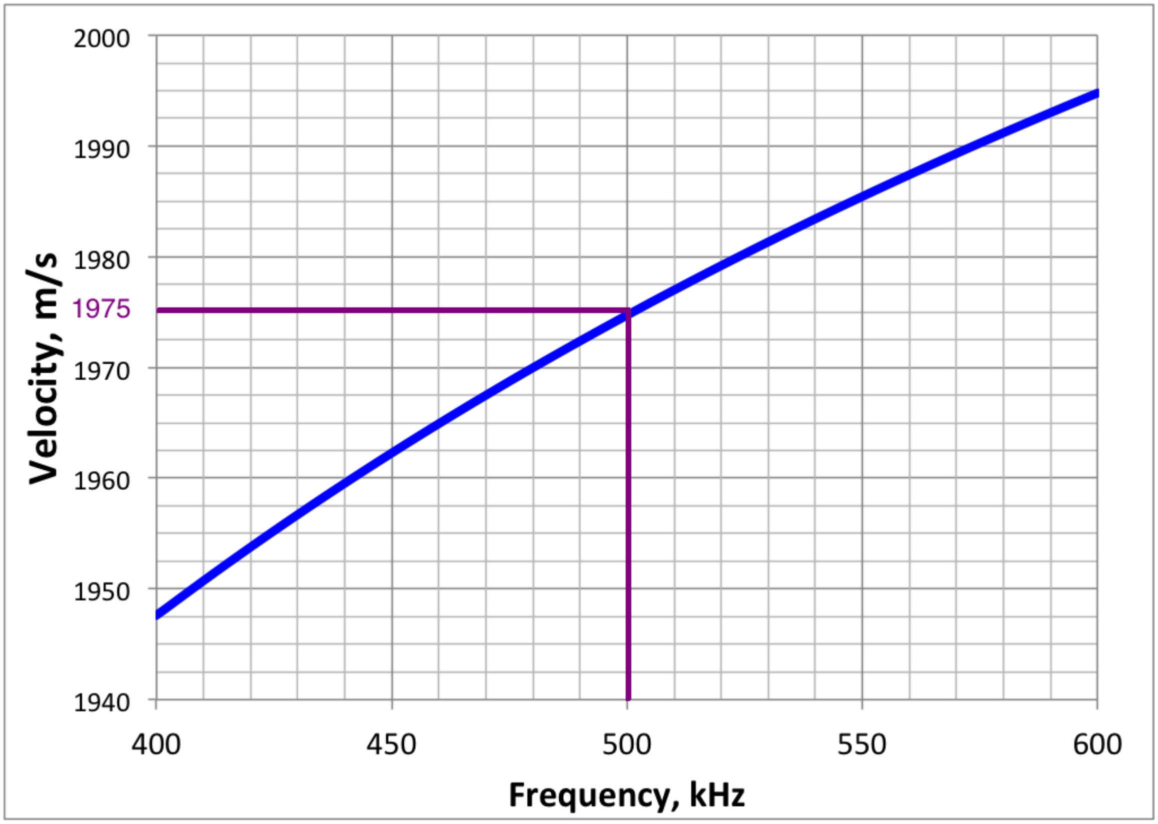

Figure 45. The estimation of the velocity of fractured water-saturated cube according to the proposed averaging technique. The predicted effective velocity is $V_{P_{sat}}^{(f)} = 1975$ m/s.

7 Discussion and Conclusions

The objectives of this research were to consider a randomly fractured fluid saturated media. The averaging of the effective elastic properties of fluid-saturated isotropic-fractured rock was proposed with consideration of extremely slow and dispersive guided wave propagation within individual fractures at the seismic range of frequencies ($10-100$ Hz). The Krauklis wave (K-wave) was presented as an low frequency asymptotic solution of the guided wave.

The random fracture distribution was described by the four relationships between the number of fractures and their length, these relations have a deep connection to the natural observations and field data. For any laws of the random fracture distribution, the presence of K-waves tends to increase P-wave velocity dispersion and attenuation with a decrease of frequency.

Due to K-wave propagation within fractures, the effective velocity and attenuation are dispersive. Reverse velocity dispersion and attenuation become two times greater with an increase of one order in the fracture density. Effective velocity and attenuation are sensitive to the fracture thickness, the thicknesses below 10^{-3} m have a significant influence on the parameters at the low frequency, but their effect is small at the high frequencies. The increasing viscosity of the fluid inside fractures elevates the attenuation; though, the velocity varies lesser with viscosity. The growth of the attenuation in the background matrix causes the increase in the effective attenuation.

Applications of the averaging were considered in the framework of the reflectivity of the media. The comparison of the reflection coefficients from the boundary with fractured and non-fractured half-spaces was made. Compared to the frequency independent reflection coefficient amplitude between two homogeneous half-spaces, the amplitude of reflection coefficient between homogeneous and fractured varied with the frequency. The drastic difference between them was present at the low frequencies.

For two assumed widths of the layer, the results exhibited the remarkable difference of the P-wave reflection coefficient from the fractured layer in comparison with the homogeneous layer in all cases of the acoustic impedance distribution. The biggest difference in behavior of the reflection coefficients versus incident angle was observed at low frequencies. The thickness related tuning effects had an impact on the seismic signal; they differ for the fractured and homogeneous layers for all acoustic impedance cases.

As the case studies tree field examples consistent with the assumptions of the averaging technique were considered. The numerical modeling results involving Krauklis wave theory were in agreement with seismic monitoring data from the Royal Center Field, Indiana. The results of the modeling might prove theoretical justification for low-frequency seismic anomalies, detected in fractured zones within source rock in the East-Surgut Basin, Western Siberia. At last, was investigated the possibility of a P-wave velocity prediction in the fluid-saturated fractured sample based on the velocity of dry non-fractured porous material. The combination of the Gassmann fluid substitution and proposed methodology for velocity calculations were applied. The results were weighted against the laboratory measurements on the fractured 3-D printed samples. The predicted velocity appeared to be 4% less than measured.

The approach and results of its calculations allow an interpretation of reverse velocity dispersion, high attenuation, and special behavior of reflection coefficients vs. frequency and angle of incidence as the indicators of fractures; however, this technique has a broad spectrum of ways of the further development.

Based on the main assumptions of this research, the following list consists of (but not limited to) major directions of expanding the proposed theoretical approach.

A. In this work only random fractures were considered and oriented fractures were avoided. Expanding it to the anisotropic models can do one of the major developments in this technique. Hence, bringing forward the estimation of the frequency-dependent anisotropic velocity and attenuation.

B. The other contribution to the semi-empirical averaging methodology would be the detailed development and implementation of the interactions between fracture and porous background matrix.

C. There is a wide possibility for consideration of interactions between single fractures for this model (e.g., intersection of fractures, connectivity).

8 Appendix I: Volumes and Densities

8.1 Wave volumes

8.1.1 P-wave volume

The region around a ray that mostly influences the propagation of a band-limited wave is called the **first Fresnel zone** (Spetzler and Snieder, 2004). In reality, a wave does not strictly propagate along a line, as it assumed in the ray theory. Generally, a wave is a collective phenomenon in which the particle motion is organized over a finite region of a space (Scales and Snieder, 1999). For waves with a finite frequency band, discontinuities in the wavefield tend to be smoothed out as the waves propagate. Hence, the wavefield is continuous over a limited area of propagation. The size of the region over which the wavefield varies is given by the wavelength, which decreases for increasing frequency (Spetzler and Snieder, 2004).

Consider a source at the location $\mathbf{r_s}$ on Figure 46 that excites waves. According to the representation theorem, the wavefield recorded at the receiver location $\mathbf{r_r}$ can be represented as an integral over a subsurface S that is located between the source and receiver. Using this geometry the wavefield at the receiver position can be written as

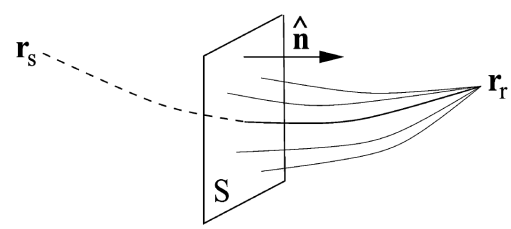

Figure 46. Wavefield at the reciever location $\mathbf{r_r}$. *Shapshot from (Spetzler and Snieder, 2004).*

$$P(\mathbf{r_r}) = \int_S \frac{1}{\rho_{(\mathbf{r})}} \left(P(\mathbf{r})\nabla G(\mathbf{r},\mathbf{r_r}) - G(\mathbf{r},\mathbf{r_r})\nabla P(\mathbf{r})\right) \cdot ds, \tag{39}$$

where $P(\mathbf{r_r})$ is the acoustic pressure at the receiver position $\mathbf{r_r}$, ρ is the mass density, and $G(\mathbf{r},\mathbf{r_r})$ is the Green's function. This expression holds for acoustic waves. The medium or which the Greens function $G(\mathbf{r}, \mathbf{r_r})$ is defined can be either homogeneous or inhomogeneous. The wavefield on the surface S in the integral (39) is the total wavefield. When the backscattering is weak, the wavefield in the integral can be substituted by the incident waves that travel directly from the source to the surface S. This simplification is called the Kirchhoff approximation. In the Kirchhoff approximation, the integral (39) can be interpreted as a superposition of waves that have been scattered from different points on the surface S.

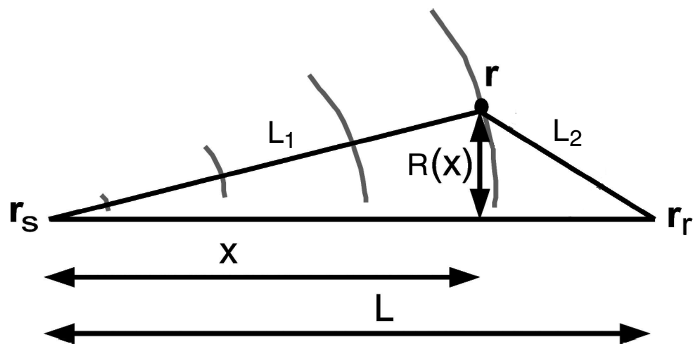

Figure 47. Definition of the geometric variables in a homogeneous velocity model. Wavefronts of the wavefield emitted from the source and the wavefronts of the diffracted wavefield due to the diffractor at position **r** are illustrated with the solid and dashed gray lines, respectively

For a homogeneous model, the geometry of the diffraction process is shown in Figure 47. The incident wave propagate from the source at $\mathbf{r_s}$ to the point $\mathbf{r}$ and initiate the a diffracted wavefield that radiated to the receiver $\mathbf{r_r}$. The point $\mathbf{r}$ belongs to the surface S of the expression (39) at the distance x from the source, along the geometric ray. The distance from $\mathbf{r}$ to the geometric ray is $R(x)$, distance from the source to a receiver is L. Then the travel path D of the ray from the $\mathbf{r_r}$ to $\mathbf{r_s}$ through $\mathbf{r}$ is:

$$D = L_1 + L_2 - L \leq \frac{\lambda}{2}, \tag{40}$$

and $L - x = \frac{\lambda}{2}$, hence, using Pythagorean theorem,

$$D = \sqrt{x^2 + R^2(x)} + \sqrt{(L-x)^2 + R^2(x)} - L. \tag{41}$$

For the $x \gg R(x)$, $D = L + \frac{\lambda}{2}$:

$$L + \frac{\lambda}{2} = \sqrt{x^2 + R^2(x)} + \left.\sqrt{\left(\frac{\lambda}{2}\right)^2 + R^2(x)}\right|_{x \gg R(x)} = x + \sqrt{\left(\frac{\lambda}{2}\right)^2 + R^2(x)}, \tag{42}$$

$$\lambda = \sqrt{\left(\frac{\lambda}{2}\right)^2 + R^2(x)}, \Rightarrow \qquad R^2(x) = \lambda^2 - \frac{\lambda^2}{4} \tag{43}$$

$$R(x) = \frac{\sqrt{3}}{2}\lambda. \tag{44}$$

Thus the Fresnel zone volume, which defines P-wave volume, is expressed as:

$$Vol = \frac{4\pi}{3} R^2(x) \cdot \frac{\lambda}{2} = \frac{\pi}{2}\lambda^3 \tag{45}$$

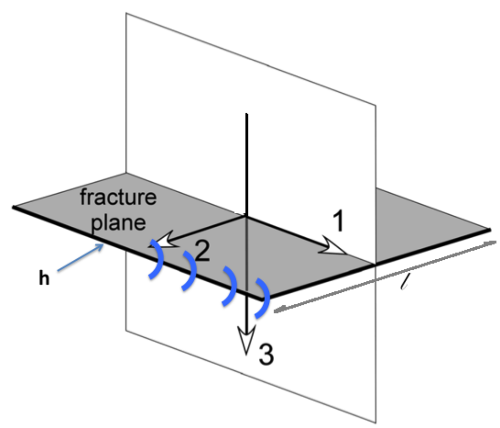

Figure 48. Planar fracture scheme

8.1.2 Single fracture volume

The volume of the finite plain fracture of the thickness h and the length l is defined as:

$$v_f = h \cdot l^2 \tag{46}$$

And the volume of the ellipsoid fracture with the radius $l/2$ and the thickness h is defined as:

$$v_f = \frac{\pi}{3} l^2 h \tag{47}$$

8.1.3 Wave volume of a single fracture

Consider the guided wave phenomena in a fracture (Figure 49). The wave has strong component along the fracture, and it exponentially decays **e** times, passing the distance equal to $\frac{\lambda_K}{2\pi}$. The thickness of the fracture including decay distance is:

$$h_K = \frac{\lambda_K}{2\pi} + \frac{\lambda_K}{2\pi} + h = \frac{\lambda_K}{\pi} + h \tag{48}$$

where the λ_K is a guided wave wavelength, $\lambda_K < L_{min} < L_{max} < \lambda_P/2$ and $\lambda_K = \frac{2\pi V_K(\omega)}{\omega} \gg h$, thus:

$$h_k(\omega) = \frac{2\pi V_K(\omega)}{\pi\omega} + h \cong \frac{2V_K(\omega)}{2\pi f}. \tag{49}$$

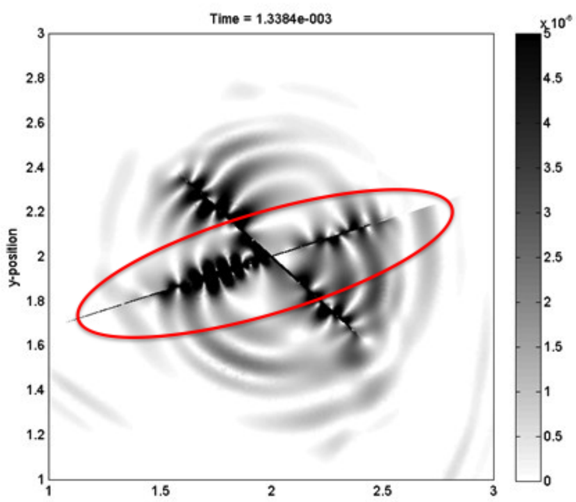

Figure 49. Ellipsoid fracture volume scheme. *Modefied after (Frehner and Schmalholz, 2010).*

Hence, if the fracture is represented as a plain, the wave volume of the guided wave is:

$$v_{fr}(l,\omega) = 2l^2 \frac{V_K(\omega)}{\omega} = \frac{1}{\pi} l^2 \lambda_K \tag{50}$$

In case of an ellipsoid-shaped wave volume:

$$v_{fr}(l,\omega) = \frac{4\pi}{3} \frac{l^2}{4} \frac{V_K(\omega)}{\omega} = \frac{1}{6} l^2 \lambda_K. \tag{51}$$

The limitations on the fracture length is governed by the minimum frequency of a band f_{min}, P-wave and guided wave velocities:

$$L_{min} = \frac{V_K(\omega)}{f_{min}}, \tag{52}$$

$$L_{max} = \frac{V_P}{2f_{min}}. \tag{53}$$

8.1.4 Total volume of the fluid

The total volume of the fluid in the fracture network can be estimated as:

$$Vol_f = \frac{1}{L_{max} - L_{min}} \int\limits_{L_{min}}^{L_{max}} \nu_f(l) N_i(l) dl, \tag{54}$$

where $N_i(l)$ number of fractures or any law defining fracture distribution.

8.1.5 Cumulative volume of all fractures

Consider a fractured medium. Each fracture has its wave volume (51), hence, the averaged wave volume of all fractures with guided wave phenomena is:

$$Vol_{fr}(\omega) = \frac{1}{L_{max} - L_{min}} \int\limits_{L_{min}}^{L_{max}} \nu_{fr}(l,\omega) N_i(l) dl, \tag{55}$$

where $N_i(l)$ number of fractures or any law defining fracture distribution.

8.1.6 Volume of the background matrix

The volume of a background matrix is defined as deference of P-wave volume and cumulative wave volume of fractures.

$$Vol_m = Vol - Vol_{fr} \tag{56}$$

8.2 Densities

The density of the background matrix ρ_m is initially known, as well as the density of fluid ρ_{fl} in fractures. There are other densities that should be defined related to volumes they belong.

The density in the volume (51) is defined as average between the density of the matrix surrounding fracture and the density of liquid inside the fracture:

$$\rho_{fr}(\omega) = \frac{Vol_f \rho_{fl} + v_{fr}(\omega)\rho_m}{Vol_f + v_{fr}(\omega)} = \frac{l^2 h \rho_{fl} + \frac{\lambda_K}{\pi} l^2 \rho_m}{l^2 \left(h + \frac{\lambda_K}{\pi}\right)} = \frac{h\rho_{fl} + \frac{\lambda_K}{\pi}\rho_m}{\left(h + \frac{\lambda_K}{\pi}\right)} = \frac{h\rho_{fl} + \frac{2\pi V_K(\omega)}{\pi\omega}\rho_m}{\left(h + \frac{2V_K(\omega)}{\omega}\right)} \tag{57}$$

$$\rho_{fr}(\omega) = \frac{h\rho_{fl} + \frac{2V_K(\omega)}{\omega}\rho_m}{h + \frac{2V_K(\omega)}{\omega}} \tag{58}$$

The average density of the fractured media as whole, can be calculated by:

$$\overline{\rho} = \frac{Vol_f \rho_{fl} + Vol_m \rho_m}{Vol}. \tag{59}$$

9 Appendix II: Codes

9.1 Fortran 95 codes

Krauklis wave velocity calculation code

```
!==============================
! file with solid matrix and fluid parameters
! input.txt with header in order
! Vp Vs rho rof nu_f G h Qm fmin fmax dm
! Vp, Vs - P- and S- wave velocities
! rho and rof - density of matrix and density of fluid, respectively
! G = shear modulus
! h - opening of fracture
! Qm - q-factor of matrix
! fmin and fmax = minimum and maximum frequency
! dm = frequency step
! written by: Anna Krylova, 2017
!==============================

program velocity_krauklis

real Vs,Vp,G,f,h,rof,rho,Vk,nu_f ,S,QK, Qm
real, parameter :: Pi=3.1415927
integer m0,m1,dm
complex VKK, beta
integer, parameter :: in_unit=10, out_unit=20
real :: dmmin = 1.0e-4


open (unit=10, file="input.txt", status="old", form="formatted", action=
    "read")
```

```fortran
read (unit=10, FMT=*)
read (unit=10, FMT=*) Vp,Vs,rho, rof,nu_f,G, h,Qm, m0,m1,dm
close(10)
open (unit=20, file="results_vk.txt")

If( dm<dmmin) stop 'choosing step error'
  f = m0

 do while(f<=m1)
      Vk = (2*Pi*f*h*G*(1-(vs/vp)**2)/rof)**(1.0/3.0)
      S=h*sqrt((2*Pi*f*rof)/nu_f)
      beta= - CMPLX(0.0,1.0)*S**2/12.
      VKK= Vk*(beta/(1+sqrt(beta/3)+beta))**(1.0/3.0)
      QK= abs(  real(VKK**2)/aimag(VKK**2))
      print *,'  Vp=', Vp, '  Vs=', Vs,'  fminr=', m0,'  fmax=', m1,'  f=', f, S
      write (20,FMT=*)Vp, Vs, m0, m1, f , real(VKK), aimag(VKK)
      f=f+dm
 end do
 close(20)

 end program velocity_krauklis
```

P-wave volume and volume of fractures

```fortran
program Vol
implicit none
real  fr, Vop, vk
double precision a, b, integral, lmax, lmin
integer n
```

```
double precision vkk
external f
real, dimension (1:91, 1:7) :: Array
integer :: ln, col


open (unit=20, file="results_vk.txt", status="old", form="formatted", action="read")
open (unit=30, file="volumes.txt")

 do ln=1,91
 read (20, FMT=*)(Array (ln, col), col=1,7)
 end do

do ln=1,91
  write (30,FMT=* ) (Array (ln, col), col=1,7)
end do
close(30)
call printMatrix(Array,91,7)

open (unit=30, file="volumes.txt")
open (unit=40, file="results_volumes.txt")
do ln=1,91
   read (30, FMT=*)(Array (ln, col), col=1,7)
   lmax= Array(ln,1)*sqrt(Array(ln,4)**2-Array(ln,3)**2)/(Array(ln,4)*Array(ln,3))
   lmin=Array(ln,6)/Array(ln,4)

   a=lmin
   b=lmax
   n=500
```

```
    fr=Array(ln,5)
    Vop=(  (Array(ln,1)/Array(ln,3))**(3.)-(Array(ln,1)/Array(ln,4))**(3.)  )*0.5
    vkk=Array(ln,6) !+CMPLX(0.0,1.0)*Array(ln,8)
    call ave_trap (f,a,b,integral,n,vkk,fr)
    write (40, FMT=*)  Array(ln,5), integral, Vop, Array(ln,6), Array(ln,7)
    print *, a, b ,  Array(ln,5), integral, Vop, Array(ln,6), Array(ln,7)
  end do

 close(40)
 close(20)
close(30)

end program Vol


!------------------------------------------------------------
!Matrix Print
!------------------------------------------------------------
 subroutine printMatrix(array, n, m)
implicit none
real, intent(in) :: array(n,m)
integer, intent(in) :: n,m
integer :: i
do i = 1,n
print*, array(i,:)
end do
end subroutine printMatrix


```

```
Function f(l,vkk,fr)
!----------------------------------------------------
! Function for integration_
!single fracture volume * law of distribution
! frequency dependent
!----------------------------------------------------
implicit none
double precision  l
real N0, l0, fr

double precision, parameter:: pi = 3.1415926
double precision vkk,f

real, dimension (1:91, 1:7) :: Array2

integer :: ln, col
open (unit=10, file="results_vk.txt", status="old",form="formatted",
    action="read")

 do ln=1, 91
 read (10, FMT=*)(Array2 (ln, col), col=1,7)

N0=10**(4.)   !fracure density const
l0=1.0
f = N0*((l/l0)**(-2.5))*(l**2.)* vkk/(6.* fr)
 end do
 close(10)

return
end

```

```
Subroutine ave_simpson(f,a,b,integral,n,vk,vkk,fr)
!=============================================================
! Integration of f(x) on [a,b]
! Method: Simpson rule for n intervals
! written by: Alex Godunov (October 2009)
!modified by: Anna Krylova (March 2017)
!-------------------------------------------------------------
! IN:
! f    - Function to integrate (supplied by a user)
! a    - Lower limit of integration
! b    - Upper limit of integration
! n    - number of intervals
! OUT:
! integral - Result of integration
!=============================================================
implicit none
double precision  a, b, integral,s
double precision hh, l
real fr
integer nint
integer n, i
double precision f, vkk, vk
! if n is odd we add +1 to make it even
if((n/2)*2.ne.n) n=n+1

! loop over n (number of intervals)
s = 0.0
hh = (b-a)/dfloat(n)
do i=2, n-2, 2
  l = a+dfloat(i)*hh
```

```
   s = s + 2.0*f(l,vkk,fr) + 4.0*f(l+hh,vkk,fr)
end do
integral =(1./(b-a))* (s + f(a,vkk,fr) + f(b,vkk,fr) + 4.0*f(a+hh,vkk,fr
   ))*hh/6.0
return
end subroutine ave_simpson


Subroutine ave_trap(f,a,b,integral,n,vkk,fr)
!==========================================================
! Integration of f(x) on [a,b]
! Method: Trapezoid rule for n intervals
! written by: Alex Godunov (October 2009)
!modified by: Anna Krylova (March 2017)
!----------------------------------------------------------
! IN:
! f   - Function to integrate (supplied by a user)
! a   - Lower limit of integration
! b   - Upper limit of integration
! n   - number of intervals
! OUT:
! integral - Result of integration
!==========================================================
implicit none
double precision  a, b, integral,s
double precision hh, l
real fr
integer nint
integer n, i

double precision vkk,f
```

```

! if n is odd we add +1 to make it even
!if((n/2)*2.ne.n) n=n+1

! loop over n (number of intervals)
s = 0.5*(f(a,vkk,fr)+f(b,vkk,fr))
hh = (b-a)/dfloat(n)

do i=1,n-1
  l = a+dfloat(i)*hh
   s = s + f(l,vkk,fr)
end do
integral =(1./(b-a))*hh*s
return
end subroutine ave_trap
```

Averaging of elastic constants

```
program elastic_const
!================
! Needs results from previous code Vol
! written by: Anna Krylova, 2017
!================
implicit none
real fr,rho,rof,G,h, vs,vp,Q,Qm, QK,nu_f
complex vk
integer m0, m1, dm
integer, parameter :: in_unit=40, out_unit=50
real, dimension (1:91, 1:5) :: Ar1
complex p1,p2,veff,cc,cpp,cpk
```

```
integer :: ln, col


open (unit=40, file="results_volumes.txt", status="old",form="formatted"
    , action="read")
open (unit=43, file="eff_elastic_const.txt")
open (unit=44, file="effective_velocity.txt")
open (unit=42, file="input.txt",status="old",form="formatted", action="
    read")
read (42,fmt=*)
read (unit=42, FMT=*) Vp,Vs,rho, rof, nu_f,G, h,Qm, m0, m1, dm
close(42)


 do ln=1, 91
 read (40,*)(Ar1 (ln, col), col=1,5)
     cpp=(Vp**2.0*rho) - CMPLX(0.0,1.0)*(Vp**2.0*rho)/Qm
  vk=Ar1(ln,4)+CMPLX(0.0,1.0)*(Ar1(ln,5))
  QK=abs(Ar1(ln,4)**2./Ar1(ln,5)**2.)
  cpk= (vk**2)*rho

  fr=Ar1(ln,1)
  p1= (Ar1(ln,2)/Ar1(ln,3))*cpk**(-1.)
  p2=( (Ar1(ln,3)- Ar1(ln,2))/Ar1(ln,3)) * Cpp**(-1.0)
  cc=( (Ar1(ln,2)/Ar1(ln,3))*cpk**(-1.)+ ((Ar1(ln,3)- Ar1(ln,2))/Ar1(ln
    ,3))*Cpp**(-1.))**(-1.)

     Veff= sqrt(cc/rho)
     Q=abs(real(cc)/aimag(cc))
 write (43, FMT=*) fr, real(p1) ,aimag(p1),real(p2), aimag(p2)
 print *,fr,real(Veff), aimag(Veff),Qk,Q, 1/Q
```

```
 write (44, FMT=*) Ar1(ln,1),real(Veff), aimag(Veff), Q, 1/Q

end do
 !call printMatrix(Ar1,46,4)
 close (44)
 close(40)

close(43)
end elastic_const
```

Reflection from a boundary

```
!===================
! input file with upper layer properties
! input_hom_layer_above.txt
! Vp, Vs, rho = P- , S- waves velocities, density
! written by: Anna Krylova, 2017
!===================

program reflectionboundary
implicit none
double precision, parameter:: pi = 3.1415926
real vp,vs, G,h, rof,rho, fr, width, Qm, nu_f
real rho2, vs2,vp2,R,theta,theta2
complex q,X,Y,Z,T, W1,W2,W3,W4,D, d1,d2,d3,d4,d5 !for zoeppr. eq
complex q2,X2,Y2,Z2,T2, W12,W22,W32,W42,D02, d12,d22,d32,d42,d52, dt !
    for zoeppr. eq
integer m0, m1, dm
complex R0,VF, R11, R33
integer, parameter :: in_unit=44, out_unit=50
```

```
real, dimension (1:91, 1:5) :: Ar2
integer :: ln, col

 open (unit=45, file="effective_velocity.txt", status="old", form="
    formatted", action="read")
 open (unit=46, file="input.txt",status="old",form="formatted", action="
    read")
 read (46,fmt=*)
 read (unit=46, FMT=*) Vp,Vs,rho, rof,nu_f,G,h,Qm,m0,m1,dm
 close(46)
 open (unit=47, file="input_hom_layer_above.txt",status="old",form="
    formatted", action="read")
 read (47,fmt=*)
 read (unit=47, FMT=*) Vp2, Vs2,rho2

 print*, "Enter width of the layer" ! width of a layer from keypad
 read (*,*) width
 close(47)

 open (unit=50, file="bound_ang_homo.txt")

do ln=1, 91
 read (45,*)(Ar2 (ln, col), col=1,5)
  fr=Ar2(ln,1)
  VF= Ar2(ln,2)+CMPLX(0.0,1.0)*Ar2(ln,3)   ! = Vp ! for homogeneous

   theta=0 ! initially some angle
   do  theta=0, PI/3, Pi/24    !range of angles w/step PI/24
  ! Zoeppritz equations
   T=sin(theta)/Vp2
   Q=2.*(rho*(VF/2.)**2.-rho2*Vs2**(2.))
```

```
    X=rho-Q*T**2.
    Y=rho2+Q*T**2.
    Z=rho-rho2-Q*T**2.
    W1=sqrt(1-Vp2**2.*T**2.)
    W2=sqrt(1-Vs2**2.*T**2.)
    W3=sqrt(1-VF**2.*T**2.)
    W4=sqrt(1-(VF/2.)**2.*T**2.)
    d1=Vp2*Vs2*VF*(VF/2.)*T**2.*Z**2.
    d2=VF*(VF/2.)*W1*W2*X**2.
    d3=Vp2*Vs2*W3*W4*Y**2.
    d4=rho*rho2*( Vs2*VF*W1*W4 + Vp2*(VF/2.)*W2*W3 )
    d5=Q**2.*T**2.*W1*W2*W3*W4
    D=d1+d2+d3+d4+d5
    R11 = -1+2.*W1*(D**(-1.))*(VF*(VF/2.)*W2*X**2.+ Vs2*VF*rho2*rho*W4 +Q
     **2*T**2*W2*W3*W4)
    R33 = 2*Vp2*rho2*T*(D**(-1.))*(VF/2 * W2*X + Vs2* W4 *Y)

      print *, fr, theta, abs(R11), abs(R33)
      write(50, FMT=*) fr, theta, abs(R11), abs(R33)
  end do
end do

 close(45)
 close(50)

end reflectionboundary
```

Reflection from a layer

```
program reflection_layer
```

```
!=================
! Input for upper and lower half-space
!Input_med_above.txt   -upper
!Input_med_below.txt   -lower
! P-, S- wave velocity , density
! written by: Anna Krylova , 2017
!=================
implicit none
double precision , parameter:: pi = 3.1415926
real vp,vs, G,h, rof,rho, fr, width, Qm, nu_f
real rho2, vs2,vp2,R, Vp22, Vs22,rho22,theta2,theta, phiR
complex q,X,Y,Z,T, W1,W2,W3,W4,D, d1,d2,d3,d4,d5 !for zoeppr. eq
complex q2,X2,Y2,Z2,T2, W12,W22,W32,W42,D02, d12,d22,d32,d42,d52, dt  !
    for zoeppr. eq
integer m0, m1, dm
complex R0,VF, R11, R22
integer, parameter :: in_unit=44, out_unit=50
real, dimension (1:91, 1:5) :: Ar2
integer :: ln, col


open (unit=45, file="effective_velocity.txt", status="old",form="
    formatted", action="read")

 open (unit=46, file="input.txt",status="old",form="formatted", action="
    read")
 read (46,fmt=*)
 read (unit=46, FMT=*) Vp, Vs,rho, rof,nu_f, G, h,Qm,  m0, m1, dm
 close(46)

 open (unit=47, file="Input_med_above.txt",status="old",form="formatted"
```

```
    , action="read")
read (47,fmt=*)
read (unit=47, FMT=*) Vp2, Vs2,rho2
 close(47)

print*, "Enter width of the layer" ! width of a layer from keypad
read (*,*) width

print*, "Enter angle of incidence" ! width of a layer from keypad
read (*,*) theta

open (unit=48, file="input_med_below.txt",status="old",form="formatted"
    , action="read")
read (48,fmt=*)
read (unit=48, FMT=*) Vp22, Vs22,rho22
 close(48)
open (unit=50, file="results_RC.txt") !

do ln=1, 91
read (45,*)(Ar2 (ln, col), col=1,5)

  fr=Ar2(ln,1)
 VF=Ar2(ln,2)+CMPLX(0.0,1.0)*Ar2(ln,3)  !Vp if homogeneous

! Zoeppritz upper reflection
   T=sin(theta)/Vp2
   Q=2.*(rho*(VF/2.)**2.-rho2*Vs2**(2.))
   X=rho-Q*T**2.
   Y=rho2+Q*T**2.
   Z=rho-rho2-Q*T**2.
   Wl=sqrt(1-Vp2**2.*T**2.)
```

```
W2=sqrt(1-Vs2**2.*T**2.)
W3=sqrt(1-VF**2.*T**2.)
W4=sqrt(1-(VF/2.)**2.*T**2.)
d1=Vp2*Vs2*VF*(VF/2.)*T**2.*Z**2.
d2=VF*(VF/2.)*W1*W2*X**2.
d3=Vp2*Vs2*W3*W4*Y**2.
d4=rho*rho2*( Vs2*VF*W1*W4 + Vp2*(VF/2.)*W2*W3 )
d5=Q**2.*T**2.*W1*W2*W3*W4
D=d1+d2+d3+d4+d5
R11 = -1+2.*W1*(D**(-1.))*(VF*(VF/2.)*W2*X**2.+ Vs2*VF*rho2*rho*W4 +Q
**2*T**2*W2*W3*W4)

  theta2=ASIN(real( sin(theta)*(VF/Vp2)))

! Zoeppritz lower reflection
T2=sin(theta2)/Vp2
Q2=2.*(rho2*Vs22**(2.)-rho*(VF/2.)**2.)
X2=rho22-Q2*T2**2.
Y2=rho+Q2*T2**2.
Z2=rho22-rho-Q2*T2**2.
W12=sqrt(1-VF**2.*T**2.)
W22=sqrt(1-(VF/2.)**2.*T**2.)
W32=sqrt(1-Vp22**2.*T**2.)
W42=sqrt(1-Vs22**2.*T**2.)
d12=Vp22*Vs22*VF*(VF/2.0)*T2**2.*Z2**2.
d22=Vp22*Vs22*W12*W22*X2**2.
d32= VF*(VF/2.) *W32*W42*Y2**2.
d42=rho*rho2*(Vp22*(VF/2.) *W12*W42 +  Vs22*(VF)*W22*W32 )
d52=Q2**2.*T2**2.*W12*W22*W32*W42
D02=d12+d22+d32+d42+d52
R22 = -1+2.*W12*(D02**(-1.))*(Vs22*(Vp22) *W22*X2**2.+  Vp22*(VF/2.)
```

```fortran
     *rho*rho22*W42 +Q2**2*T2**2*W22*W32*W42)

    dt=2*width/real(VF)

    R0=(R11+R22*exp(-CMPLX(0.0,1.0)*2.*Pi*fr*dt*cos(theta2)))/(1+R11*R22*
     exp(-CMPLX(0.0,1.0)*2.*Pi*fr*dt*cos(theta2)))
    R=abs(R0) ! Amplitude
    phiR = atan(aimag(R0)/real(R0)) ! phase

    write(50, FMT=*) fr,  R, phiR
   print *, fr, R, phiR

 end do
 close(45)
 close(50)

end reflection
```

References

Baecher, G., N. Lanney, and H. Einstein, 1977. Statistical description of rock properties and sampling. *The 18th US Symposium on Rock Mechanics (USRMS)*.

Baecher, G. B., and N. A. Lanney, 1978. Trace length biases in joint surveys. *The 19th US Symposium on Rock Mechanics (USRMS)*.

Bakulin, A., V. Grechka, and I. Tsvankin, 2000a. Estimation of fracture parameters from reflection seismic data-part i: Hti model due to a single fracture set. *Geophysics*, 65(6): 1788–1802.

Bakulin, A., V. Grechka, and I. Tsvankin, 2000b. Estimation of fracture parameters from reflection seismic datapart i: Hti model due to a single fracture set. *Geophysics*, 65(6): 1788–1802.

Bayuk, I., and E. Chesnokov, 1998. Correlation between elastic and transport properties of porous cracked anisotropic media. *Physics and Chemistry of the Earth*, 23(3):361–366.

Bonnet, E., O. Bour, N. E. Odling, P. Davy, I. Main, P. Cowie, and B. Berkowitz, 2001. Scaling of fracture systems in geological media. *Reviews of Geophysics*, 39(3):347–383.

Bour, O., and P. Davy, 1997. Connectivity of random fault networks following a power law fault length distribution. *Water Resources Research*, 33(7):1567–1583.

Brekhovskikh, L. M., 1960. *Waves in layered media*. Academic, New York.

Carcione, J. M., B. Gurevich, J. E. Santos, and S. Picotti, 2013. Angular and frequency-dependent wave velocity and attenuation in fractured porous media. *Pure and Applied Geophysics*, 170(11):1673–1683.

Castagna, J. P., and M. M. Backus, 1993. *Offset-dependent reflectivity - Theory and practice of AVO analysis*. Society of Exploration Geophysicists.

Červenỳ, V., and R. Ravindra, 1971. *Theory of seismic head waves*. University of Toronto Press.

Chapman, M., 2003. Frequency-dependent anisotropy due to meso-scale fractures in the presence of equant porosity. *Geophysical Prospecting*, 51(5):369–379.

Chesnokov, E. M., S. Crampin, and R. G. Hipkin, 1984. Seismic anisotropythe state of the art: Ii. *Geophysical Journal International*, 76(1):1–16.

Chesnokov, E. M., Y. A. Kukharenko, and P. Y. Kukharenko, 1995. Diagram technique method for calculation of effective physical parameters of microinhomogeneous media. *SPIE's 1995 International Symposium on Optical Science, Engineering, and Instrumentation*, pages 2–12.

Chouet, B., 1986. Dynamics of a fluid-driven crack in three dimensions by the finite difference method. *Journal of Geophysical Research: Solid Earth*, 91(B14):13967–13992.

Daley, T. M., M. Feighner, and E. Majer, 2000. Monitoring underground gas storage in a fractured reservoir using time lapse vsp. Technical report, Ernest Orlando Lawrence Berkeley National Lab., CA (US).

Davy, P., A. Sornette, and D. Sornette, 1990. Some consequences of a proposed fractal nature of continental faulting. *Nature*, 348(6296):56–58.

Dawson, T. A., and G. L. Carpenter, 1963. Underground storage of natural gas in indiana. Technical report, Indiana Geological Survey.

De Dreuzy, J.-R., P. Davy, and O. Bour, 2001. Hydraulic properties of two-dimensional random fracture networks following a power law length distribution 1. effective connectivity. *Water Resources Research*, 37(8):2065–2078.

Dershowitz, W., and H. Einstein, 1988. Characterizing rock joint geometry with joint system models. *Rock Mechanics and Rock Engineering*, 21(1):21–51.

Ferrazzini, V., and K. Aki, 1987. Slow waves trapped in a fluid-filled infinite crack: Implication for volcanic tremor. *Journal of Geophysical Research: Solid Earth*, 92(B9): 9215–9223.

Fisher, R., 1953. Dispersion on a sphere. *Proceedings of the Royal Society of London A: Mathematical, Physical and Engineering Sciences*, 217(1130):295–305.

Frehner, M., and S. Schmalholz, 2010. Finite-element simulations of stoneley guided-wave reflection and scattering at the tips of fluid-filled fractures. *Geophysics*, 75(2):T23–T36.

Frehner, M., 2013. Krauklis wave initiation in fluid-filled fractures by seismic body waves. *Geophysics*, 79(1):T27–T35.

Gassmann, F., 1951. Über die elastizität poröser medien: Vierteljahrss-chrift der naturforschenden gesellschaft in zurich 96, 1-23. *Paper translation at http://sepwww. stanford. edu/sep/berryman/PS/gassmann. pdf.*

Goloshubin, G., C. Van Schuyver, V. Korneev, D. Silin, and V. Vingalov, 2006. Reservoir imaging using low frequencies of seismic reflections. *The Leading Edge*, 25(5):527–531.

Goloshubin, G., Y. Tsimbalyuk, I. Privalova, and P. Rusakov, 2014. Low-frequency amplitude analysis for oil detection within the middle jurassic sediments in the southern part of western siberia. *Interpretation*, 2(4):SP35–SP43.

Goloshubin, G. M., T. M. Daley, and V. A. Korneev, 2001. Seismic lowfrequency effects in gas reservoir monitoring vsp data. *SEG Technical Program Expanded Abstracts 2001*, pages 1693–1696.

Goloshubin, G., P. V. Krauklis, L. A. Molotkov, and H. B. Helle, 1994. Slow wave phenomenon at seismic frequencies: 63rd annual international meeting. *SEG, Expanded Abstracts*, pages 809–811.

Greenwood, J., and J. Williamson, 1966. Contact of nominally flat surfaces. *Proceedings of the Royal Society of London A: Mathematical, Physical and Engineering Sciences*, 295:300–319.

Groenenboom, J., and J. Falk, 2000. Scattering by hydraulic fractures: Finitedifference modeling and laboratory data. *Geophysics*, 65(2):612–622.

Gu, B., K. T. Nihei, L. R. Myer, and L. J. Pyrak-Nolte, 1996. Fracture interface waves. *Journal of Geophysical Research: Solid Earth*, 101(B1):827–835.

Hargitaia, H., P. Erikssonb, E. Simpsonc, and O. Okaforb, 2014. Synaeresis crack polygons. *Encyclopedia of Planetary Landforms*, pages 1–4.

Hilterman, F. J., 2001. *Seismic amplitude interpretation*. Society of Exploration Geophysicists and European Association of Geoscientists and Engineers.

Huang, L., R. R. Stewart, N. Dyaur, and J. Baez-Franceschi, 2016. 3d-printed rock models: Elastic properties and the effects of penny-shaped inclusions with fluid substitution. *Geophysics*, 81(6):D669–D677.

Hudson, J., 1981. Wave speeds and attenuation of elastic waves in material containing cracks. *Geophysical Journal of the Royal Astronomical Society*, 64(1):133–150.

Hudson, J., 2000. The effect of fluid pressure on wave speeds in a cracked solid. *Geophysical Journal International*, 143(2):302–310.

Ionov, A. M., 2007. Stoneley wave generation by an incident p-wave propagating in the surrounding formation across a horizontal fluid-filled fracture. *Geophysical Prospecting*, 55(1):71–82.

Korneev, V., 2008. Slow waves in fractures filled with viscous fluid. *Geophysics*, 73(1): N1–N7.

Korneev, V., 2010. Low-frequency fluid waves in fractures and pipes. *Geophysics*, 75(6): N97–N107.

Korneev, V., and G. Goloshubin, 2015. Elastic properties of fluid-saturated fractured rock. *SEG Technical Program Expanded Abstracts*, pages 3202–3208.

Korneev, V., G. Goloshubin, T. Daley, and D. Silin, 2004. Seismic lowfrequency effects in monitoring fluidsaturated reservoirs. *Geophysics*, 69(2):522–532.

Korneev, V., G. Goloshubin, B. Kashtan, A. Bakulin, V. Troyan, G. Maximov, L. Molotkov, M. Frehner, S. Shapiro, and R. Shigapov, 2012. Krauklis wave-half a century after. *EAGE, Saint Petersburg 2012*.

Korneev, V., L. Danilovskaya, S. Nakagawa, and G. Moridis, 2014. Krauklis wave in a trilayer. *Geophysics*, 79(4):L33–L39.

Kozlov, E. A., 2004. Pressure-dependent seismic response of fractured rock. *Geophysics*, 69(4):885–897.

Krauklis, P. V., 1962. About some low-frequency oscillations of a liquid layer in elastic medium. *PMM*, 26(6):1111–1115. in Russian.

Krauklis, P. V., G. Goloshubin, and L. Krauklis, 1994. Slow wave in the porous layer. *Zapiski Nauchnykh Seminarov POMI*, 210:146–153.

Krauklis, P., G. Goloshubin, and L. Krauklis, 1997. A slow wave in a porous layer. *Journal of Mathematical Sciences*, 83(2):259–263.

Krylova, A., and G. Goloshubin, 2016a. Low-frequency seismic reflection from a fractured layer. *78th EAGE Conference and Exhibition 2016*.

Krylova, A., and G. Goloshubin, 2016b. Reflectivity of isotropic-fractured layer. *SEG Technical Program Expanded Abstracts 2016*, pages 3379–3384.

Krylova, A., and G. Goloshubin, 2017. A seismic reflection from isotropic-fractured fluid-saturated layer. *Geophysical Prospecting Online*.

Kuster, G. T., and M. N. Toksoz, 1974. Velocity and attenuation of seismic waves in two-phase media: Part ii. experimental results. *Geophysics*, 39(5):607–618.

Liner, C. L., 2012. *Elements of seismic dispersion: A somewhat practical guide to frequency-dependent phenomena*. Society of Exploration Geophysicists.

Liner, C. L., 2016. *Elements of 3D seismology*. Society of Exploration Geophysicists.

Liu, E., S. Crampin, J. Queen, and W. Rizer, 1993. Velocity and attenuation anisotropy caused by microcracks and macrofractures in a multiazimuth reverse vsp. *Canadian Journal of Exploration Geophysics*, 29(1):177–188.

Liu, E., J. H. Queen, X. Y. Li, M. Chapman, H. B. Lynn, and E. M. Chesnokov, 2002. Analysis of frequency-dependent seismic anisotropy from a multicomponent vsp. pages 101–104.

Long, J., J. Remer, C. Wilson, and P. Witherspoon, 1982. Porous media equivalents for networks of discontinuous fractures. *Water Resources Research*, 18(3):645–658.

Maksimov, G. A., A. V. Derov, B. M. Kashtan, and M. Y. Lazarkov, 2011. Estimation of hydro-fracture parameters by analysis of tube waves at vertical seismic profiling. *Acoustical Physics*, 57(4):529–541.

Molotkov, L., 1979. Equivalence of periodic-layered and transversally isotropic media. *Mathematical Problems of the Theory of Wave Propagation. 10*, 1:219–233.

Molotkov, L., 1984. *Matrix method in the theory of wave propagation in layered elastic and liquid media*. Nauka, Leningrad.

Nagy, P., G. Blaho, and L. Adler, 1993. Excess nonlinearity in materials containing microcracks. *Review of Progress in Quantitative Nondestructive Evaluation. 13 B*.

Nakagawa, S., and V. Korneev, 2014. Effect of fracture compliance on wave propagation within a fluid-filled fracture. *The Journal of the Acoustical Society of America*, 135(6): 3186–3197.

Nakagawa, S., S. Nakashima, and V. A. Korneev, 2016. Laboratory measurements of guided-wave propagation within a fluid saturated fracture. *Geophysical Prospecting*, 64:143–156.

Nakagawa, S., and M. A. Schoenberg, 2007. Poroelastic modeling of seismic boundary conditions across a fracture. *The Journal of the Acoustical Society of America*, 122(2): 831–847.

Park, Y.-J., J.-R. Dreuzy, K.-K. Lee, and B. Berkowitz, 2001. Transport and intersection mixing in random fracture networks with power law length distributions. *Water Resources Research*, 37(10):2493–2501.

Pecorari, C., 1997. Acoustoelasticity in cracked solids. *Geophysical Journal International*, 129(1):169–175.

Pride, S. R., E. Tromeur, and J. G. Berryman, 2002. Biot slowwave effects in stratified rock. *Geophysics*, 67(1):271–281.

Priest, S. D., 2012. *Discontinuity analysis for rock engineering*. Springer Science & Business Media.

Pyrak-Nolte, L. J., and N. G. W. Cook, 1987. Elastic interface waves along a fracture. *Geophysical Research Letters*, 14(11):1107–1110.

Rempe, M., T. Mitchell, J. Renner, S. Nippress, Y. Ben-Zion, and T. Rockwell, 2013. Damage and seismic velocity structure of pulverized rocks near the san andreas fault. *Journal of Geophysical Research: Solid Earth*, 118(6):2813–2831.

Ren, H., G. Goloshubin, and F. J. Hilterman, 2009. Poroelastic analysis of amplitude-versus-frequency variations. *Geophysics*, 74(6):N41–N48.

Scales, J. A., and R. Snieder, 1999. What is a wave? *Nature*, 401(6755):739–740.

Schoenberg, M., 1983. Reflection of elastic waves from periodically stratified media with interfacial slip. *Geophysical Prospecting*, 31(2):265–292.

Schoenberg, M., and J. Douma, 1988. Elastic wave propagation in media with parallel fractures and aligned cracks. *Geophysical Prospecting*, 36(6):571–590.

Schoenberg, M., and C. Sayers, 1995. Seismic anisotropy of fractured rock. *Geophysics*, 60(1):204–211.

Schoenberg, M., 1980. Elastic wave behavior across linear slip interfaces. *The Journal of the Acoustical Society of America*, 68(5):1516–1521.

Shapiro, S., 2017. Stress impact on elastic anisotropy of triclinic porous and fractured rocks. *Journal of Geophysical Research: Solid Earth*, 122(3):2034–2053.

Shih, P.-J. R., and M. Frehner, 2016. Laboratory evidence for krauklis-wave resonance in fractures and implications for seismic coda wave analysis. *Geophysics*, 81(6):T285–T293.

Smith, T. M., C. H. Sondergeld, and C. S. Rai, 2003. Gassmann fluid substitutions: A tutorial. *Geophysics*, 68(2):430–440.

Spetzler, J., and R. Snieder, 2004. The fresnel volume and transmitted waves. *Geophysics*, 69(3):653–663.

Tang, X. M., and C. H. Cheng, 1988. Wave propagation in a fluid-filled fracture an experimental study. *Geophysical Research Letters*, 15(13):1463–1466.

Trapeznikova, N., 1985. *Prognosis and interpretation of seismic wave dynamics [in Russian]*. Nauka.

Tsvankin, I., J. Gaiser, V. Grechka, M. Van Der Baan, and L. Thomsen, 2010. Seismic anisotropy in exploration and reservoir characterization: An overview. *Geophysics*, 75 (5):75A15–75A29.

Ulmishek, G. F., 2003. *Petroleum geology and resources of the West Siberian Basin, Russia*. US Department of the Interior, US Geological Survey.

Walsh, J., and M. Grosenbaugh, 1979. A new model for analyzing the effect of fractures on compressibility. *Journal of Geophysical Research: Solid Earth*, 84(B7):3532–3536.

Zoeppritz, K., 1919. Erdbebenwellen vii. *Nachrichten von der Gesellschaft der Wissenschaften zu Göttingen, Mathematisch-Physikalische Klasse*, 1919:57–65.